VISIBLE- LIGHT DRIVEN PHOTOCATALYTIC DEGRADATION OF ORGANIC POLLUTANTS OVER $CuWO_4$@TiO_2 NANOCOMPOSITE: A COMBINED EXPERIMENTAL AND THEORITICAL STUDIES

By

Keya Rani Dutta

ID-MSCHEM014F

A thesis submitted in partial fulfillment of the requirements for the degree of MASTER of SCIENCE in Chemistry

Department of Chemistry

CHITTAGONG UNIVERSITY OF ENGINEERING AND TECHNOLOGY

April 2025

Declaration

I hereby declare that the work contained in this Thesis has not been previously submitted to meet the requirements for an award at this or any other higher education institution. To the best of my knowledge and belief, the Thesis contains no material previously published or written by another person except where due reference is cited. Furthermore, the Thesis complies with the PLAGIARISM and ACADEMIC INTEGRITY regulations of CUET.

Keya Rani Dutta

Student ID - 21MSCHEM014F

Department of Chemistry

Chittagong University of Engineering & Technology (CUET)

Dedication

To my beloved parents, siblings, teachers, and supportive life partner, and countless others who've contributed to my journey, whether through a kind word, a helping hand, or a moment of inspiration.

List of Publications

Journal Articles

1. "Optimizing Photocatalytic Dye Degradation: A Machine Learning and Metaheuristic Approach for Predicting Methylene Blue in Contaminated Water" Yunus Ahmed, Keya Rani Dutta, Sharmin Nahar Chowdhury Nepu, Meherunnesa Prima, Hamad AlMohamadi, Parul Akhtar, Results in Engineering, 2025, 25; 103538 DOI: https://doi.org/10.1016/j.rineng.2024. 103538. (IF: 6.0, Q1).

2. "Emerging strategies in sustainable removal of antibiotics using semiconductor-based photocatalysts" Yunus Ahmed1, Keya Rani Dutta, Parul Akhtar, Md. Arif Hossen, Md Jahangir Alam, Obaid A. Alharbi, AlMohammadi and Abdul Wahab Mohammad, Beilstein Journal of Nanotechnology, 2025, 16, 264–285. https://doi.org/10.3762/bjnano.16.21 (IF 3.2, Q2).

3. "Advanced Ciprofloxacin Quantification: A Machine Learning and Metaheuristic Approach Using Ultrasensitive Chitosan-Gold Nanoparticle Based Electrochemical Sensor" Yunus Ahmed, Tahmina Akter, Meherunnesa Prima, Keya Rani Dutta, Sanjida Mukut, Mohebul Ahsan, Md Mahbubur Rahman, M.K. Mohammad Ziaul Hyder, Journal of Environmental Chemical Engineering. 2025, 13(1) 115094; DOI: https://doi.org/10.1016/j.jece.2024. 115094. (IF: 7.4, Q1)

Conferences

1. "Photocatalytic Activity of $CuWO_4$@TiO_2 Nanocomposites: Synthesis, Optimization, and Application in Wastewater Treatment." Keya Rani Dutta, Md. Mahfujur Rahman, Akser Alam Siddiqua Maya and Yunus Ahmed. 2nd ICRAC-2024, Jagannath University, 31 January – 02 February 2025

2. "Enhancing Photocatalytic Dye Degradation: A Machine Learning and Metaheuristic- Based Protocol for Methylene Blue." Meherunnesa Prema, Sharmin Nahar Chowdhury, Keya Rani Dutta, Yunus Ahmed. 2nd ICRAC-2024, Jagannath University, 31 January – 02 February 2025.

3. "Synthesis, characterization, and optimization of $FeWO_4$@TiO_2, an efficient nanocatalyst for the degradation of antibiotic and textile dye in neutral solution." Akser Alam Siddiqua Maya, Keya Rani Dutta, Md. Mahfujur Rahman, Tahmina Akter and Yunus Ahmed. 7th ICNST, Asian University for Women, 02-03 March 2023.

4. "Synthesis, Characterization, Optimization, and Application of $CuWO_4$@TiO_2 Nanoadsorbent for the Removal of Antibiotic from Aqueous Solution." Yunus Ahmed, Md. Mahfujur Rahman, Akser Alam Siddiqua Maya, Tahmina Akter, Keya Rani Dutta, Obaide Alharbi. 19th IWA-LET, Essen, Germany, 24-28 June 2024.

Approval/Declaration by the Supervisor

This is to certify that Keya Rani Dutta has carried out this research work under my supervision, and that she has fulfilled the relevant Academic Ordinance of the Chittagong University of Engineering and Technology, so that she is qualified to submit the following Thesis in the application for the degree of MASTER of SCIENCE in Chemistry. Furthermore, the Thesis complies with the PLAGIARISM and ACADEMIC INTEGRITY regulations of CUET.

Dr. Yunus Ahmed (Supervisor)

Professor

Department of Chemistry

Chittagong University of Engineering & Technology

Acknowledgement

All praise and gratitude to the Merciful and Almighty God, whose blessings have granted me the capability and opportunity to successfully complete this research and submit the required thesis for fulfillment of Master of Science (M.Sc.) degree in Chemistry.

I am deeply honored to express my heartfelt appreciation and sincere gratitude to my esteemed teacher and supervisor, Dr. Yunus Ahmed, Professor, Department of Chemistry, CUET, Chattogram. His invaluable academic guidance, unwavering support, continuous encouragement, and insightful discussions have been instrumental throughout the research and thesis preparation process. This achievement would not have been possible without his dedication to research, constructive feedback, and constant motivation.

I extend my sincere thanks to all the faculty members and staff of our department for their encouragement, collaboration, and continuous inspiration, which have significantly enriched my academic journey. I am also immensely grateful to my friends of our Water and Environmental Biotechnology lab for their unwavering assistance and camaraderie.

My deepest gratitude goes to my beloved parents, Reva Dutta and Millon Dutta, whose unconditional love, sacrifices, and encouragement have been the foundation of my academic pursuits. I extend my heartfelt thanks to my mentor, Subrata Dev, for his continuous guidance and motivation from my childhood to this day. I am equally thankful to my siblings, Uttam Dutta, Mukta Dutta, and Supta Gosh, as well as my beloved husband, Prince Das, for their unwavering support, patience, and encouragement throughout this journey.

The author also grateful to P&D, CUET for providing scholarship for the study.

Abstract

With the growing presence of organic pollutants like methylene blue (MB) in wastewater, there are significant concerns for both the environment and public health, highlighting the urgent need for the development of effective remediation strategies. This study addressed the urgent need for effective remediation strategies for organic pollutants, specifically methylene blue (MB), in wastewater by synthesizing and evaluating a $CuWO_4$@TiO_2 nanocomposite photocatalyst. A comprehensive characterization using UV-Vis diffuse reflectance spectroscopy (DRS), field emission scanning electron microscopy (FESEM), X-ray diffraction (XRD), X-ray photoelectron spectroscopy (XPS), Brunauer-Emmett-Teller (BET) surface area analysis, electrochemical impedance spectroscopy (EIS), and cyclic voltammetry (CV) was conducted to assess the nanocomposite's structural, morphological, and electrochemical properties. Density functional theory (DFT) calculations provided insights into the photocatalytic mechanism, particularly the most stable Ti/Cu@$CuWO_4$ interface configuration. To enhance predictive modeling for MB degradation, ten machine learning (ML) algorithms, including AdaBoost, Bagging, CatBoost, Decision Tree, Extra Trees, Gradient Boosting, HistGradientBoosting, LightGBM, Random Forest, and XGBoost, were evaluated based on coefficient of determination (R^2), mean square error (MSE), root mean square error (RMSE), mean absolute error (MAE), and median absolute error (MedAE). Among this HistGradientBoosting model demonstrating exceptional performance, achieving an R^2 of 0.9998 in training and 0.9915 in testing, along with low error metrics. Experimental validation under optimal conditions (200 mg/L catalyst, 150 mW/cm² light intensity, 88.6 min reaction time) confirmed a 98.5% MB degradation efficiency, closely aligning with the ML-predicted 98.99%. The nanocomposite exhibited significantly higher catalytic activity as compared to individual $CuWO_4$ and TiO_2, with rate constants of 0.0302 min^{-1} for the nanocomposite, 0.0197 min^{-1} for $CuWO_4$, and 0.0167 min^{-1} for TiO_2. Scavenger experiments revealed the order of active species in the degradation process as $O_2^{\bullet -} > HO^{\bullet} > {}^1O_2 > e^- > h^+$, this research emphasizing the combined effectiveness of experimental, computational, and machine learning methods in optimizing photocatalytic water treatment processes.

বিমূর্ত

বর্জ্য জলে মিথিলিন ব্লু (এমবি) এর মতো জৈব দূষণকারীর ক্রমবর্ধমান উপস্থিতির সাথে, পরিবেশ এবং জনস্বাস্থ্য উভয়ের জন্যই উল্লেখযোগ্য উদ্বেগ বাড়ছে যা কার্যকর প্রতিকার কৌশলগুলির বিকাশের জরুরি প্রয়োজনকে তুলে ধরে। এই অধ্যয়নটি একটি $CuWO_4@TiO_2$ ন্যানোকম্পোজিট ফটোক্যাটালিস্ট সংশ্লেষণ এবং মূল্যায়নের মাধ্যমে বর্জ্য জলে জৈব দূষণকারী, বিশেষত মিথিলিন ব্লু (এমবি) এর জন্য কার্যকর প্রতিকার কৌশলগুলির জরুরী প্রয়োজনকে সম্বোধন করেছে। UV-Vis ডিফিউজ রিফ্ল্যাক্টেন্স স্পেকট্রোস্কোপি (DRS), ফিল্ড এমিশন স্ক্যানিং ইলেক্ট্রন মাইক্রোস্কোপি (FESEM), এক্স-রে ডিফ্র্যাকশন (XRD), এক্স-রে ফটোইলেক্ট্রন স্পেকট্রোস্কোপি (XPS), ব্রুনাউয়ার-এমমেট-টেলার (BET) সারফেস এরিয়া অ্যানালাইসিস, ইলেক্ট্রোকেমিক্যাল ইম্পিডেন্স স্পেকট্রোস্কোপি (EIS), ব্যবহার করে একটি ব্যাপক চরিত্রায়ন এবং সাইক্লিক ভোল্টমেট্রি (CV) ন্যানোকম্পোজিটের কাঠামোগত, রূপগত এবং ইলেক্ট্রোকেমিক্যাল বৈশিষ্ট্যগুলি মূল্যায়ন করার জন্য পরিচালিত হয়েছিল। ঘনত্ব কার্যকরী তত্ত্ব (DFT) গণনা ফটোক্যাটালিটিক প্রক্রিয়ার অন্তর্দৃষ্টি প্রদান করে, বিশেষ করে সবচেয়ে স্থিতিশীল $Ti/Cu@CuWO_4$ ইন্টারফেস কনফিগারেশন। মিথিলিন ব্লু অবক্ষয়ের ভবিষ্যদ্বাণীমূলক মডেলিং পর্যালোচনার জন্য, অ্যাডাবুস্ট (AdaBoost), ব্যাগিং (Bagging), ক্যাটবুস্ট (CatBoost), ডিসিশন ট্রি (Decision Tree), এক্সট্রা ট্রিস (Extra Trees), গ্রেডিয়েন্ট বুস্টিং (Gradient Boosting), হিস্টগ্র্যাডিয়েন্টবুস্টিং (HistGradientBoosting), লাইটজিবিএম (LightGBM), রেন্ডম ফরেস্ট (Random Forest) এবং এক্সজিবুস্ট (XGBoost) নামক দশটি মেশিন লার্নিং (ML) অ্যালগরিদম ব্যাবহার করা হয়েছিল এবং তাদের নির্ধারণের সহগ (R^2), গড় বর্গ ত্রুটি (MSE), মূল গড় বর্গক্ষেত্র ত্রুটি (RMSE), গড় পরম ত্রুটি (MAE) এবং মধ্যম পরম ত্রুটি (MedAE)-এর উপর ভিত্তি করে মূল্যায়ন করা হয়েছিল। হিস্টগ্রেডিয়েন্ট বুস্টিং মডেলটি কার্যকরী কর্মক্ষমতা প্রদর্শন করে, যা প্রশিক্ষণে R^2 ০.৯৯৯৮ এবং পরীক্ষায় R^2 ০.৯৯১৫ অর্জন করে, সাথে কম ত্রুটির মেট্রিক্সসমূহ দৃশ্য হয়। সর্বোত্তম অবস্থার অধীনে পরীক্ষামূলক বৈধতা (২০০ mg/L অনুঘটক, ১৫০ mW/cm^2 আলোর তীব্রতা, ৮৮.৬ মিনিট প্রতিক্রিয়া সময়) একটি ৯৮.৫ % MB অবক্ষয় দক্ষতা নিশ্চিত করেছে যা ML-পূর্বাভাসিত ৯৮.৯৯ % এর সাথে ঘনিষ্ঠভাবে সারিবদ্ধ। $CuWO_4@TiO_2$ ন্যানোকম্পোজিট পৃথক $CuWO_4$ এবং TiO_2-এর তুলনায় উল্লেখযোগ্যভাবে উচ্চতর অনুঘটক কার্যকলাপ প্রদর্শন করেছে, যা যথাক্রমে ০.০৩০২ min^{-1}, ০.০১৯৭ min^{-1} এবং TiO_2-এর জন্য ০.০১৬৭ min^{-1} হারের ধ্রুবক। স্ক্যাভেঞ্জার পরীক্ষাগুলি অবক্ষয় প্রক্রিয়ায় সক্রিয় প্রজাতির ক্রমকে $O_2\bullet^- > HO\bullet > {}^1O_2 > e^- > h^+$ হিসাবে প্রকাশ করেছে। ফটোক্যাটালিটিক জল–চিকিৎসা প্রক্রিয়াটি অপ্টিমাইজ করার ক্ষেত্রে পরীক্ষামূলক, গণনামূলক এবং মেশিন লার্নিং পদ্ধতির সম্মিলিত কার্যকারিতার উপর জোর দেয়।

Table of Contents

List of Figures

List of Tables

Nomenclature

Symbols	Elaborations
e.g.	for example
etc.	Etcetera
et al	And Others
Fig.	Figure
Min	Minimum
Max	Maximum
ppm	Parts per million
nm	nanometer
λ	Wavelength
eV	Electron volt
ppb	Parts per billion
^{0}C	Degree Celsius
ppt	Parts Per Thousand

Acronyms and Abbreviations

AB	AdaBoost
BET	Brunauer Emmett Teller
CB	CatBoost
CV	Cyclic Voltammetry
DFT	Density Functional Theory
DT	Decision Tree
EIS	Electrochemical Impedance Spectroscopy
FE-SEM	Field Emission Scanning Electron Microscopy
GGA	Generalized Gradient Approximation
GB	Gradient Boosting
GCE	Glassy Carbon Electrode
HGB	Hist Gradient Boosting
LGB	Light GBM
ML	Machine Learning
MB	Methylene Blue
MSE	Mean Square Error
MAE	Mean Absolute Error
MedAE	Median Absolute Error
RF	Random Forest
SHAP	Shapley Additive Explanations
UV-VIS	Ultraviolet-visible Spectroscopy
XGB	Extreme Gradient Boosting
XRD	X-ray Diffraction
XPS	X-ray Photoelectron Spectroscopy

Chapter 1: INTRODUCTION

1.1 Background

Freshwater is essential to the survival of all species on Earth since different ecosystems and cultures depend on surface water supplies [1]. However, the widespread use of organic dyes in industrial processes has led to significant water pollution, which could have terrible consequences for human health and the ecological balance [2, 3]. Rivers, ponds, lakes, and other bodies of water are the main regions at risk. Millions of tones of effluent are released daily into the environment by the paper, textile, pharmaceutical, and other sectors. As a result, treating these dyes prior to discharge is crucial [4, 5]. Methylene blue (MB), for example, has an acute risk of burning the eyes in animals as well as humans [6]. When swallowed, MB stimulates the digestive system, causing a variety of symptoms such as headaches, tachycardia, indigestion, nausea, and vomiting. To keep the environment in balance, MB dye and other toxins must be eliminated from polluted water because they are toxic to living things [7]. Numerous methods, including ion exchange, adsorption, filtration, and catalytic oxidation, have been used to eliminate the contaminants listed above. But the results aren't satisfactory [8].

The nontoxicity, environmental friendliness, and strong photostability of photocatalytic degradation make it a green way to remove toxins. In environmental remediation, this method has gained more attention since it uses the maximum amount of solar energy to break down organic materials into inorganics like CO_2 and H_2O [9]. Photocatalysts harvest the infinite sunlight to generate chemical energies or eliminate environmental pollution via different photocatalytic processes such as H_2 evolution, pollutant removal, CO_2 reduction, and Nitrogen fixation [10]. However, inaccuracy and unpredictability continue

to be limitations of photocatalysis; designing fruitful and sustainable semiconductor photocatalysts is critical. Semiconductor nanomaterials have been effectively utilized as chemosensors to identify and analyze minute amounts of harmful environmental chemicals. This makes them invaluable for monitoring and detecting ecological pollutants and protecting public health [11]. Researchers are quite interested in TiO_2 because it is an n-type semiconductor, which has led to substantial study for a variety of photocatalytic technics [12]. Because of its great chemical and thermal stability, non- toxicity, and affordability, antase titanium (TiO_2) has drawn a lot of attention among the photocatalytic nanomaterials that have recently been established and employed as photocatalysts for breaking down of synthetic dyes water [13]. Yet, anatase TiO_2 has many drawbacks, including a broad energy bandgap (~3.2 eV) that results in inadequate absorption of light that is visible and the quick recombination of pairs of electrons and holes produced by photoenergy [14]. Its wide range of practical applications is further limited by the difficulty of recovering and separating TiO_2 nanoparticles from aqueous solutions [15].

The production of TiO_2 composites enables morphological modification and property refinement for improved performance. Metals like noble, semiconductors, metal-organic frameworks, and C nanotubes all have intrinsic chemical and mechanical qualities that make them highly promising for the straightforward production of effective TiO_2 hybrid nanocomposites [16, 17]. Despite the promising potential for effective photocatalytic mineralisation of poisonous dyes in water, titania performance has proved difficult to enhance, especially in conjunction with other semiconductors [18]. Recent research found that the photocatalytic activity may be significantly increased by mixing with various semiconductors, including SnO_2, NiO, Bi_2O_3, $Sb_xSn_{1-x}O_2$, $FeTiO_3$, In_2O_3, ZnO, CdS, ZrO_2, CuS, Fe_2O_3, WO_3, SiO_2, and others [19-22]. Due to its proper CB

and VB locations in relation to TiO_2, WO_3 also hunts for photogenerated electrons that are obtained from TiO_2. The WO_3 VB is photoexcited to form holes, which then transfer and collect in the valence band (VB) of TiO_2 [23]. By growing the capacity for charge transfer, this method raises the WO_3/TiO_2 composite's photoactivity. In heterogeneous catalysis, nanometer-scale tungstates comprising $ZnWO_4$, Bi_2WO_6, $CuWO_4$, and other elements are thoroughly investigated [24]. $CuWO_4$ is a novel and promising material that has recently shown promise in water splitting and organic pollutant photodegradation. $CuWO_4$ is an n-type semiconductor distinguished by its remarkable chemical reliability and particular redox performance. It is photosensitive in light due to its band gap, which is around 2.2 eV [25, 26]. The valence band (VB) and conduction band (CB) of TiO_2 and $CuWO_4$ are positioned to facilitates electron transport. To create a p-n heterojunction with TiO_2, $CuWO_4$ is the perfect semiconductor. Electrochemical detection is a highly efficient and sensitive method for detecting substances. This detection platform is known for its cost-effectiveness, sustainability, consistent performance, and remarkable sensitivity, making it a valuable tool in various applications [27]. Electrochemical sensors utilizing ternary nanocomposites have garnered considerable interest because they facilitate swift electron transfer at the interface, provide conductive properties that may be adjusted and increase the particle size for improved performance [28].

Density functional theory has been identified as a basic computational method for investigating nanophotocatalytic electronic, structural, and optical properties. The principles of transferring charge and surface reactivity of nanophotocatalysts are beneficial during photocatalytic activity optimization [29, 30]. Capable of simulating the interaction between light and matter at the atomic scale, DFT thus provides the means to rationally design active nanomaterials, with an in-depth

knowledge of heterojunction behavior and underlying mechanism of degradation processes in photocatalytic systems [31]. Machine learning models play a critical role in the correct prediction of contaminant concentrations in polluted water. Development of precise predictive models is crucial for protecting people health and maintaining integrity of the ecosystem in light of dye pollution in aquatic environments. Different ML approaches exist for this purpose, including Linear Regression (LR), Support Vector Machines (SVMs), Gaussian Processes (GPs), Artificial Neural Networks (ANNs), and tree-based methods. Among the tested models, tree-based models proved to be the most effective option. Further improvements involve the development of training techniques based on gradients for faster training of tree-based models with improvement in predictive performance [32]. Continuous research has brought forth algorithms such as AdaBoost (AB), CatBoost (CB), LightGBM, HistGradientBoosting (HGB), and Extreme GB (XGB) [33-35].

1.2 Aims and Objectives

This study focuses on the following specific objectives

- To synthesize and characterize the $CuWO_4$@TiO_2 nanocomposite for efficient dye degradation by photocatalysis.
- To understand the geometrics and electronics properties and optimize the structure performance by Density Functional Theory (DFT).
- To optimize the photocatalysis process by using Machine Learning (ML) algorithoms.
- To explore the degradation mechanisms involved in dye degradation and evaluate the stability and reusability of $CuWO_4$@TiO_2 nanocomposite for practical applications.

1.3 Significance of This Study

This study will help educate future researchers on the degradation and removal of dye from wastewater, contributing to environmental remediation. Comprehensive knowledge on photocatalytic degradation wil be provide by this study, process using $CuWO_4@TiO_2$ nanocomposites and its efficiency under different operational conditions. It will also explore the role of reactive species contribute to dye breakdown and their impact on pollutant breakdown. The final phase of the study will investigate the underlying degradation mechanism, assess the stability and reusability of photocatalysts, and propose a sustainable strategy for large-scale wastewater treatment applications.

1.4 Thesis Outline

Chapter 1 outlines the background and key objectives of the study, emphasizing the role of nano-photocatalysts in wastewater treatment.

Chapter 2 outlines the brief literature review focusing on wastewater treatment technologies, various photocatalytic processes and their mechanisms, and lab-scale to potentially large-scale photocatalysis applications.

Chapter 3 describes the materials and instruments used during the research work and the procedures followed for the range of tests conducted.

Chapter 4 provides a detailed description of the characterization of the $CuWO_4@TiO_2$ nanocomposite, DFT calculations to analyze electronic and structural properties, parameter optimization using ML, and other analyses to validate the catalyst's efficiency and stability.

Chapter 5 summarizes the entire study, providing a comprehensive conclusion and future research directions for enhancing the photocatalytic performance of $CuWO_4@TiO_2$ nanocomposites for sustainable wastewater treatment.

Chapter 2: LITERATURE REVIEW

2.1 Background

Antibiotics are chemical substances used to treat bacterial complications in humans, animals, aquaculture, and livestock feed [36]. Between 2010 and 2019, their usage expanded dramatically to an estimated 100,000 to 200,000 tonnes worldwide [37], with around half used for animal feed, which is expected to climb to 105,796 tonnes by 2040 [38, 39]. The public is concerned about the extensive and frequently excessive use of antibiotics, particularly as they are being found to be environmental pollutants that come from human and animal waste [40]. Antibiotic resistance spreads more quickly when antibiotics are present in the environment repeatedly [41-43]. Antibiotic resistance spreads more quickly when antibiotics are present in the environment repeatedly, since this lead the creation of antibiotic-resistant bacteria (ARBs) and associated ARGs [44, 45]. According to certain sources, there is a serious threat to the ecosystem and human health [46-50]. Alarming projections in the USA anticipated antimicrobial resistance-related deaths exceeding the combined toll of cancer and diabetes, with approximately 23,000 deaths annually [51]. Extended exposure to antibiotics in natural environments promotes the growth of bacteria that are resistant to antibiotics (ARBs) and the genes that cause this resistance (ARGs), which contributes to the spread of antibiotic resistance and poses a significant risk to both human health and ecological systems [52].

To address the environmental hazards posed by antibiotics, we use physical, biological, and chemical methods [48,53, 54]. Various physical wastewater treatment techniques are based on mechanical separation to reduce contaminant levels by relocating rather than degrading antibiotics [42,43, 55]. In wastewater treatment, biological methods, including biological membrane technology and the activated sludge process, are frequently used [56]. These technologies are facing scrutiny because they come with certain limitations, including prolonged processing times and the challenge of effectively recovering generated heat [57]. On the other hand,

chemical processes like separating solids from liquids and degradation are also frequently employed to render pollutants non-toxic or non-hazardous [48, 58]. It should be noted that many of the conventional methods fail in degrading antibiotics completely since most of them are very complex in structure and are even resistant to biodegradation in an aquatic medium [59]. Advanced oxidation process (AOP) has lately arisen as one of the very effective treatment technology that has proven to remove antibiotics more effectively compared to the previous methods of physical adsorption, flocculation as well as chemical oxidation [42, 43, 60]. AOPs offer several advantages, including simple equipment, straightforward operation, minimal sludge production, and the rapid generation of mineralized products. They are also very good at breaking down refractory and high-strength organic compounds [61]. Photocatalyst-based AOPs represent a promising strategy for eliminating antibiotics from polluted water, providing several advantages over other oxidation techniques. By utilizing light energy to activate catalysts, these AOPs facilitate antibiotic degradation without needing extra chemical oxidants and producing minimal of harmful by-products, promoting environmental sustainability [62]. Moreover, they exhibited high selectivity towards antibiotics with preserving water quality. Compared to other photocatalysts material, semiconductor-based photocatalysts often achieved superior efficiency and high mineralization rates, offering a comprehensive solution for antibiotic contamination. The progressively increasing trend of publications and corresponding citations record in recent times highlighted the superiority of semiconductor-based photocatalysts for the degradation of antibiotics (Figure 2.1). The appeal of photocatalysis lies in its potential to achieve extensive mineralization, converting organic pollutants into harmless mineral compounds. Additionally, its nonselective, it can deal with a large range of pollutents, which makes it a flexible choice for environmental remedition in a variety in water and air purification applications. These features collectively position photocatalysis as an attractive approach for addressing pollution challenges in diverse settings.

.

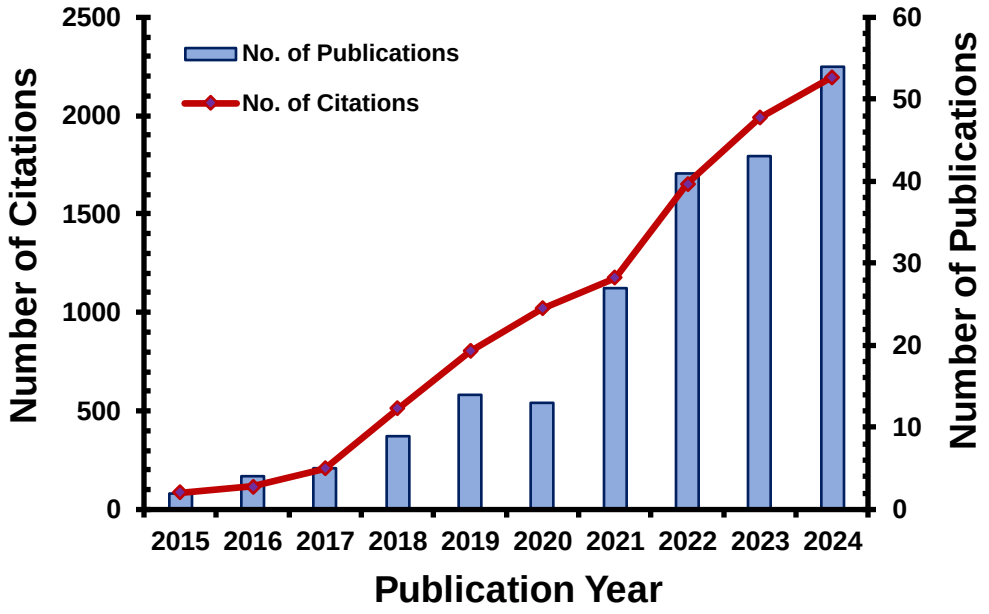

Figure 2.1 The trend of publications focusing on antibiotic degradation using semiconductor-based photocatalysts (Scopus database).

A number of noteworthy review studies that concentrate on eliminating antibiotics through AOPs have surfaced in recent years [63-65]. Some of these articles explored into specific AOP methods tailored for antibiotic remediation, such as H_2O_2-based AOP [64], Fenton-based AOPs [66], UV-based AOPs [67], UV/chlor(am)ine based AOP [68], electrochemical-based AOP (EAOP) [69], persulfate and peroxymonosulfate based AOPs [65] as well as the catalytic degradation process [70], graphene-based materials [71, 72], adsorption process [42, 43]. However, these papers primarily discuss the oxidizing agents or AOP processes and their efficiency in removing antibiotics without focusing on the detailed mechanisms of how these materials or processes degrade antibiotics. They do not address the entry of antibiotics into the environment, their adverse impact on human health and the environment, or the effects of each treatment process in relation to established industrial applications. As a result, there is a lack of understanding about these processes and their practical limitations for large-scale commercial wastewater treatment.

This literature review entirely concentrates on semiconductor-based photocatalytic processes and their effectiveness in eliminating antibiotics while also addressing their

practical constraints. The scope includes discussions on antibiotic sources, pollution risks and impacts, removal challenges, and influential factors. This study help to understanding of the essential principles and mechanisms underlying semiconductor-based photocatalysts and their sequential modification for enhanced antibiotics degradation from contaminated water. The discussion also highlights concluding remarks and future directions of emerging techniques for sustainable wastewater treatment.

2.2 Sources of Antibiotic Pollution

The primary sources of antibiotics in surface water include animal husbandry and aquaculture, domestic sewage discharges, pharmaceutical manufacturing, and healthcare facilities [73]. Antibiotics are commonly administered to animals through feed or water, primarily for growth promotion in large-scale animal farming operations and to prevent and treat infectious diseases [74]. Consequently, antibiotic residues are excreted by the animals in their faces, which can enter the environment by applying manure as fertilizer or runoff from animal housing facilities. Additionally, antibiotics are extensively used in aquaculture, where only a fraction (20-30%) of the pharmaceuticals used are absorbed by aquatic products [75]. Domestic sewage discharge represents a significant source of antibiotics in urban water systems [76]. Antibiotics are commonly prescribed to individuals to treat various infections. Yet, research indicates that only a small fraction of antibiotics administered to the body are absorbed and utilized by organisms. The remaining 40%–90% of active medications or metabolites are excreted in faces and urine [77]. Consequently, treated wastewater or septic effluent containing residual antibiotics can be released into nearby water bodies [78]. Pharmaceutical companies generate, handle, and dispose of significant quantities of antibiotics during production. A study found that downstream water sources from pharmaceutical production plants had significantly higher antibiotic concentrations than upstream sources [79]. Hospitals and healthcare facilities also significantly contribute antibiotics to urban water systems [80]. These

facilities administer large doses of antibiotics to patients, resulting in the excretion of antibiotic residues through wastewater. Medical waste incineration is a significant source of antibiotic emissions, potentially contributing to the spread of antibiotic resistance. The present study investigates several primary sources of environmental antibiotics, as illustrated in Figure 2.2, and provides a comprehensive analysis of their pathways for their movement and persistence in groundwater systems.

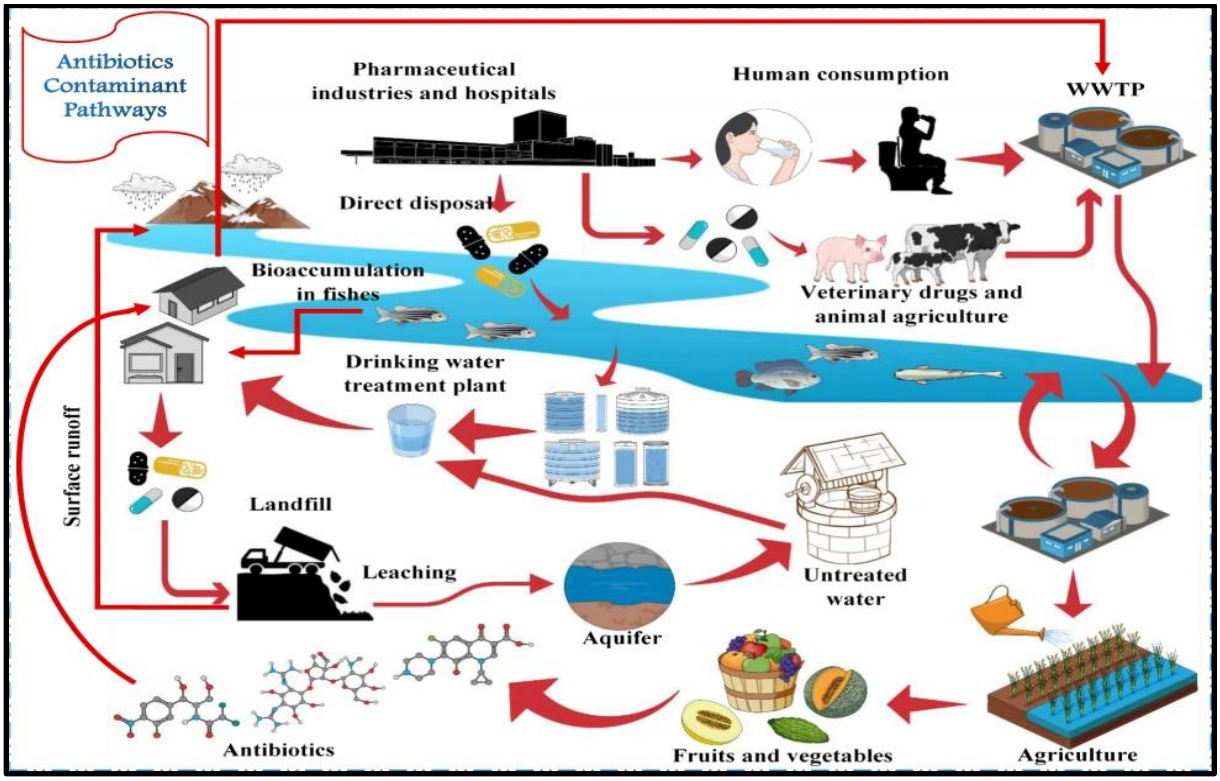

Figure 2.2 Sources of antibiotics in the environment and their pathway

2.3 Challenges of Removing Antibiotics from the Environment

The challenge of removing antibiotics from the environment, including water bodies, soil, and wastewater, is commonly called the antibiotic removal problem. Antibiotics present in the environment pose risks to both ecosystems and human health. Several primary barriers contribute to the difficulty in removing antibiotics effectively:

2.3.1 Chemical Complexity

The diverse chemical structures of antibiotics present a significant challenge for their removal compared to simpler contaminants. Various classes of antibiotics necessitate specific treatment processes to achieve effective removal. Furthermore, the degradation of antibiotics can result in the formation of transformation products [82], which may possess distinct properties and introduce additional environmental and health risks.

2.3.2 Cost and Infrastructure

Implementing successful antibiotic removal technology often requires substantial investments in advanced treatment infrastructure and operational costs. While advanced treatment processes like advanced oxidation or membrane filtration may be effective, they are energy-intensive and expensive to implement on a large scale [63]

2.3.3 Low Quantities

Antibiotics are frequently present in the environment in small amounts, usually in the range of parts per billion (ppb) or parts per trillion (ppt) range. Detecting and eliminating them at such low concentrations poses a significant challenge [77]. Additionally, antibiotics may be co-present with a mixture of other pollutants in certain instances, complicating the isolation and targeted removal of antibiotics.

2.3.4 Multiple Sources

Antibiotics can enter the environment through various pathways, including wastewater discharges from healthcare facilities, pharmaceutical industry effluents, agricultural runoff, and human and animal waste [83]. However, effectively locating and regulating each source poses a significant challenge.

2.3.5 Persistence Nature

Certain antibiotics exhibit persistence and resist environmental degradation, resulting in prolonged contamination [84]. Additionally, they are classified as emerging contaminants due to ongoing research on their potential hazards and environmental impacts [85]. Consequently, standardized removal methods may not be readily available.

2.3.6 Limited Public Awareness

Many people may be unaware of how improper antibiotic disposal harms the environment or the importance of antibiotic removal, which can lead to poor practices and pollution. Additionally, in many areas, there may be a lack of regulatory regulations for safe antibiotic levels in water [86], making it challenging to establish treatment targets.

2.4 Mechanism of the Photocatalytic Process for Antibiotic Degradation

The semiconductor-based photocatalysis process effectively promotes the degradation of antibiotics from contaminated water. Researchers have conducted experiments to evaluate the efficacy of various photocatalysts in eliminating different antibiotics from their respective environments. Research on catalyst composition and application has evolved through four distinct generations [87], each shedding light on the mechanisms of various photocatalysts used for pollutant degradation, namely: single component transition metal oxides (TMOs) representing the first generation, doped TMOs/ binary TMOs/ doped binary TMOs as the second generation, and

inactive/active support-immobilized TMOs as the third generation, while the fourth generation refers to ternary/quaternary compositions. The first two generations represent suspended catalysts, the third generation is supported catalysts, and the fourth generation can be suspended or supported. Generally, oxides of titanium (Ti), zinc (Zn), bismuth (Bi), tungsten (W), graphene, and graphitic carbon nitride (g-C_3N_4), also their substitute materials are commonly synthesized and used as photocatalysts for the removal of antibiotics from contaminated sources. These semiconductor materials and their substitutes are synthesized through a variety of advanced methods, including sol-gel, hydrothermal, solvothermal, precipitation, and template-assisted techniques [88]. The synthesis method chosen often depends on factors such as the desired crystal structure, particle size, surface area, and photocatalytic activity required for the specific application

2.4.1 Mechanism of the General Photocatalytic Process

Three main phases can be identified as the fundamental reaction mechanisms of semiconductor photocatalysis for the breakdown of antibiotics from contaminated water: photon absorption, excitation, and reaction [89, 90]. When a photocatalyst absorbs photons with energy higher than its band gap, the electrons in the valence band (VB) get energized and transition to the conduction band (CB), resulting in the formation of a hole (h^+) in the VB (Photocatalyst + $h\upsilon$ → photocatalyst + $h^+ + e^-$) [89, 90]. Afterward, the electrons and holes produced by the light are effectively separated and move toward the surface of the photocatalyst, initiating further reactions on the material surface. Photogenerated holes have the potential to directly target antibiotics (h^+ + antibiotics → $H_2O + CO_2$ + degradation products). This process can possibly result in substantial destruction of the harmful antibiotics. Figure 2.3 illustrates the different phases of the typical photocatalytic decomposition of antibiotics.

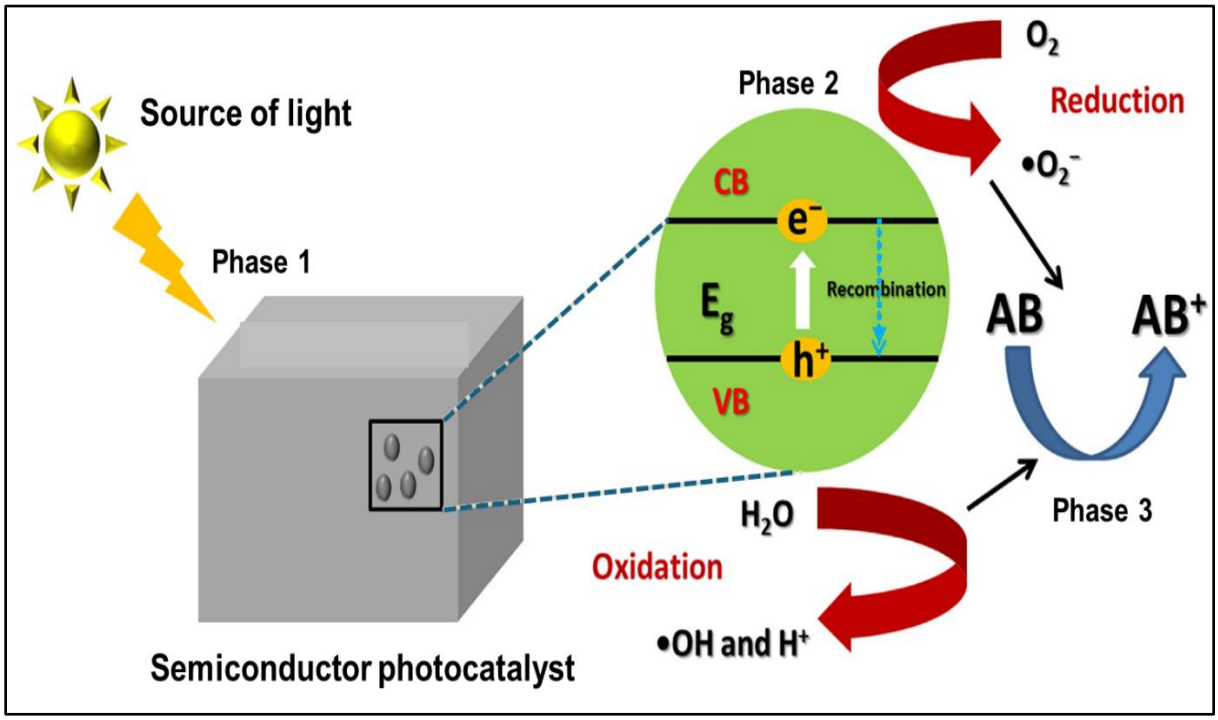

Figure 2.2 General mechanism for antibiotics degradation by using semiconductor-based photocatalysis process.

Materials scientists in this field have suggested and acknowledged two distinct pathways on degradation routes [91]. The first pathway occurs when the semiconductor's CB potential is more negative compared to the $O_2/O_2^{\bullet-}$ redox potential (-0.13 eV vs. normal hydrogen electrode (NHE)). In this reductive pathway, the photoexcited electrons (e^-) have the ability to interact with electron acceptors, like O_2, which can be found on the catalyst surface or dissolved in water. This reaction reduces O_2, forming a superoxide radical anion ($O_2^{\bullet-}$) ($O_2 + e^- \rightarrow O_2^{\bullet-}$) [70, 90]. Additionally, H_2O_2 can be generated by transferring electrons from the conduction band to the adsorbed O_2. Due to the catalyst's CB position's higher negative charge than the O_2/H_2O_2 system (+0.682 eV vs. NHE), the generated H_2O_2 subsequently reacts with electrons released by light to generate the active $HO^{\bullet}$ radicals [70, 92]. The second pathway also known as the oxidative pathway, occurs when the holes migrate to the surface of the photocatalyst. As a result, the presence of $HO^{\bullet}$ radicals was generated by oxidizing H_2O/OH^-, and this generation was influenced by the alkalinity or acidity of the surrounding environment ($H_2O/OH^- + h^+ \rightarrow HO^{\bullet} + H^+$) [70, 92]. Therefore, the

generation of $HO^{\bullet}$ can happen through both pathways: either by oxidizing H_2O or OH^- molecules or by reducing O_2. After the excitation, H^+ possesses the capacity to interact with electrons, generating thermal energy ($H^+ + e^- \rightarrow$ energy). This process results in a reduction in the efficiency of the photodegradation. Notably, the typical redox potential of photocatalysts must exceed that of $HO^{\bullet}/OH^-$ (+1.99 eV vs. RHE)[70, 92]. Both ROS ($HO^{\bullet}$ and $O_2^{\bullet-}$) are highly reactive oxidizing agents in photocatalysis. Under extended exposure to high-energy light, they have the ability to efficiently convert antibiotics and their intermediates into final mineralization products, such as CO_2 and H_2O (Antibiotics + $HO^{\bullet}$ and/or $O_2^{\bullet-} \rightarrow CO_2 + H_2O$).

2.4.2 Mechanism of Metal & Non-metal or Co-doped Photocatalysis Process

The large band gap and significant electron-hole recombination of traditional and single semiconductor photocatalysts limit their effectiveness under visible light, which hinders their practical application. To improve the photocatalytic efficiency, several dopants, such as transition metals (Fe, Cu, Mn, Zn, Ni, Co, Cr, Ru, Ag) or nonmetals (C, N, S, F) have been introduced into the semiconductor material. Metal and non-metal dopants have the ability to construct an impurity energy level located below the CB of the material [93, 94]. This action serves to reduce the band gap, which in turn extends the absorption wavelength edge towards the region of visible light [95, 96]. The idea of modifying semiconductor materials in the second generation involves the process of co-doping with both metal and nonmetal ions. This method has attracted considerable interest because of its synergistic effect on improving the absorption of visible light and minimizing electron-hole recombination [97-99]. However, these synthesized materials not only remove antibiotic pollutants but also help to impact the formation of ROS. The co-doped material provides comparatively higher holes and electrons for the generation of ROS than other doped materials. Shen and their group made a comparable observation regarding the synthesized Co-N co-doped TiO_2 photocatalyst, demonstrating that the co-doped TiO_2 photocatalyst played a significant role in the generation of holes and electrons. Specifically, it contributed

70.1% of the holes and 29.9% of the electrons, in comparison to Co-doped TiO_2 and N-doped TiO_2[95]. This can be attributed to the electron-trapping capabilities of Co ions, which enhance charge transfer and facilitate highly efficient electron-hole separation. The mechanism of doped ions on semiconductor material is shown in Figure 2.3.

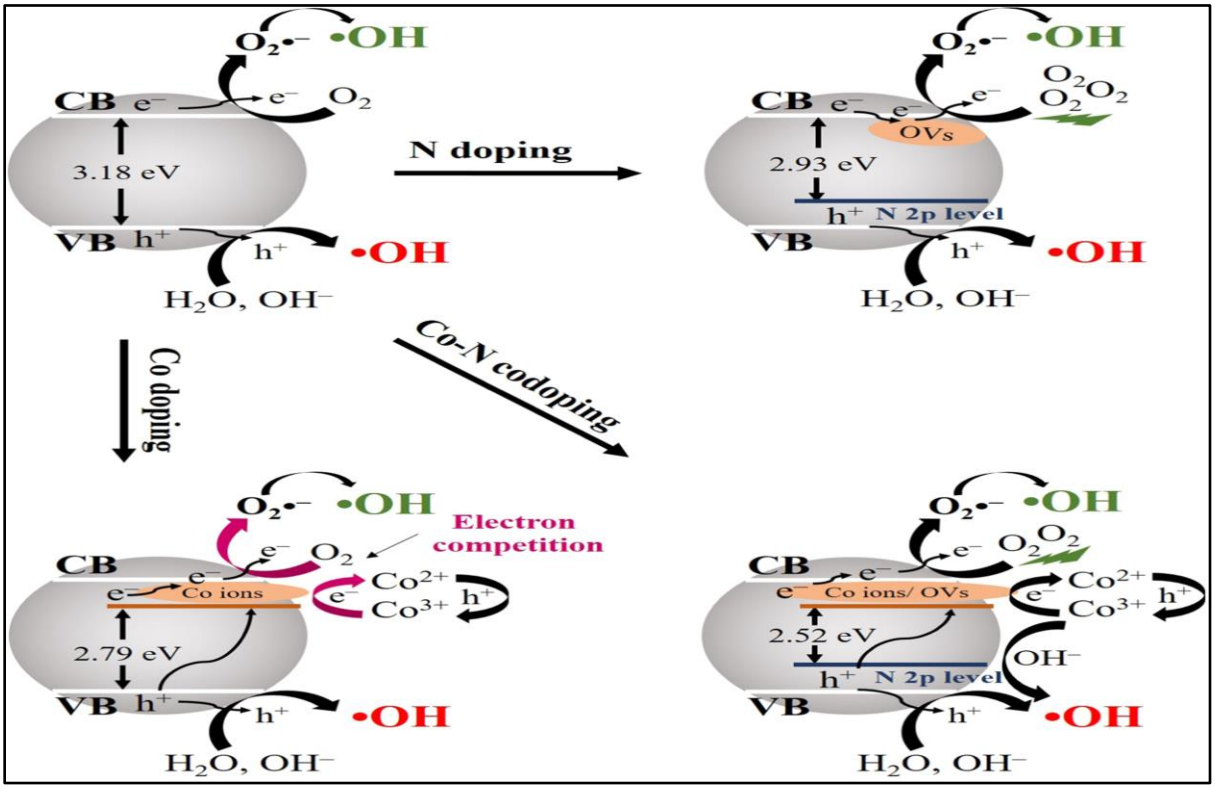

Figure 2.3 The mechanism of doped ions on semiconductor material.

2.4.3 Mechanism of the Heterojunction Photocatalysis Process

Most semiconductor materials are susceptible to electron-hole recombination, which reduces photocatalytic efficacy. As a result, extra efforts must be taken to ensure visible light is used efficiently while avoiding electron and hole recombination. To improve semiconductor material performance, charge carriers should be separated better, their lifespan extended, the photocatalyst's band gap reduced, and the surface area increased [87]. Researchers have taken two approaches to developing effective solar light-activated semiconductor-based photocatalysts. The primary approach is to improve the absorption of visible light of semiconductor materials by including metal or nonmetal elements. This augmentation can be accomplished by modifying the

energy band structure or utilizing localized surface plasmonic resonance (LSPR) events. The second strategy focuses on the development of heterojunctions between a semiconductor and another semiconductor that is activated by visible light [100, 101]. These heterojunctions should have band gaps and energy levels that match the valence and conduction bands. Heterojunctions are primarily composed of (a) Type I heterojunction, (b) Type II heterojunction, (c) p-n junction, (d) Schottky junction, and (e and f) Z-scheme heterojunction, which have all been extensively studied in relation to antibiotic photodegradation [102, 103]. Figure 2.4 depicts the latest developments in heterojunction systems. These heterojunction-based photocatalysts followed the fundamental photocatalytic procedure, except using one semiconductor material. When a potential difference is applied in heterojunction systems, electrons transfer from the conduction band (CB) of semiconductor 1 (SC1) to the CB of semiconductor 2 (SC2). At the same time, holes in the valence band (VB) of SC1 migrate to the VB of SC2. This charge transfer occurs in Type-I heterojunctions, as shown in Figure 2.4a. In Type-II heterojunctions, however, holes move from SC2 to SC 1 (Figure 2.4b). In the p-n junction system, a Type II mechanism exchanges electrons (e^-) and holes (h^+). Electrons travel from p-type to n-type semiconductors, whereas holes move from n-type to p-type semiconductors (Figure 2.4c). The effective segregation of light-induced charge carriers allows the CB of the second semiconductor and the VB of the first semiconductor to engage in reduction and oxidation processes, enhancing the photocatalytic activity. Although Type-II heterojunctions can restrict photogenerated charge recombination, they also reduce compound semiconductors' redox capacity and pose problems to the continuous flow of electrons and holes due to electrostatic repulsion. A Schottky junction is also formed by combining two different semiconductor materials (Figure 2.4d). The oxidation capability of Schottky heterojunctions is restricted to some organic impurities due to the location of the semiconductor photocatalyst's VB. To overcome the aforementioned concerns with other heterojunctions, the concept of Z-scheme heterojunctions was developed, inspired by natural photosynthesis [104-106]. These heterojunctions are classified

based on their charge transfer mechanism and the presence or absence of mediators. The direct Z-scheme relies on the electron transfer between photocatalysts directly, eliminating the electron mediator, which would simplify the design and enhance stability but may suffer from higher charge recombination. In contrast, an indirect Z-scheme, which uses a redox pair (e.g., Fe^{3+}/Fe^{2+}) or a conductive mediator to facilitate efficient charge transfer and spatial separation of charge carriers, reduces the risk of recombination and increases the photocatalytic efficiency. While indirect composites are more complicated to fabricate and possibly beset by stability problems due to mediator degradation, indirect Z-schemes are nevertheless often used in applications that demand high charge separation performance, while direct Z-schemes are best suited for systems where robustness and simplicity are desired. When exposed to visible light, electrons at a lower CB location on SC2 interact with holes on the VB of SC1 via the heterojunction interface (Figure 2.4e) or an intermediary conducting medium (Figure 2.4f). This enables the photocatalyst to maintain high redox capacity.

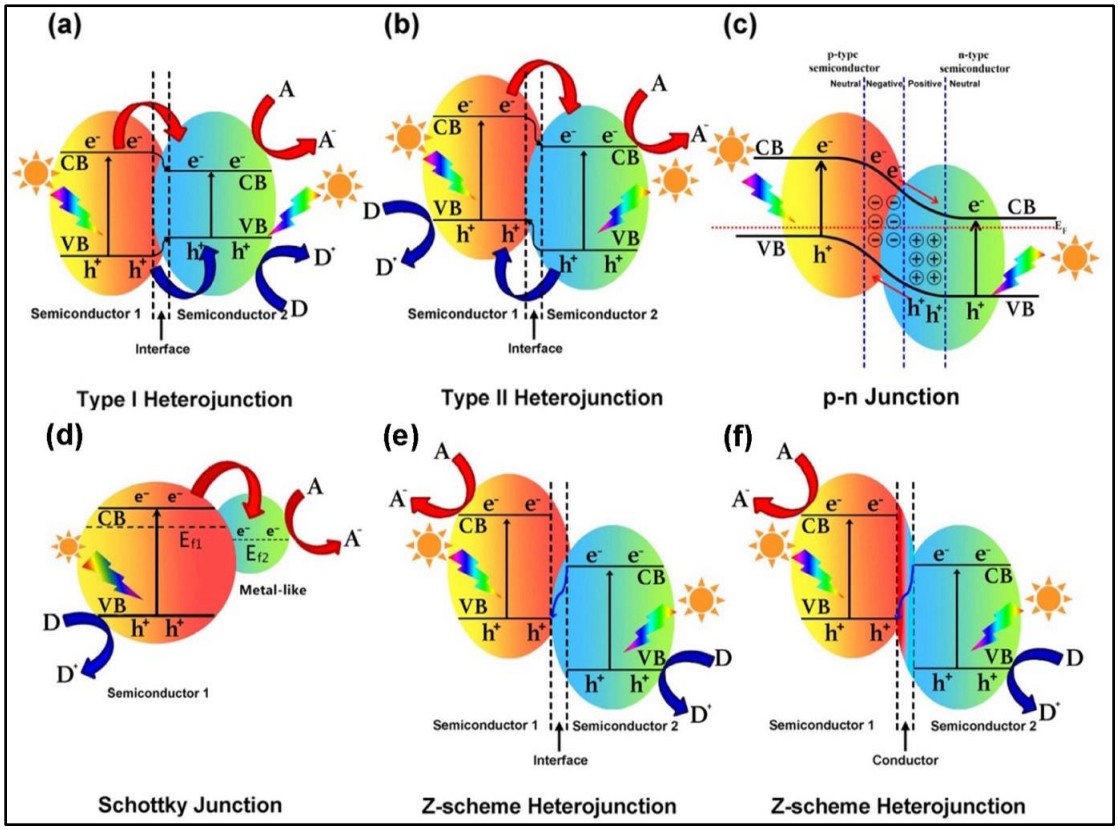

Figure 2.4 The six alternative heterojunction structural models are illustrated as follows: (a) Type I heterojunction, (b) Type II heterojunction, (c) p-n junction, (d) Schottky junction, (e) Z-scheme heterojunction (without an electron mediator), and (f) indirect Z-scheme (with an electron mediator).

2.5 Semiconductor – Based Nanophotocatalyst in Antibiotics Removal

Photocatalysis is a highly effective, affordable, and environmentally friendly approach for removing antibiotics from wastewater. Various semiconductor photocatalysts, such as titanium oxide (TiO_2), zinc oxide (ZnO), bismuth oxyhalide (BiOX), graphitic carbon nitride (g-C_3N_4), and graphene oxide (GO), tungsten oxide (WO_3), and their substituents, have distinct physical and chemical characteristics that influence their efficiency and effectiveness in removing antibiotics. The subsequent sections describe these six commonly used semiconductor materials to remove antibiotics from the environment and their impact on sustainable wastewater treatment.

2.5.1 Titanium Oxide -based Materials or Composites

TiO_2 is the most often used photocatalyst for antibiotic removal owing to its unique features. These substances in nanostructured forms exhibit outstanding physical and chemical durability, a high ratio of surface area to volume, adjustable electronic properties in comparison to the corresponding bulk phase, exceptional photocatalytic performance, lack of toxicity, widespread availability, and cost efficiency [100]. It has a broad bandgap (3.2 eV). Therefore, it can be activated by UV radiation, which is limited in sunlight. This feature makes TiO_2 not suitable for outdoor applications where natural light is abundant. Although TiO_2 has a high photocatalytic activity under UV light, its practical usefulness is limited due to rapid electron and hole recombination and insufficient visible light harvesting [100]. As visible light accounts for most sunlight, developing an effective strategy is critical to enhance the TiO_2 activity under visible light. When using TiO_2 in a full-scale field deployment, reducing the amount and utilizing solar energy can be extremely cost-effective and beneficial to wastewater treatment. Researchers have improved bulk TiO_2 photocatalytic activity through various modifications, including doping with a suitable transition metal, and synthesizing composite materials. Several such advanced photocatalysts have been developed and successfully used to prevent antibiotic contamination, which is shown in Table 2.1. These modifications have led to improved charge separation rates, reduced recombination rates, and the generated oxygen vacancies, ultimately enhancing catalytic efficiency in visible light or solar-simulated light. To enhance the photocatalytic activity, several dopants, such as transition metals, d-block metals or nonmetals or co-doped, have been introduced into the TiO_2 material. The durability of the doped TiO_2 relied on the number of electrons in the dopants and their ionic size.

Although researchers have significantly improved the catalytic efficacy of TiO_2 under visible or solar-simulated light instead of UV light, retrieving the synthesized small particles poses new challenges. Researchers have recently synthesized heterojunctions using TiO_2 and magnetic particles such as α-Fe_2O_3 and Fe_3O_4 to solve the problem of

recovering particles. They accomplished the separation with success, greatly enhancing the efficiency of the catalysts and their potential to be reused, while also decreasing the overall cost of synthesis. The construction of the α-Fe_2O_3@TiO_2 photocatalyst resulted in a higher efficiency in removing cefixime (CFX) antibiotic than pure TiO_2 and Fe_2O_3 under visible light illumination (500 W halogen lamp and wavelength >400 nm) [107]. At a dosage of 0.012 g/L of α-Fe_2O_3@TiO_2, with a pH of 4.76, an initial CFX concentration of 20.5 mg/L, and a duration of 103 minutes, 98% of CFX was effectively removed. The heterojunction formed between the TiO_2 and Fe_2O_3, promoted the electron-holes segregation rate and reduced the rate of recombination, which steered the photodegradation activity. The photocatalyst of TiO_2/GO/chitosan was synthesized by Berna Erim et al. [73] for the degradation of CFX under UV-A irradiation. In optimized conditions (catalyst dose of 0.327 g/L, CFX concentration of 20.29 mg/L, pH of 4.1, and UV-A irradiation of 60 W), the TiO_2/GO/chitosan photocatalyst exhibited a prominent degradation efficiency of 95.34%. They also reported in another article that the SWCNT/ZnO/Fe_3O_4 combination achieved a CFX decomposition efficiency of 94.19% at pH 5.93, 22.76 ppm CFX, and 0.46 g/l photocatalyst [74]. In a recent study, Jeyaprakash and coworkers [75] synthesized Ti^{3+}-doped TiO_2 with oxygen vacancies utilizing ultrasonic treatment for the degradation of tetracycline (TC) via sono-photocatalysis under visible halogen lamp irradiation. The modified-TiO_2 demonstrates remarkable degradation of TC, with an efficiency of approximately 96%, which is 1.56 times higher than that of pure TiO_2 photocatalysts.

2.5.2 Zinc-based Materials or Composites

Zinc oxide (ZnO) is another widely used semiconductor material that exhibits enhanced sensitivity to ultraviolet (UV) light due to its improved electrical band structure. It possesses a substantial surface area, exhibits good thermal stability, is non-toxic, and features a straightforward scope for morphological modification (such as nanorods, nanosheets, nanobelts, etc.). Due to its higher quantum efficiency, it is anticipated to demonstrate superior photocatalytic activity in comparison to pristine

TiO_2, g-C_3N_4, and BiOBr [101]. However, its broader bandgap (3.37 eV) and rapid electron-hole recombination limit its ability to undergo photocatalytic reactions when exposed to visible light [101]. To address these limitations, significant endeavors have been undertaken to improve the properties of ZnO by introducing similar doping ions (non-metals and/or transition metals compounds) on ZnO. This alteration introduces surface defects, leading to a decrease in the bandgap. As a result, the materials become more efficient in harvesting energy to produce reactive species, which is beneficial for applications involving contaminant treatment [96]. Hunge and co-workers [108] synthesized MoS_2/ZnO (MZ) composites with a lower band gap (2.81 eV), which showed higher CIP antibiotic removal efficiency as compared to its single materials (ZnO =43% and MoS_2=50%). A similar approach was also observed for the removal of erythromycin (ERY), spiramycin (SP), and CIP antibiotics by using $ZnIn_2S_4$ [109], g-C_3N_4/ $ZnFe_2O_4$ [110], Cr_2O_3@ZnO [111], ZnO/TiO_2 [112] respectively. However, the application of doped ZnO for remediation purposes is presently impractical due to electron-hole recombination under certain situations.

Scientists have found a variety of adsorbent materials, including biochar, metal-organic frameworks (MOFs), functionalized mesoporous silica, porous organic polymers, zeolite, and derivatives of graphene. These substances act as a support for metal oxide, which serves to increase the catalyst surface area, improve the chemical stability, and immobilize catalysts. Consequently, there is an enhancement in catalytic performance. In a study conducted by Rahman and colleagues [96], it was found that pure ZnO has a very low efficiency (7%) in degrading the metronidazole (MNZ) antibiotic through a photocatalysis process under 180 min irradiation of visible light (wavelength, $\lambda \geq 400$ nm and intensity, ~3×104 lux). However, the efficiency increases to 31.8% when using the N-doped ZnO photocatalyst. In contrast, after 70 minutes of light exposure, the ternary GO-N-ZnO photocatalyst shows a rapid and considerable increase in photocatalytic efficiency of 43.45%. Yu and co-workers [113] synthesized ZnO with N, O-contained biochar (ZnO/NOC) composites, which showed higher TC

antibiotic removal efficiency (97.08%) as compared to its single materials ZnO. The photocatalytic activities of ZnO/NOC were 5.4 and 7.7 times higher than that of pure ZnO for TC (30 mg/L) under ultraviolet and visible lights, respectively. Excellent performance is mainly ascribed to large surface area, ample proper size pore, fast charges transfer, large density and long lifetime of photoinduced charges, and strong interaction between ZnO and N, O-contained biochar [113]. Roy and his colleagues [114] effectively synthesized an rGO-ZnO composite functionalized with ferrocene(Fc) using a simple hydrothermal method. The Fc@rGO-ZnO photocatalyst, as it was first synthesized, exhibited exceptional performance compared to pristine ZnO, resulting in a five-fold increase in CIP and SMX removal efficiency. After three hours of treatment, they removed more than 95% of the antibiotics. The most recent research on the use of ZnO or Zn-based compounds as a photocatalyst to remove antibiotics from water is compiled in Table 2.2.

2.5.3 Bismuth-based Materials or Composites

Although the activity of titanium and zinc oxide-based photocatalysts has been increased through modification, they still have poorer light absorption. Bismuth oxyhalide-based photocatalysts have been widely employed to degrade antibiotics under the illumination of UV and visible light [115, 116]. It also possesses a distinctive electronic structure with the VB containing Bi 6s and O 2p orbitals [89]. This distinctive configuration results in a more pronounced absorption edge in the visible light spectrum. The reciprocal relationship between the anion and cation fosters the creation and migration of holes, thereby promoting improved photocatalytic performance. The inclusion of bismuth in photocatalytic research is justified due to its limited solubility in water, which contributes to the compound's ecological safety. Nevertheless, photocatalysts have certain limitations, including reduced surface area, diminished absorption efficiency, poor heterojunction interface matching, and limited carrier transfer routes [117]. Bi-based materials include various compounds such as sillén-structured BiOX, scheelite-structure ($BiVO_4$, $BiOIO_3$, Bi_2O_3, Bi_2S_3), aurivillius-

structured Bi_2MO_6 (M = Mo, Cr, W), and other composites synthesized with metals and non-metals or heterojunctions for the degradation of antibiotics. Table 2.3 provides comprehensive details and a concise overview of the latest research on bismuth-based photocatalysts used to eliminate antibiotics from wastewater.

Bismuth oxide (Bi_2O_3) is a widely utilized semiconductor in electronics and chemical engineering due to its uncomplicated composition, affordable price, and easy manufacturing process. Bi_2O_3 is widely recognized as a polycrystalline photocatalyst that exhibits four main phases. The majority of these phases are determined to be unstable, with α-Bi_2O_3 appearing at low temperatures and δ-Bi_2O_3 appearing at high temperatures. Scientists have noted that Bi_2O_3 in the metastable phase can undergo a transformation into $(BiO)_2CO_3$, which limits its potential as an effective visible photocatalyst due to its chemical instability [117]. Furthermore, β-Bi_2O_3 exhibits enhanced photocatalytic efficiency in comparison to α- Bi_2O_3. This can be due to the distinctive structure of β-Bi_2O_3, which facilitates the transfer of carriers and prevents their recombination during the process of photocatalysis. Nevertheless, the inherent instability of β-Bi_2O_3 presents a formidable obstacle in the development of uncomplicated techniques for producing pure β-Bi_2O_3, particularly on a nanoscale level. However, the Bi_2O_3 material's photocatalytic efficiency is inadequate for decomposing antibiotics without undergoing modification with suitable dopants. Chen and his colleagues [118] synthesized nano Bi_2O_3 and observed lower degradation of tetracycline (TC). Meanwhile, modification of Bi_2O_3 with MnO_2, changed the morphology from nanorod to nanosheet. This nanosheet structure showed higher TC removal efficiency compared to pure Bi_2O_3, attributed to its increased specific surface area and absorption capacity. Using a one-step hydrothermal process, Wu et al. [104] synthesized Bi-bridged Z-scheme BiOCl/Bi_2O_3 heterojunctions. The constructed binary photocatalysts exhibited 94.79% TC degradation efficiency owing to its enhanced separation of electron-hole (e^-/h^+) pairs and powerful redox capability. The

higher photoactivity was also observed only for other heterostructures like $NiFe_2O_4/Bi_2O_3$ [119], $Fe_3O_4@Bi_2O_3$–RGO [120], $Bi_2O_3/ (BiO)_2CO_3$ [121].

Bismuth oxyhalides (BiOX) are renowned as a favoured photocatalyst due to their distinctive optical and electrical properties, distinguishing them from other promising materials. The distinctive layered structure of BiOX (X = Cl, Br, and I) facilitates efficient separation of charge carriers, resulting in exceptional photocatalytic performance [117]. BiOX includes $[Bi_2O_2]^{2+}$ slabs surrounded by double slabs of $[X]^-$. The band gaps of the different compounds are as follows: BiOF (3.22 eV), BiOCl (2.80 eV), BiOBr (2.36 eV), and BiOI (1.75 eV) [117]. Although BiOCl has a higher bandgap, it is considered a promising photocatalyst compared to the other two BiOI and BiOBr [122]. For example, BiOCl microspheres were able to remove 91.90% of TC after 30 min treatment at a dosage of 500 mg/L of catalyst, with a pH of 4.8, an initial TC concentration of 20 mg/L [123]. Nevertheless, the degrading effectiveness of the photocatalysts reduced as the amount of sorbitol increased. This could be because too much sorbitol has a photo-shielding effect that prevents light and catalyst from coming into direct contact. The improved photodegradation was possible because the catalyst prevented the recombination of e^-/h^+ and facilitated the direct attack of h^+ on the surface of BiOCl [116, 123]. The previous statement was verified by monitoring the relatively lesser effectiveness of BiOI [124] and BiOBr [125] in removing antibiotics. The photocatalytic activity of BiOX varies based on the dipole moment. Photocatalyst efficiency is particularly high when the dipole moment exceeds 2.0 Debye. The hybridization of halogens does not impact electron mobility. However, it does lead to a decrease in hole mobility while perhaps enhancing the separation of charge carriers [126]. In order to enhance the photocatalytic activity of BiOX, significant endeavours have been undertaken, including the creation of heterojunctions or the introduction of metal doping. Wang et al. [116] synthesized BiOCl/Mt photocatalysts by combining montmorillonite (Mt), which is naturally rich in iron, with bismuth nitrate. According to the authors, the composite exhibited 3.4 times higher reactivity than BiOCl when

exposed to visible light. The degradation of TC using the BiOCl/CdS catalyst exhibited a similar tendency, with degradation rates 4.73 and 2.94 times higher than those of pure CdS and BOCl, respectively [127]. Some other heterostructures also exhibited significant photocatalytic activity in the degradation of antibiotics, which are shown in Table 2.3.

Bismuth metal oxides such as Bi_2WO_6, Bi_2MO_6, $BiVO_4$, and $Bi_2Ti_2O_7$ are gaining attention for their possible use in antibiotic degradation, like bismuth oxide and bismuth oxyhalides. The hybrid oxides mostly comprised Bi_2O_3 and various metal oxides such as V_2O_5, W_2O_3, Mo_2O_3, TiO_2, and others. $BiVO_4$ is a newly designed n-type semiconductor with enhanced photocatalytic efficiency. This is attributed to its specific physicochemical features, including ferro-elasticity and ionic conductivity [122]. Regrettably, bismuth-based metal oxides exhibit a diminished light conversion efficiency as a result of the swift recombination of electrons and holes. Several composite photocatalysts have been studied, such as $BiVO_4/MoS_2$, $BiVO_4/FeVO_4$, $AgI/BiVO_4$, $g\text{-}C_3N_4/BiVO_4/rGO$, $Ag/AgBr/BiVO_4$, $CuS/BiVO_4$, $BiVO_4/TiO_2/rGO$, $MnFe_2O_4/BiVO_4$, $BiVO_4/GO/CoFe_2O$, $ZnFe_2O_4/BiVO_4/g\text{-}C_3N_4$ and $BiVO_4$@BiOCl for the degradation of antibiotics, as indicated in Table 2.3. The novel heterostructure of $BiVO_4$-nanosheet and MoS_2-nanoflake composite reported 97.46% degradation of TC antibiotics within 90 min of visible light illumination with 40 mg/L initial concentration at 15 mg/L catalysts loading [128]. Surprisingly, the photocatalytic TC degradation performance decreased to 66.82 when catalysts loading increased to 20 mg/L. The stability of the constructed nanocomposite photocatalysts remained 94.45% after 4^{th} cycle of reuse. The trapping analysis showed that the utilization of scavengers reduced the photodegradation rates.

Bismuth tungstate (Bi_2WO_6) is a semiconductor with n-type conductivity that belongs to the aurivillius family. The material exhibits two distinct crystallographic phases: monoclinic and orthorhombic. Most Bi_2WO_6, which is in an orthorhombic phase, has layers encircled by $(Bi_2O_2)^{2+}$ layers and comprise WO_6 octahedral layers. It comprises

perovskite layers and has a band gap of 2.77 eV. The research community has shown significant interest in zero-dimensional Bi_2WO_6 quantum dots and one-dimensional Bi_2WO_6 nanofibers. Bismuth tungstate exhibits excellent thermal and chemical stability in addition to its activity in visible light. It is typically synthesized through the mixer of $Bi(NO_3)_3$ and Na_2WO_4 using different methods. The distinctive layered structure of this material creates gaps between the slabs that form an electric field. This electric field opposes the movement of h^+ and e^-. This effect decreases the recombination of charge carriers, leading to an increase in the photocatalytic activity. A recent study performed by Wang et al. [129],and found a small amount of Ti addition greatly enhanced the degradation capabilities of Bi_2WO_6 for CAP antibiotic, resulting in an impressive degradation rate of 92.44%. It has been observed by certain researchers that the incorporation of Mg, Fe, Zn, Cu or other transition metals through doping can potentially improve Bi_2WO_6 light absorption capabilities and increase the antibiotic degradation efficiency [130]. Some metal-doped bismuth photocatalysts and their antibiotic degradation efficiency are summarized in Table 2.3.

2.5.4 Graphical Carbon Nitride-based Materials or Composites

Graphitic carbon nitride (g-C_3N_4) is a metal-free semiconductor material with distinct optical, electrical, structural, and physicochemical characteristics [131]. These properties make it well-suited for applications in energy and environmental fields. Due to its narrow bandgap of 2.7 eV, this material can efficiently absorb a significant amount of visible light, which is advantageous for both oxidation and reduction reactions [132]. Nevertheless, some noteworthy concerns arise, such as the elevated rate of electron-hole recombination, limited surface area, restricted number of active sites, slow kinetics of surface reactions, and the diminished mobility of charges, resulting in electron delocalization [131, 132]. The molecular rearrangement of g-C_3N_4 has been the subject of a great deal of recent research because of its potential to alter the surface chemistry and textural structure [133]. This technique reduces carrier transfer resistance, improves pollutant adsorption, broadens light absorption range,

and promotes carrier separation. During the degradation of tetracycline hydrochloride (TCH), it exhibited remarkable activity under visible light and degraded 84.1%, while bulk g-C_3N_4 achieved 52.1% after 90 minutes of irradiation. Recently, researchers have revealed that adding small organic compounds into the precursors of g-C_3N_4 through copolymerization at the molecular level can significantly improve the efficiency of g-C_3N_4. Li et al. [134] conducted a copolymerization of thiourea with 7,7,8,8-Tetracyano-p-benzoquinone methane (TCNQ) to enhance the energy band and electronic structure of g-C_3N_4. The degradation efficiency was 4 times higher for the g-C_3N_4 /TCNQ catalytic system for the degradation of pefloxacin antibiotic compared to the pristine g-C_3N_4. By combining thiourea with 3-aminopyridine, researchers modified the morphology and textural structure of g-C_3N_4, which improved its solar absorption and charge-carrier transportation. The photocatalytic TC decomposition rate was 3.32 times higher in the pyridazine-doped g-C_3N_4 than in the unmodified form [135].

Several studies have shown that heterojunctions formed by combining g-C_3N_4 with other semiconductors with comparable band structures can take advantage of the differences in energy band structures while simultaneously combining the best features of both components. The result is an intrinsic electric field between the materials, which slows down the recombination of photogenerated electrons and holes and speeds up the transfer of photogenerated carriers [136]. By combining ZnO and g-C_3N_4, Wang et al. [137] synthesized a Z-type heterostructure. The newly synthesized composite had greater interlayer spacing, specific surface area, and pore volume. After 120 minutes of simulated light exposure, the rates of TC degradation by pure ZnO, g-C_3N_4, and defective ZnO/g-C_3N_4 composite were found to be 35.20%, 71.48%, and 93.47%, respectively. Due to the existence of N defects, the constructed nanocomposite promotes electron transfer efficiently with less recombination rate. Other g-C_3N_4 heterojunction photocatalysts, like CdS/g-C_3N_4 [138], CoO/g-C_3N_4 [139], P-doped g-C_3N_4/Co_3O_4 [93], and others, have also shown improved photocatalytic

activity (Table 2.4). The binary composite still has several shortcomings. Compared to the binary composite, adding a third semiconductor can improve the separation of charge carriers and expand the range of wavelengths that can be absorbed due to a synergistic effect. As an example, Kumar and colleagues [99] synthesized a ternary S-scheme K, P-g-C_3N_4/GO/$CoFe_2O_4$ photocatalyst, which demonstrated a greater TC removal efficiency compared to the unary and binary heterostructure [99]. The photodegradation efficiency of TC for K, P-g-C_3N_4/GO/$CoFe_2O_4$, K, P-g-C_3N_4/GO, K, P-g-C_3N_4, and g-C_3N_4 was reported to be 85%, 57%, 42%, and 30% after 60 min of visible light exposure, respectively. Likewise, Liu et al. [140] designed a ternary g-C_3N_4/Ag_2CO_3/GO photocatalyst, which follows a double Z-scheme to degrade TC. The ternary system exhibits potent oxidation and reduction capabilities for antibiotic degradation (81.6% within 60 min) compared to binary g-C_3N_4/Ag_2CO_3 composite (67.5% within 60 min). Indirect Z-scheme photocatalytic systems differ from direct Z-scheme systems by incorporating an electron mediator between the two semiconductors. This mediator facilitates the efficient transport and separation of h^+ and e^-. However, the inclusion of an ionic electron transport medium in the traditional Z-scheme photocatalytic system leads to the occurrence of reverse reactions on the surface of photocatalysts, resulting in a decrease in the total number of photogenerated charges. Samsudin and colleagues [141] validated their findings by designing a Z-scheme Ag/$AgVO_3$/g-C_3N_4 photocatalyst. This catalyst exhibited outstanding capabilities in degrading CIP (82.6% within 2h) and generating hydrogen from rainwater. The effective separation and mobility of photo charge carriers were credited to the role of Ag nanoparticles as electron mediators. There are some other observations, which are shown in Table 2.4.

2.5.5 Graphene Oxide-based Materials or Composites

Graphene is a monolayer of carbon atoms organized in a hexagonal lattice, with various types of defects present around the edges. This material is categorized based on the level of surface oxidation, which includes pristine graphene, graphene oxide (GO), and reduced graphene oxide (rGO). Among the derivatives of graphene, GO and rGO are frequently used to support photoactive materials and immobilize pollutants. Additionally, they serve as crucial interfaces for electron carriers, augmenting light absorption and antibiotic pollutants' adsorption through their functional groups [142]. Graphene derivatives possess two notable drawbacks: they are more expensive than other carbon compounds, and their normal synthesis procedure requires using dangerous oxidizing and reducing agents [142]. Therefore, it is crucial to utilize direct, secure, economical, and eco-friendly synthesis methods to use these materials as photocatalysts. Graphene oxide (GO) has attracted public interest as another metal-free carbon material, owing to its two-dimensional ultra-thin layered structure, robust stability, and remarkable capacity to transport charge carriers [142]. When coupled with suitable semiconductor materials or modified to other forms of heterostructures, it can enhance the photocatalytic efficiency for various applications, including water purification. GO-based photocatalysts can facilitate this process by generating electron-hole pairs upon absorption of photons. Recently, Kumar et al. [99] fabricated a K, P co-doped g-C_3N_4/$CoFe_2O_4$ catalyst with GO, which demonstrated an 85% degradation rate for TC and 99% degradation rate for doxycycline antibiotics within a 60-minute of treatment time. The degradation efficiencies were improved through doping and further enhanced by adding GO and magnetic $CoFe_2O_4$. Numerous ternary compounds (Table 2.5) incorporating GO as a co-catalyst have been employed in the photocatalysis field to remove antibiotics. For instance, g-C_3N_4/Ag_2CO_3/GO [140], BiOBr/MoS_2/GO [143], g-C_3N_4/GO/$CoFe_2O_4$ [99].

Reduced graphene oxide (rGO) is also considered as one of the promising semiconductor materials, but its characteristics can differ based on the level of reduction and the specific production techniques employed. GO is a type of insulating material that is made from graphene by oxidizing graphite. The reduction process eliminates functional groups in GO that contain oxygen, restoring π-conjugated structures and electrical conductivity. Bulk rGO has a uniform tendency to attract molecules, but its ability to react to light is limited due to its broad bandgap and inefficient absorption of light. Therefore, adding suitable material or modifications to the basal catalyst considerably improves photo-catalysis efficiency [114]. For instance, combining TiO_2 and rGO makes it more energy-efficient than traditional photocatalysts such as TiO_2. The enhanced activity of these heterojunctions mainly occurred in solar-simulated light and removed around 87% of SMX within one hour [144]. Similarly, adding Ag_3PO_4 in N-doped rGO photocatalyst degrades higher concentrations of SMX at the same time [145]. Incorporating metal oxide (MO) into rGO enhances the photosensitization. The process of sensitizing different antibiotics in wastewater through photoactive oxidation has been previously investigated utilizing various materials such as rGO/WO_3, g-C_3N_4/$BiVO_4$/rGO, $BiVO_4$/TiO_2/rGO, rGO/$Bi_4O_5Br_2$, rGO-$BiVO_4$-ZnO, rGO-ZnO, Ferrocene-rGO-ZnO, α-Fe_2O_3/ZnO/rGO, CdS-Bi_2MoO_6/rGO and rGO modified tin selenide (SnSe) etc., which are summarized in Table 2.5.

2.5.6 Tungsten Oxide-based Materials or Composites

Tungsten trioxide (WO_3) is considered environmentally benign, making it a preferable option for eco-friendly water treatment applications. In aqueous solutions, WO_3 is mechanically strong and physiochemically stable, and the synthesis of high-purity WO_3 is a good option for the degradation of antibiotics under solar light irradiation [146]. WO_3 is a catalyst that responds to visible light and has consistent physicochemical properties because of its low band gap energy (2.4 to 2.8 eV) [146]. However, the usage of this material in the environmental remediation process is questionable [147-149] due to the fact that the electrons generated by light in the CB of WO_3 (about +0.5 V vs. NHE) have a weaker positive potential as compared to the reduction potential of O_2 ($O_2/O_2^{\bullet-}$ = − 0.33 V vs. NHE). Diverse approaches have been suggested to enhance its photocatalytic activity. For example, g-C_3N_4-WO_3 [147], rGO/WO_3 [148] and multi-walled carbon nanotubes-WO_3 [150] were found to be photodegraded SMX under 300 W Xenon Arc solar simulator light. Three catalysts showed remarkable degradation of SMX, with degradation rates of 91.7%, 98.0%, and 88.5%, respectively, compared to bare WO_3. Various composites were synthesized using a simple anion-exchange approach, including AgI/WO_3 [151], Ag_3VO_4/WO_3 [149], AgCl/Ag_3PO_4/g-C_3N_4 [152]. These composites were prepared by adding different molar ratios of AgX. With the inclusion of AgX, there was a significant enhancement in the removal rate of antibiotics. This was achieved by augmenting the positive potential and accelerating electron transfer rates. The most recent research on using tungstate as a photocatalyst to remove antibiotics from water is compiled in Table 2.6.

Table 2.1. Degradation antibiotics by TiO_2-based photocatalytic process

Name of Antibiotics	Dosages of antibiotics and catalysts	Light source and other parameters	Removal efficiency (%)	Reaction time (min)	Reference
Clarithromycin	0.1 mg/L of CLA 100 mg/L of Graphene-based TiO_2	1000 W Xenon lamp Simulated sunlight, pH = 6, RWW	86.0	60	[144]
Sulfamethoxazole	10 mg/L of SMX 1250 mg/L of TiO_2/pBC	50 W Xenon lamp Visible light, pH = 4 to 10, SWW	91.27	180	[153]
Sulfamethoxazole	10 mg/L of SMX 1250 mg/L of Zn-TiO_2/pBC	50 W Xenon lamp Visible light, pH = 4, RWW	81.21	180	[154]
Sulfamethoxazole	30 mg/L of SMX 1000 mg/L of F-Pd doped-TiO_2	320W Xenon lamp Simulated light, pH = -,UPW	94.2	20	[155]
Ciprofloxacin	0.5 mg/L of CIP 0.43 g/L of black Ti^{3+}/N-TiO_2 (b-N-TiO_2)	5 W LED bulb Visible light, pH = 6.7, UPW	98.5	70	[156]
Ciprofloxacin	75 uM of CIP/ LEV 1000 mg/L of N and C co-doped TiO_2	300 W Xenon lamp Visible light, pH = -, RWW	68.7	120	[98]
Levofloxacin			95.7		
Tetracycline	10 mg/L of TC/ CTC	300 W Xenon lamp	87.03	60	[157]

Chlortetracycline	300 mg/L of TiO_2-MOF	Visible light, pH = 7, UPW	78.91		
Ceftriaxone	100 mg/L of CTR 1 g/L of activated carbon based TiO_2	50 W LED bulb Visible light, pH = -, RWW	99.6	240	[158]
Enrofloxacin	10 mg/L of ENF 1 g/L of MX-TiO_2 composite	UVA lamp, 2.1mW/cm^2 pH = 4.8, UPW	91.6	300	[159]
Cefixime	20.5 mg/L of CFX 0.012 g/L of α-Fe_2O_3@TiO_2	500 W Halogen lamp Visible light, pH = 4.8, SWW	98.8	103	[107]
Tetracycline	20 mg/L of TC 0.01 g/L of Ti^{3+} doped-TiO_2	500 W Halogen lamp Visible light, pH = 4.7, SWW	96	60	[160]

Table 2.2. Degradation of antibiotics by zinc-based photocatalytic process

Name of Antibiotics	Dosages of antibiotics and catalysts	Light source and other parameters	Removal efficiency (%)	Reaction time (min)	Reference
Erythromycin	10 mg/L of ERY 50 mg/L of $ZnIn_2S_4$	100W Iodine-gallium lamp Visible light, pH = -, UPW	100	180	[109]
Spiramycin	20 mg/L of Spiramycin 1000 mg/L g-C_3N_4/$ZnFe_2O_4$	300 W Xenon lamp Visible light pH = -, UPW	95.0	240	[110]
Tetracycline	40 mg/L of TC 1000 mg/L of Ag_3PO_4/Zn-Al LDH	500 W Xenon lamp Simulated sunlight pH = -, UPW	96	90	[161]
Ciprofloxacin	10 mg/L of CIP 500 mg/L of $ZnSnO_3$	350 W Xenon lamp Simulated sunlight pH = 5.9, SWW	85.9	100	[162]
Ciprofloxacin	10 mg/L of CIP 1g/L of Cr_2O_3@ZnO	300 W Xenon lamp Visible light pH = 3.5, UPW	100	30	[111]
Tetracycline	30 mg/L of TC 1g/L ZnO and N, O-contained biochar (ZnO/NOC)	350 W Xenon lamp sunlight pH = 6, UPW	97.08	140	[113]

Ciprofloxacin	0.05 mg/L of CIP 2g/L of MoS_2/ZnO composites	250 W Metal halide lamp Ultraviolet light pH = - , UPW	96.18	120	[108]
Tetracycline	40 mg/L of TC 200 mg/L of ZnO/ TiO_2 composites	300 W Xenon lamp Simulated sunlight pH = -, UPW	84.06	120	[112]

Table 2.3. Degradation of antibiotics by bismuth-based photocatalytic process

Name of Antibiotics	Dosages of antibiotics and catalysts	Light source and other parameters	Removal efficiency (%)	Reaction time (min)	Reference
Tetracycline	20 mg/L of TC 1g/L of BiOBr	10 W LED lamp Visible light, pH = 6.35, DW	80.3	90	[125]
Ofloxacin	10 mg/L of OFX/ CIP/ NOR 250 mg/L of BiOCl	125 W Mercury lamp UV light, pH = 7, UPW	93.0	80	[115]
Norfloxacin			92.0	240	
Tetracycline	20 mg/L of TC 10 mg/L of CIP/ NOR 500 mg/L of BiOCl	250 W Xenon lamp Visible light, pH = 7, UPW	91.90	30	[123]
Ciprofloxacin			82.11	120	
Norfloxacin			74.52	120	
Ciprofloxacin	10 mg/L of CIP 500 mg/L of BiOCl/NGQDs	300 W Xenon lamp Visible light, pH = 7, DW	94.0	10	[163]
Ciprofloxacin	20 mg/L of CIP 1000 mg/L of Ti_3C_2-Bi/BiOCl	300 W Xenon lamp pH = -, UPW	89.0	100	[164]
Tetracycline	10 mg/L of TC 667 mg/L BiOCl/CdS	300 W Xenon lamp Visible light, pH= -, UPW	95.9	60	[127]
Oxytetracycline	10 mg/L of OTC 250 mg/L g-C_3N_4/BiOCl/CdS	Natural sun light pH = 7, DW	99.0	240	[165]
Tetracycline	10 mg/L of TC 200 mg/L BiOCl/Bi–Bi_2O_3	300 W Xenon lamp Visible light, pH = -, UPW	94.79	150	[104]

Tetracycline	20 mg/L of TC 400 mg/L $BiOCl_{0.9}I_{0.1}$/β-Bi_2O_3	350 W Xenon lamp Simulated light, pH = 6, UPW	82.4	120	[166]
Tetracycline	45 mg/L of TC 200 mg/L MnO_2/Bi_2O_3 300 mg/L of PMS	300 W Xenon lamp Visible light, pH = 6.5, UPW	73.34	100	[118]
Tetracycline	10 mg/L of TC/ CTC/ OTC/ DOX 1000 mg/L of $BiVO_4$/TiO_2/RGO	1000 W Xenon lamp Visible light, pH = -, UPW	96.2	120	[167]
Chlortetracycline			97.5		
Oxytetracycline			98.7		
Doxycycline			99.6		
Tetracycline	190 mg/L of TC 500 mg/L of $BiVO_4$/ MoO_3	300 W Xenon lamp Solar light, pH = 4.52, UPW	97.66	160	[168]
Tetracycline	10 mg/L of TC 250 mg/L of $MnFe_2O_4$/$BiVO_4$	300 W Xenon lamp Visible light, pH = -, UPW	92.0	120	[169]
Tetracycline	40 mg/L of TC 1.5 g/L of $BiVO_4$/MoS_2	100 W Xenon lamp Visible light, pH = -, UPW	97.46	90	[128]
Lomefloxacin	25 mg/L of LOM 0.5 g/L of $ZnFe_2O_4$/$BiVO_4$/g-CN	300 W Xenon lamp Visible light, pH = -, UPW	96.1	105	[170]
Tetracycline	40 mg/L of TC, 10 mg/L of CIP 1.0 g/L of $BiVO_4$@BiOCl	500 W Xenon lamp Visible light, pH = -, UPW	90.32	200	[171]
Ciprofloxacin			71.32		
Tetracycline	15 mg/L of TC 500 g/L of Bi_2WO_6/ $CuBi_2O_4$	300 W Xenon lamp Visible light, pH = -, UPW	91.0	60	[172]

Ciprofloxacin	10 mg/L of CIP/ NOR 1g/L of Mg/Bi_2WO_6	300 W Xenon lamp Visible light, pH = -, UPW	99.1	150	[130]
Norfloxacin			89.44		
Norfloxacin	10 mg/L of NOR 600 mg/L of Ag_3PO_4/Bi_2WO_6/MWCNTs	1000 W Xenon lamp Visible light, pH = -, UPW	94.34	180	[173]
Ciprofloxacin	10 mg/L of CIP 0.5 g/L of Co_3O_4/Bi_2WO_6/PMS 0.2 g/L of PMS	300 W Xenon lamp Visible light, pH = 6.5, UPW	86.2	5	[174]
Ciprofloxacin	10 mg/L of CIP 5 mg/L of Bi_3TaO_7 QDs/g-C_3N_4	86 W blue LED lamp pH = 7, UPW	91.0	120	[105]
Sulfamethoxazole	5 mg/L of SMX 500 mg/L of Ag/g-C_3N_4/Bi_3TaO_7	300 W Xenon lamp Visible light, pH = 6.5, UPW	98	25	[106]
Ciprofloxacin	20 mg/L of CIP 250 mg/L of CdS-Bi_2MoO_6/RGO	500 W Xenon lamp Visible light, pH = -, UPW	91.0	60	[175]
Tetracycline	15 mg/L of TET 600 mg/L of $CuInS_2$/Bi_2MoO_6	300 W Xenon lamp Visible light, pH = 7, UPW	84.7	120	[176]
Ciprofloxacin	10 mg/L of CIP;20 mg/L of TC 250 mg/L of $Bi_4O_5Br_2$/CdS	350 W Xenon lamp Visible light, pH = -, UPW	85	60	[177]
Tetracycline			85	60	
Norfloxacin	10 mg/L of NOR 250 mg/L of ZnO/Bi_2WO_6	Natural sunlight pH = 6.6, UPW	99.7	120	[178]
Levofloxacin	15 mg/L of LEV	100 W LED lamp	92.5	120	[179]

	900 mg/L of Bi_2CrO_6/g–C_3N_4	Visible light, pH = 6, UPW			
Chlortetracycline	20 mg/L of CTC 0.9 g/L of Bi_2WO_6/g-C_3N_4/ACF	300W Xenon lamp Visible light, pH = -, SWW	90.2	69	[180]
Ciprofloxacin	10 mg/L of CIP 20 mg/L of TC 500 mg/L of $BiVO_4$/Bi_2WO_6/WO_3	300W Xenon lamp Simulated light, pH = 6, UPW	67.5	100	[181]
Tetracycline			33.2	75	
Tetracycline	20 mg/L of TC/ OTC 400 mg/L of In_2O_3/Bi_2WO_6	300 W Xenon lamp Simulated light, pH = -, UPW	86	70	[182]
Oxytetracycline			82		
Norfloxacin	10 mg/L of NOR/ LEV 400 mg/L of g-C_3N_4/Bi_2WO_6	300 W Xenon lamp Simulated light, pH = -, UPW	85.75	120	[183]
Levofloxacin			85.82		
Chloramphenicol	50 mg/L of CHL 1g/L of Ti-Bi_2WO_6@BC	500 W Xenon lamp Visible light, pH = 7, UPW	92.44	120	[129]

Table 2.4. Degradation of antibiotics by g-C_3N_4-based photocatalysis process

Name of Antibiotics	Dosages of antibiotics and catalysts	Light source and other parameters	Removal efficiency (%)	Reaction time (min)	Reference
Tetracycline	40 mg/L of TC 400 mg/L of g-C_3N_4	300 W Xenon lamp Visible light, pH = 4.18, UPW	84.1	90	[133]
Tetracycline	20 mg/L of TC 1 g/L of Nb_2O_5/g-C_3N_4	250 W Xenon lamp Simulated sunlight, pH = 3, SWW	90.1	150	[184]
Sulfamethazine	10 mg/L of SMT 101g/L of C doping g-C_3N_4	300 W Xenon arc lamp Visible light, pH = -, UPW	98.0	60	[185]
Sulfamethazine	30 mg/L of SMT 500 mg/L of g-C_3N_4	300 W Xenon arc lamp Visible light, pH = 3, UPW	99.7	60	[186]
Erythromycin	50 mg/L of ERY 500 mg/L of CdS/ g-C_3N_4	35 W Xenon lamp Visible light, pH = 5, UPW	81.02	60	[138]
Tetracycline	150 mg/L of TC 400 mg/L of CoO/g-C_3N_4	300 W Xenon lamp Visible light, pH = -, UPW	73.12	300	[139]
Metronidazole	10 mg/L of MTZ 1000 mg/L of P-doped g-C_3N_4/Co_3O_4	250 W Xenon lamp Visible light, pH = -, UPW	70	180	[93]
Sulfamethoxazole	5 mg/L of SMX 1000 mg/L Ag-P co-doped g-C_3N_4	350 W Xenon lamp Visible light, pH = 9, SWW	99	30	[97]

Sulfamethazine	5 mg/L of SMT 200 mg/L 2D/1D g-C_3N_4/TNTs	450 W Xenon lamp pH = 7, UWW	100	300	[187]
Tylosin	25 mg/L of TYL 500 g/L of Sm-doped gC_3N_4	35 W Xenon lamp Simulated sunlight, pH = 3-11, UPW	78.4	90	[94]
Tetracycline	50 mg/L of TC 11 g/L of ZnO/g-C_3N_4	500 W Mercury lamp UV light, pH = -, RWW	93.4	120	[137]
Tetracycline	10 mg/L of TC 10 mg/L of Pyridazine doped g-C_3N_4	300 W Xenon lamp Visible light, pH = 6, UPW	95	60	[135]
Pefloxacin	10 mg/L of PEF /ENR/CIP 50 mg/L of g-C_3N_4/TCNQ-X	300 W Xenon lamp Visible light, pH = -, UPW	91.6	180	[134]
Tetracycline	8×10^{-5} M of TC / DOX 60 mg/L of K, P co-doped g-C_3N_4/GO/$CoFe_2O_4$	500 W halogen lamp Visible light, pH = 7, UPW	85	60	[99]

Table 2.5. Degradation of antibiotics by graphene oxide-based photocatalysis process

Name of Antibiotics	Dosages of antibiotics and catalysts	Light source and other parameters	Removal efficiency (%)	Reaction time (min)	Reference
Amoxicillin	50 mg/L of AMX 400 mg/L of GO/TiO_2	36 W UV lamp UV light, pH = 6, UPW	99	60	[188]
Tetracycline	50 mg/L of TC 50mg/L of GO/ZnO	300 W Xenon lamp Visible light, pH = 11, UPW	74	100	[189]
Tetracycline	20 mg/L of TC 30 mg/L of g-C_3N_4/Ag_2CO_3/GO	300 W Xenon lamp Visible light, pH = -, UPW	97.6	100	[140]
Ciprofloxacin	10 mg/L of CIP 20mg/L of $BiPO_4$@GO-MMIPs	300 W Xenon lamp Visible light, pH = -, UPW	100	80	[190]
Tetracycline	20 mg/L of TC 25 mg/L of BiOBr/MoS_2/GO	300 W Xenon lamp Visible light, pH = 11, UPW	98	40	[143]
Trimethoprim	20 mg/L of TMP 2.5 mg/L of CuFe-LDH/GO	18 W Philips TL-D UV light, pH = 8.8, UPW	90.8	120	[191]
Sulfamethoxazole	0.10 mg/L of SMX 100 mg/L of TiO_2-rGO	1000 W Xenon lamp Simulated sunlight, pH = 5.2-6.2, RWW	87.0	60	[144]
Sulfamethoxazole	20 mg/L of SMX 200 mg/L of Ag_3PO_4/N-doped rGO	250 W Xenon arc lamp Visible light, pH = 5.8, UPW	93.8	60	[145]

Ciprofloxacin	10 mg/L of CIP 300 mg/L of rGO-$BiVO_4$-ZnO	Tungsten lamp Visible light, pH = 7, UPW	98.4	60	[192]
Ciprofloxacin	10 mg/L of CIP 20 mg/L of NOR/TC 50 mg/L of rGO/$Bi_4O_5Br_2$	500 W of Xenon lamp Visible light, pH = -, UPW	97.6	60	[193]
Norfloxacin			80.7		
Tetracycline			98.7		
Chloramphenicol	1000 mg/L of CAP 500 mg/L of rGO-ZnO	4 W of UVP Compact lamp UV light, pH= 2, UPW	90.8	40	[194]
Oxytetracycline	10 mg/L of OTC 300 mg/L of cobalt ferrite/rGO	300 W Xenon lamp Vis. light, pH=7.36, UPW	84.7	40	[195]
Tetracycline	25 mg/L of TC 25 mg/L of rGO/MoO_3/TiO_2	300 W Xenon lamp Visible light, pH = -, UPW	94	80	[196]
Ciprofloxacin	10 mg/L of CIP/SMX 25 mg/L of Fc@rGO-ZnO	10 W UV lamp UV light, pH = 4, UPW	97.09	180	[114]
Ofloxacin	40 mM of OFX 20 mg/L of rGO-ZnS-CuS	Tungsten lamp (300 mW/cm^{-2}) Visible light, pH = -, UPW	86.65	135	[197]
Oxytetracycline	20 mg/L of OTC 370 mg/L of rGO/α-Fe_2O_3/ZnO 2.06 mM of PS	24 W LED bulb Visible light, pH = 4, UPW	98	90	[142]
Norfloxacin	10 mg/L of NOR 0.75 mg/L of rGO–SnSe	300 W Xenon lamp Visible light, pH = 7, UPW	90.7	70	[198]

Table 2.6. Degradation of antibiotics by tungsten oxide-based photocatalysis process

Name of Antibiotics	Dosages of antibiotics and catalysts	Light source and other parameters	Removal efficiency (%)	Reaction time (min)	Reference
Sulfanilamide	10 mg/L of SAM 500 mg/L of Ag doped WO_3	200 W Xenon arc lamp Visible light, pH = 5, UPW	96.2	300	[199]
Tetracycline	35 mg/L of TC 1000 mg/L of AgI/WO_3	300 W Xenon lamp Visible light, pH = 6.62, UPW	75.0	60	[151]
Tetracycline	10 mg/L of TC 500 mg/L of Ag_3VO_4/WO_3	300 W Xenon lamp Visible light, pH = -, UPW	71.2	30	[149]
Sulfamethoxazole	10 mg/L of SMX 1 g/L of WO_3/g-C_3N_4	300 W Xenon lamp Simulated sunlight, pH = -, UPW	91.7	240	[147]
Sulfamethoxazole	10 mg/L of SMX 2 g/L of WO_3/rGO	200 W Xenon arc lamp Simulated sunlight, pH = 7, RWW	98.0	80	[148]
Sulfamethoxazole	10 mg/L of SMX 2 g/L of WO_3-MWCNTs	300 W Xenon arc lamp Simulated sunlight, pH = -, UPW	88.5	180	[150]
Tetracycline	50 mg/L of TC 50 mg/L of Cu-doped WO_3	300 W Xenon lamp Visible light, pH = 10, UPW	93.7	60	[200]
Levofloxacin	20 mg/L of LVX 50 mg/L of WO_4	300 W Xenon lamp Visible light, pH = 7, UPW	84.3	120	[201]

2.6 Conclusions and Perspectives

This study thoroughly examines the most recent developments and obstacles related to the use of semiconductor-based photocatalysts for the degradation of antibiotic pollutants in the environment. It underscores the detrimental effects of antibiotic emissions on ecosystems and public health. The research delves into the processes involved in photocatalytic degradation, which depend on the production of free radicals and reactive oxygen species. Although the application of solar radiation and visible light sources for photocatalytic activation is currently constrained, there is an urgent necessity for further investigation and advancement in this domain. Therefore, concentrating on long-term antibiotic removal efficacy and conducting in-depth studies on intermediate by-products is crucial.

The review also comprehensively discusses various techniques to enhance the photocatalytic performance of semiconductors. These methods include altering the morphology and structure, constructing heterojunctions, incorporating metals and non-metals onto the photocatalyst surface, and making surface/interface modifications. These strategies have demonstrated notable enhancements in the effectiveness of antibiotic degradation, either by reducing the band gap of the photocatalyst or improving the movement of photogenerated charge carriers, thus facilitating efficient charge separation. Together, these innovations contribute to the development of sustainable and highly effective photocatalytic systems.

However, despite these encouraging findings, several challenges must be confronted. These challenges encompass the existence of multiple sources of contaminants in wastewater, the intricate nature of antibiotics, the necessity to comprehend the mechanisms of photocatalytic degradation at the atomic scale,

and the creation of catalysts capable of withstanding adverse influences from environmental factors.

To further advance the field of photocatalysis, future research should delve into new and innovative approaches, including developing novel materials, optimizing catalyst preparation methods, enhancing photocatalyst recycling capabilities, and exploring synergistic treatments. The focus should be on designing photocatalysts with quasi-same photoactivity and ease of separation to minimize waste and reduce operating costs. It is also suggested that cost-efficiency analysis be performed, including energy requirements for conventional treatment methods such as AOPs with photocatalysis process, to ensure large-scale wastewater treatment.

Extensive research on sustainable and recyclable photocatalysts is urgently needed to tackle environmental concerns related to antibiotic degradation effectively. Strong political support, adequate funding, and effective interdisciplinary collaboration are crucial for advancing progress in this field and successfully applying laboratory findings to real-world solutions. Through careful consideration of these challenges and utilization of cutting-edge technologies, semiconductor-based photocatalytic active nanomaterials offer a promising opportunity to mitigate antibiotic pollution and protect the well-being of our environmennd society.

Chapter 3: MATERIALS AND METHODOLOGY

3.1 Chemical and Reagents

Copper (II) sulfate pentahydrate (99.5 %, Merck),, Sodium Tungstate Dihydrate (98 %, Sisco research lab), Cetyltrimethyl ammonium bromide (99%, SRL),NaOH(Researchlab), Absolute Ethanol (SigmaAldrich), Tetraethoxysilane (TEOS, 98%, Alfa Aesar), Hexadecylamine (HDA, TCI,>95%), Titanium Isopropoxide (TTIP, 27.8-28.6% TiO_2, Sisco Research lab), Ammonia (25%, Merck KGaA), Methylene Blue (Smart Lab) , Sodium Azide (99.5%, SigmaAldrich), Triethanolamine (98%, SigmaAldrich), Iso Propyl alcohol (99.8%, Research lab), Superoxide Dismutase bovine (30KU, SigmaAldrich), Potassium Dichromate (BDH Chemical Ltd., England), Chitosan(Sisco Research Laboratories Pvt. Ltd, India), Ultrapure water (≥18.2 MΩ-cm, Direct-Q®3 UV Water purification System).

3.2 Instruments

The instruments and apparatus used for the synthesis and the photocatalytic activity of $CuWO_4$@TiO_2 are as follows: Digital balance (BEL M254Ai), Hotplate magnetic stirrer (MS-H380-Pro, USA), Direct-Q®3 UV Water purification System, Centrifuge machine (CTF-TH16, China), Sonicator (Hwashin Powersonic 405, Korea), Hot air Oven (Memmert UN55), Vortex, UV-Vis spectrophotometer (T80+, UK), Xenon Light Source (Perfect light PLS-SXE300UV, China), Potentiostat (μStat-i 400s Potentiostat / Galvanostat / Impedance Analyzer), DMol3 module, Centrifuge machine.

3.3 Synthesis of $CuWO_4$@TiO_2

The photocatalyst was synthesized through a two-step process using the hydrothermal method. Firstly, the core $CuWO_4$ was synthesized by mixing the required amount of copper (II) sulfate pentahydrate (0.01 M) and sodium tungstate dihydrate (0.01 M) in 150 mL of water. After that, the required amount of cetyltrimethyl ammonium bromide (CTAB) was added to the solution, mixed properly for around 1 hour, and then added to the NaOH solution to keep the pH at 10. Finally, the suspension was placed in a Teflon-lined stainless-steel autoclave (200 mL) and reacted for 24 h at 160 °C. Following a natural cooling of the autoclave to ambient temperature, the adsorbent was collected and repeatedly washed in deionized water and absolute ethanol before being dried at 70 °C. Secondly, the TiO_2 was coated on the core $CuWO_4$ material. Typically, 0.1 g of $CuWO_4$ material was homogeneously dispersed in ethanol (9.74 mL) using ultrasonication. Then tetraethyl orthosilicate (TEOS) and hexadecylamine (HDA) were added, and the mixture was stirred at room temperature for 1 minute to form uniform dispersion. Next, 0.2 mL of titanium isopropoxide (TIP) was added to the dispersion and stirred for 10 minutes. The resulting $CuWO_4$@SiO_2@TiO_2 product was collected by centrifugation. After that, the $CuWO_4$@SiO_2@TiO_2 precursor was dispersed in a mixture of 20 mL of ethanol and 10 mL of water with an ammonia solution (0.5 M). This mixture was then sealed in a 200 mL Teflon-lined autoclave and placed at 160 °C for 20 hours before being cooled to room temperature. Finally, the $CuWO_4$@TiO_2 nanomaterial was collected by centrifugation and washed with water and ethanol several times. After that, the catalyst was overnight dry and then calcined at 500°C for 2 hours.

3.4 Characterization of $CuWO_4$@TiO_2 nanocomposite

Synthesized $CuWO_4$@TiO_2 Photocatalysts were characterized through different physiochemical characterization processes. The optical properties of the synthesized nanocomposites were analyzed using UV-Vis diffuse reflectance spectrophotometry (UV-Vis DRS) with a Lambda 365 UV/Vis spectrophotometer from PerkinElmer, USA. The analysis provided information on absorbance and bandgap energy in order to understand the material's photocatalytic potential in Photocatalysis processes. The Field Emission Scanning Electron Microscope (FESEM, JSM 7600F, JEOL Ltd., Tokyo, Japan) was used to investigate the surface morphology, lattice structure, particle size, and distribution in order to present a full view of structural integrity and homogeneity within the $CuWO_4$@TiO_2 Photocatalysts. A Brunauer–Emmett–Teller (BET) technique was recorded on the nitrogen adsorption–desorption at 76 K using a Micromeritics 3 Flex version 5.00 (Micromeritics, Norcross, GA, USA). X-ray diffraction (XRD, EMPREAL, Netherlands) was used to investigate the crystalline structure and phase composition of synthesized nanomaterials to confirm their phase purity. The electrochemical impedance spectroscopy (EIS) and cyclic voltammetry (CV) measurements were performed on a Potentiostat/Impedance Analyzer (Metrohm, μStat-i 400s, Switzerland). The EIS was conducted to determine the charge transfer resistance and the conductivity of nanomaterials, indicating their electrochemical performance and efficiency for ROS generation. CV was performed to investigate the redox behavior and electrochemical stability of nanomaterials with the objective of probing deeply into the catalytic activity in Photocatalysis reactions.

3.4.1 Electrochemical Characterizations

3.4.1.1 Preparation of Modified Working Electrode

Before modifying the electrodes, the glassy carbon electrode (GCE) was polished with an alumina slurry. Subsequently, the GCE was sonicated in ethanol, rinsed with DI water, and dried at room temperature. Following this, 1 mg of $CuWO_4$@TiO_2 nanocomposites was dispersed in 2 mL of 0.5% chitosan and sonicated in a bath sonicator for 20 minutes to achieve a homogeneous dispersion. Approximately 10 μL of the homogeneously dispersed composite suspension was carefully applied to the pre-cleaned GCE surface and then dried in a hot air oven at 50 ºC. The working electrodes were stored at room temperature for the subsequent electrochemical detection experiments.

3.4.1.2 Measurement of EIS and CV

The electrochemical characteristics of three different nanomaterials were assessed using electrochemical impedance spectroscopy (EIS) and cyclic voltammetry (CV). EIS is a valuable methodology in electrochemistry that provides insight into the conductivity of electrode surfaces during either oxidation or reduction reactions. This technique also yields information about an electrode's alteration in conductance or impedance after its modification. In this regard, EIS was conducted using three different modified electrodes: $CuWO_4$/CHI-modified GCE (GCE/CHI/$CuWO_4$), TiO_2/CHI-modified GCE (GCE/CHI/TiO_2), $CuWO_4$@TiO_2/CHI-modified GCE (GCE/CHI/$CuWO_4$@TiO_2). The GCE was first polished using an alumina slurry before any electrode modifications. Following this, the GCE was sonicated in ethanol, rinsed with DI water, and left to dry at room temperature. Next, 1 mg of $CuWO_4$@TiO_2 nanocomposites was dispersed in 2 mL of 0.5% chitosan and sonicated in a bath sonicator for 20 minutes to ensure uniform dispersion. Approximately 10 μL of the resulting composite suspension was then carefully applied to the pre-cleaned

GCE surface and dried in a hot air oven at 50 ºC. The measurements were made in the frequency range from 2.5 × 10^3 Hz to 5 × 10^5 Hz, using a modulation amplitude of 40 mV in applied electrode potential. The Nyquist plots of bare and modified electrodes were recorded in the solution of 5.0 mM $[Fe(CN)_6]^{3-/4-}$ and 0.1 M KCl. In this plot, two-time constants may be well distinguished: a semicircular portion at high frequency due to electron transport processes and a linear portion at low frequency due to mass transport processes.

CV is a very powerful technique in the analysis of electro-active species and especially in the studies of the redox reactions of the analytes. In this study, the preliminary electroactive properties of the bare and modified GCE electrodes were characterized in the potential range from - 0.2 to - 0.7 V with a scan rate of 50 mV/s. This was conducted in a solution comprising 5.0 mM potassium ferrocyanide $[K_4Fe(CN)_6]$ with 0.1M KCl.

3.5 Density functional theory

3.5.1 Theoritical Experiment

Three simulated models of $CuWO_4$, Ti/Cu@$CuWO_4$, and Ti/W@$CuWO_4$ were developed for DMol3 computations to examine the electrical as well as optical features of the $CuWO_4$ shell surface and the interface layer of $CuWO_4$@TiO_2. The optimized geometries and electronic properties were investigated to comprehend the impact of Ti and W dopants on the structural and electronic characteristics of $CuWO_4$ surfaces, especially regarding their interaction with TiO_2 at the interface. Calculations utilizing density functional theory (DFT) were conducted with the DMol3 module. The Perdew-Burke-Ernzerhof (PBE) exchange-correlation functional utilizing the generalized gradient approximation (GGA) had been employed for all calculations. A double-numeric polarized (DNP) basis set was employed with a global cutoff of 4.5 Å, and the electronic structures were computed using spin-restricted computations with a medium integration grid. Geometry optimization was performed using convergence conditions of 2 × 10^{-5}

Ha for energy, 4×10^{-3} Å for gradient, and 5×10^{-3} Å for displacement. A Monkhorst-Pack k-point mesh of 2 × 2 × 2 was employed for Brillouin zone sampling, with symmetry enabled throughout the optimization process.

3.6 Photocatalytic Dye Degradation: A ML and Metaheuristic Approach

3.6.1 Data Collection and Analysis

The data were collected from the photocatalytic dye degradation experiments, and 189 data sets were selected for this study. In such processes, four dominant input variables were carefully selected considering their huge impact: the initial concentration of MB (mg/L), the catalyst dose (mg/L), the light intensity (mW/cm^2), and the treatment time (minutes). These variables have been identified as significant factors that might influence the efficiency of degradation of MB dye. The feature importance analysis performed in an elaborative manner also strengthened our understanding that these variables are highly influential on MB removal efficiency. Incorporating these variables, the studied model completely encompasses all the important elements that might be influential in the process of MB dye degradation. The whole approach encompasses data preprocessing; the splitting of data into sets; training ensemble machine learning models such as AdaBoost, Bagging, CatBoost, Decision Tree, Extra Trees, Gradient Boosting, HistGradientBoosting, LightGBM, Random Forest and XGBoost; hyper-parameter tuning using Bayesian optimization; the model performance evaluation metrics; feature importance analysis; parameters optimization with Differential Evolution; estimation of MB dye degradation or removal efficiency. The relationship between the model's input-output parameters and workflow is detailed in Figure 3.1. Various statistical metrics, such as the Coefficient of determination (R^2), Mean Square Error (MSE), Root Mean Square Error (RMSE), Mean Absolute Error (MAE) and Median Absolute Error (MedAE) were used to evaluate the model's predictive performance and details of their calculation based on previously published articles [42, 43].

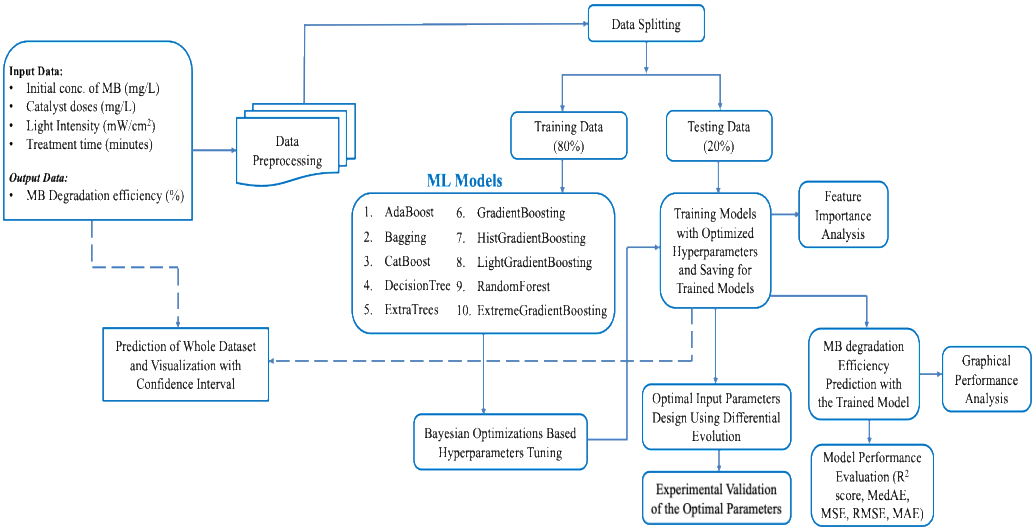

Figure 3.1 Complete block diagram of the proposed approach

3.6.2 Performance evaluation metrics

The model's input-output relationship and workflow are detailed in Figure 3.1. Additionally, to simplify complex computations and mitigate overfitting, the experimental data were randomized using Equation (1) [202]. The model performance evaluation metrics such as the Coefficient of determination (R^2), Mean Square Error (MSE), Root Mean Square Error (RMSE), Mean Absolute Error (MAE) and Median Absolute Error (MedAE) were calculated for each model and as defined by equations 3.1 to 3.6.

$$\text{Normalized Value } (X_{norm}) = \frac{X_i - X_{min}}{X_{max} - X_{min}} \qquad (3.1)$$

Where X_i is any data.

3.6.2.1 Coefficient of determination (R^2)

$$R^2 = 1 - \frac{\sum_{i=1}^{n}(y_i - \hat{y}_i)^2}{\sum_{i=1}^{n}(y_i - \bar{y})^2} \quad (3.2)$$

Where y_i is the actual value, $\hat{y}_i$ is the predicted value, $\bar{y}$ is the mean of actual values, n is the number of observations, R^2 values range from 0 to 1, with higher values indicating better model performance.

3.6.2.2 Mean Square Error (MSE)

$$MSE = \frac{1}{n}\sum_{i=1}^{n}(y_i - \hat{y}_i)^2 \quad (3.3)$$

3.6.2.3 Root Mean Square Error (RMSE)

$$RMSE = \sqrt{\frac{1}{n}\sum_{i=1}^{n}(y_i - \hat{y}_i)^2} \quad (3.4)$$

3.6.2.4 Mean Absolute Error (MAE)

$$MAE = \frac{1}{n}\sum_{i=1}^{n}|y_i - \hat{y}_i| \quad (3.5)$$

3.6.2.5 Median Absolute Error (MedAE)

$$\text{MedAE} = \text{median}(|y_i - \hat{y}_i|) \quad (3.6)$$

3.6.3 Machine Learning Models

Ten tree-based machine learning (ML) models were utilized with default hyperparameters: AdaBoost (AB), Bagging (B), CatBoost (CB), Decision Tree (DT), Extra Trees (ET), Gradient Boosting (GB), HistGradientBoosting (HGB), LightGBM (LB), Random Forest (RF), and extreme Gradient Boosting (XGB), from the library of Scikit-learn (https://scikit-learn.org/stable) in Python [203]. . To evaluate the effectiveness of photocatalyst in MB dye degradation, both preliminary screening and advanced models were developed. The 189 selected datapoint was randomly divided into two subsets: 80% for training and 20% for testing [202]. The generalization capabilities of the models were assessed using the test dataset. The chosen ML algorithms' hyperparameters were optimized using Bayesian optimization, which employs a probabilistic framework to

explore the hyperparameter space and determine optimal values. The optimized models were subsequently trained on the training dataset and tested on the test dataset. The model that presented the best performance matrices in both the training and testing procedures and subsequently used in designing optimal experimental parameters through DE for attaining maximum dye degradation. By offering practical insights for optimizing tentative settings to maximize prediction of dye degradation, this optimization technique increases the practical application of our research.

3.6.4 Descriptions of Ten Machine Learning

3.6.4.1 AdaBoost

AdaBoost is a collective learning model used for regression and classification. It iteratively enhances weak classifiers by learning from their mistakes. AdaBoost uses sequential ensembling instead of the parallel ensembling used in the RandomForest model. Combining numerous weak classifiers can achieve a strong classifier with high accuracy. However, it's important to note that while AdaBoost is an adaptive classifier, it can lead to overfitting. It is sensitive to outliers and noisy data but shows great promise in enhancing the performance of decision trees in binary classification problems. In our analysis, we performed hyperparameter optimization and tuning through grid search to determine the optimal loss function. The primary hyperparameters evaluated included the learning rate (varing from 0.1 to 5) and the total number of boosted trees (n_estimators) from 20 to 500.

3.6.4.2 Bagging

Bootstrap aggregation, also known as Bagging, integrates the concepts of bootstrap and aggregation [204]. The Bagging model generates multiple datasets with slight variations in noise and distribution by randomly sampling from the original training data. Each dataset is used to train a model independently, and the models are then combined into an ensemble model. This approach reduces the risk of models making predictions based solely on specific noise patterns in the original data. Additionally, the out-of-bagging data not included in the bootstrap process can be used to validate individual models during the model aggregation process. This validation helps the Bagging model achieve high generalization performance.

3.6.4.3 CatBoost

CatBoost is a machine learning technique that use gradient-boosted decision trees to predict continuous variables. It is widely recognized for its effectiveness, accuracy, and capability to manage categorical data within the CatBoostRegressor [33]. For the CatBoostRegressor method to function, it is necessary to design a set of relatively weak decision trees initially. Subsequently, these trees are amalgamated to construct a robust model. The method employed to link the trees is gradient boosting. Gradient boosting is the linking method employed in this procedure, which enhances model performance by adding trees one after the other to fix the mistakes of the earlier ones. The mathematical expression used by CatBoost to predict continuous values is presented in Equation (5):

$$y = f(x) = \sum_{i=1}^{n} \alpha i \; hi(x) \qquad (3.7)$$

Here, y represents the predicted value while x denotes the input features. The resultant function (x) is a linear amalgamation of fundamental functions,

$h(x)$. The coefficients αi ascertain the significance of individual base functions within this linear amalgamation.

The model coefficients are calculated using the gradient descent method. In CatBoost, the loss function must be minimised. The loss function quantifies the difference between predicted and observed values. The ML approach CatBoost can effectively address a wide range of regression problems. It is especially effective at addressing issues that pertain to categorical attributes.

3.6.4.4 Decision Tree

Decision trees are models that use a series of logical rules organized into a tree-like structure. Each test typically involves comparing data to a threshold value or specific category. This model makes predictions by segmenting the data into smaller groups using a series of decision rules arranged along a tree structure. Therefore, the order and placement of rules are crucial for the predictive accuracy of decision tree models [205]. Compared to complex artificial intelligence algorithms like artificial neural networks and convolutional neural networks, decision trees have a simple structure and prediction technique. This simplicity allows decision tree models to offer interpretability of predictions. Recently, many studies have focused on enhancing the performance of decision trees by improving their simple structure. As a result, studies have frequently emphasized using a combination of multiple independent decision trees rather than a single decision tree as a model [206].

3.6.4.5 Extra Trees

ExtraTrees, also known as extremely randomized trees, are models that utilize an ensemble algorithm with significant randomness incorporated into the decision tree growth process [207]. The fundamental concept behind ExtraTrees is to introduce strong randomization in the selection of input features and cut points when splitting the nodes of the decision tree. Due to the high level of randomness in this model, the decision tree may not provide an optimal cutting point,

resulting in suboptimal predictive performance as a standalone model. However, when combined with multiple decision tree models, ExtraTrees can effectively explore the data and enhance predictive performance. Furthermore, the model's randomness allows it to utilize all the data in the training process, reducing prediction bias. Additionally, the time required to build the model is reduced since it does not compute the optimal split.

3.6.4.6 Gradient Boosting

Gradient boosting is a widely utilized machine learning model that employs an ensemble method of decision trees known as boosting. The core concept of boosting involves the sequential addition of new decision trees by calculating the residuals of the entire ensemble model. This process continues until the model achieves the highest accuracy. Additionally, these models can be customized by adjusting the structure, such as the loss function and tree addition method [208]. The fundamental algorithm for gradient boosting used in this study can be generalized by the following equation.

$$f(x) = \sum_{k=1}^{K} f^k(x) \qquad (3.8)$$

Where $f(x)$ and $f^k(x)$ indicate entire ensemble model and k-th independent decision tree. N indicates the number of decision trees.

3.6.4.7 HistGradientBoosting

Histogram-based gradient boosting is an advanced method that enhances the speed and performance of gradient boosting models [209]. This technique efficiently combines decision trees on large datasets by dividing input features into a specified number of intervals. As a result, the models can quickly find the optimal split, unlike traditional gradient boosting methods. Additionally, histogram-based gradient boosting can handle missing values by using one of

the partitions for training, eliminating the need to preprocess the input data for missing values before applying the model

3.6.4.8 Light GBM

Light gradient boosting machine (LGBM) is an enhanced version of the Gradient Boosting model. It achieves this by including two techniques that effectively decrease the computational workload [34]. LGBM utilises gradient-based one-side sampling (GOSS) and exclusive feature bundling (EFB) methods. The GOSS methodology is a method that decreases the sample size of a dataset. The fundamental premise of GOSS is that cases with substantial gradients exert a considerable influence on predictions, and the model is inadequately trained for such instances. The GOSS algorithm curates the training data set by selectively including examples that exhibit significant gradients. Hence, cases exhibiting negligible gradients can be disregarded, thereby minimising their contribution to the training process and reducing the dataset's sample count. The EFB is a data analysis technique that aims to reduce the dimensionality of a dataset by minimising the number of input features. The EFB employs a technique of consolidating variables that have a strong correlation into a single category, under the assumption that data with a large number of dimensions is sparsely populated. Reducing the number of samples and features in the dataset using these two approaches significantly reduces the time it takes to compute the model. Furthermore, as stated by Guolin et al., the creators of LGBM, they found a maximum limit to the decrease in performance due to the decrease in sample size and number of features [34]. Therefore, while using the LGBM model, the issue of decreased prediction accuracy should not be overlooked. In addition, the LGBM model utilises a leaf-wise approach during the tree partitioning process. Compared to the level-wise technique, which considers the tree's balance, the leaf-wise tree development in LGBM selects the best possible node to split, reducing prediction error.

The LGBM technique employs a weighted summation to amalgamate predictions from individual trees within the ensemble. During the training iteration, these weights are established through evaluations of the loss function's gradients. The subsequent equation can be employed to predict the target variable using LGBM:

$$\hat{y} = \sum \alpha i \; h(x) \tag{3.9}$$

Where, $\hat{y}$ forecasts the goal value, the weight assigned to the i^{th} tree is denoted by αi, and the forecast i^{th} tree for the input attributes x is represented by $h(x)$.

The LGBM can handle massive datasets, and it excels at capturing intricate non-linear connections between features and the target variable. Through gradient-based optimization, it constructs a set of trees that collectively yield accurate predictions, thus enhancing the performance of the loss function.

3.6.4.9 Random Forest

Random Forest is a model that utilizes the bagging technique among ensembles of independent decision trees [210]. In the bagging approach for regression, multiple decision trees are created by randomly sampling data from the original dataset. The final prediction is then generated by averaging the predictions of the individual trees. Random forests offer performance benefits by reducing variance while maintaining the bias of the models, which is a key advantage of the bagging model. Additionally, random forests randomly select input features for each decision tree from the pool of all input features. This variance in the input variables used in individual decision trees reduces the correlation between the trees. An analysis has shown that ensemble models consisting of low-correlation trees reduce generalization errors and improve prediction performance [210].

3.6.4.10 Extreme Gradient Boosting

XGBoost, short for Extreme Gradient Boosting, is an advanced gradient boosting algorithm that assigns weights to the learning errors of weak models and sequentially incorporates them into the next model to create a prediction model[211]. XGBoost models support parallel processing, resulting in faster computing speed compared to traditional gradient boosting models. Additionally, XGBoost models utilize a technique to prevent overfitting by training the tree using a regularized loss function, defined by the following mathematical equation.

$$L^t = \sum_{i=1}^{n} l\left(y_i, \hat{y_i}^{t-1} + f_t(x_i)\right) + \Omega(f_t) \qquad (3.10)$$

$$\Omega(f_t) = \gamma T + \frac{1}{2}\lambda \|w\|^2 \qquad (3.11)$$

Where L^t and $f^t(x)$ indicate the loss function and decision tree at the t-th iteration. The l is convex loss function. The y_i, $\hat{y_i}$ and x_i indicate true value, predicted value and input data at i-th data instance. The Ω is regulation term calculated with the number of leaves (T) in the decision tree and the Euclidean distance of each leaf ($\|w\|^2$).

3.7 Degradation of Methylene Blue by Photocatalyst Process

For evaluating the catalytic activity of Cupper Tungstate coated titanium dioxide degradation of Methylene blue dye was examined under different conditions.

3.7.1 Preparation of Methylene Blue Solution

An aqueous solution of Methylene blue was prepared in Duran bottle by adding 10mg of Methylene blue in 1000 ml De-ionized water and used it as stock solution, concentration of stock solution was 10mg/L and it further diluted to various concentrations by adding de-ionized water.

3.7.2 Batch Experiment of Degradation of Methylene Blue

In this research, Methylene blue (MB) dye was used as a model contaminant. The model dye was prepared according to the standard operating procedure, and the concentration of MB was 10 mg /L. The dye degradation experiments were conducted in a 150-mL beaker containing 50 mL of MB. A fixed amount (200 mg/L) of $CuWO_4$@TiO_2 Photocatalyst was mixed with the 10 mg/L of MB solution. The reaction mixture was continuously stirred at 250 rpm using a magnetic stirrer for 15 minutes under dark conditions to achieve adsorption and desorption equilibrium. After that, in the photocatalysis process, the visible light source was turned on after the dark condition. The PLS-SXE300E/UV (Beijing Perfect Light Technology Co. Ltd. China) was used as a visible light source over the reactor and used a 300W xenon (Xe) lamp with a range of 320–780 nm VISREF filter. The average light intensity was 126.75 mW/$cm^{2,}$ and the surface of the reaction media was kept at 16 cm from the bulb. Aliquots of 3 mL sample were collected from the reaction mixture at chosen time intervals: -15, 0, 15, 30, 45, 60 and 75 minutes. The samples were filtered using 0.22 μm PTFE syringe filter to eliminate the $CuWO_4$@TiO_2 photocatalyst. The concentration of Methylene blue was determined using a UV-Vis spectrophotometer (T80+, UK) at its characteristic wavelength (275 nm). The degradation efficiency was calculated according to the following Eq (1) [42, 43].

$$\text{Degradation efficiency} = \frac{C_0 - C}{C_0} \times 100\% \qquad (3.12)$$

Where, C_0= initial concentration of MB, C = final concentration of MB.

3.7.3 Catalytic Activity Experiment for Optimization

To evaluate the catalytic efficiency of $CuWO_4@TiO_2$ nanoparticles, different concentrations of methylene blue (5 mg/L, 10 mg/L, and 15 mg/L) were used for the degradation efficiency test. Various catalyst doses (100 mg/L, 250 mg/L, and 400 mg/L) were added to the methylene blue solution and magnetically stirred for 15 minutes under dark conditions to establish adsorption equilibrium. The photocatalytic degradation was then carried out under different light intensities (93.74, 126.75, and 159.38 mW/cm²) with visible light irradiation. At different time intervals, 3 mL of the solution was withdrawn every 15 minutes and filtered using a 0.22 μm syringe filter. The degradation of methylene blue was monitored using a UV-visible spectrophotometer by measuring absorbance at 664 nm, with deionized water used as a blank sample, from the beginning of the reaction until equilibrium was reached after 90 minutes.

3.8 Reactive Species Analysis

Five scavengers, including sodium azide (SA), isopropanol (IPA), triethanolamine (TEA), superoxide dismutase (SOD), and potassium dichromate ($K_2Cr_2O_7$) were further used to identify reactive species such as $^1O_2$, $HO^\bullet$, h^+ $O_2^{\bullet-}$, and e^- during photo Fenton process, respectively. 1mM of TEA, IPA, and SA were used to reduce the catalytic effect and elavate the scavenging effect. Low concentrations such as 0.025 mM of $K_2Cr_2O_7$ and 6 U/mL of SOD were used in this study [46]. The influence of scavengers was determined by measuring the absorbance of Methylene blue after different time intervals.

3.9 Reusability Test

For reusability test, optimum amount (200 mg/L) of CuWO4@TiO_2 photocatalyst was mixed with the 10 mg/L of MB solution. The reaction mixture was continuously stirred at 250 rpm using a magnetic stirrer for 15 minutes under dark conditions to achieve adsorption and desorption equilibrium. Aliquots of 3 mL sample were collected from the reaction mixture at 75 minutes, and were immediately quenched with a small quantity of sodium thiosulfate to stop the reaction. The samples were filtered using 0.22 μm PTFE syringe filter to eliminate the $CuWO_4$@TiO_2 photocatalyst. The concentration of methylene blue was determined using a UV-Vis spectrophotometer (T80+, UK) at its characteristic wavelength (665 nm). Then the catalyst recovers by centrifuge the remaining solution. The remaining catalyst dried at 70 ºC. Then reuse this catalyst to run another catalytic experiment as previously described procedure.

Chapter 4: RESULTS AND DISCUSSION

4.1 Characterization of $CuWO_4$@TiO_2 nanocomposite

4.1.1 UV-Vis Diffuse Reflectance Spectroscopy Analysis (DRS)

UV-Vis diffuse reflectance spectroscopy (DRS) is a crucial technique for measuring the optical properties of semiconductor materials. This technique is particularly beneficial for evaluating the band gap energy of materials, providing essential insights into their photocatalytic performance. The capacity of a material to absorb visible light and produce electron - hole pairs is essential in photocalysis. Reducing the band gap width of a semiconductor material allows it to absorb a broader range of light wavelengths within the visible spectrum. This enhanced light absorption potential can improve the efficiency of photocatalytic processes, leading to a more effective conversion of light energy into chemical energy [212]. The band gap energy (Eg) of $CuWO_4$@TiO_2 may be determined from the DRS data applying Tauc plots. When optical band gaps were measured using Tauc's relation, where one can determine the band gap (Eg) value while taking into account the direct band gap [213]. The UV- Vis DRS of $CuWO_4$, TiO_2, and $CuWO_4$@TiO_2 is shown in Figure 4.1. The absorption edge of pristine TiO_2 was observed at 385 nm, indicating that it can only absorb light in the UV region [214]. The whole visible spectrum is absorbed by pure $CuWO_4$, according to its optical absorption spectra. $CuWO_4$, active in the visible spectrum, can capture more light due to its visible light-trapping characteristics. This leads to the excitation and transfer of electrons to the formation of TiO_2. As reported earlier, an increase in TiO_2 absorbance was observed when a visible, responsive partner was added [215, 216]. Compared to $CuWO_4$, the absorption edge of $CuWO_4$@TiO_2 is slightly shifted towards the visible region. This change is a result of the electronic interaction between $CuWO_4$ and TiO_2. The energy band gap value of $CuWO_4$@TiO_2 (2.7 eV) is found to be smaller than that of TiO_2 (3.15 eV) . The observed slight variation in the band gap does not signify a reduction in the

band gap of $CuWO_4$@TiO_2 when applied to the surface. As more interacting atoms are incorporated, the composite material manifests new energy states, leading to a closer alignment of the energy bands [217]. Thus, by reducing the band gap and making TiO_2 suitable for absorbing visible light, the combination of $CuWO_4$ and TiO_2 significantly affects the optical properties. $CuWO_4$@TiO_2 heterojunction samples have a low bandgap, which indicates promising photocatalytic application possibilities.

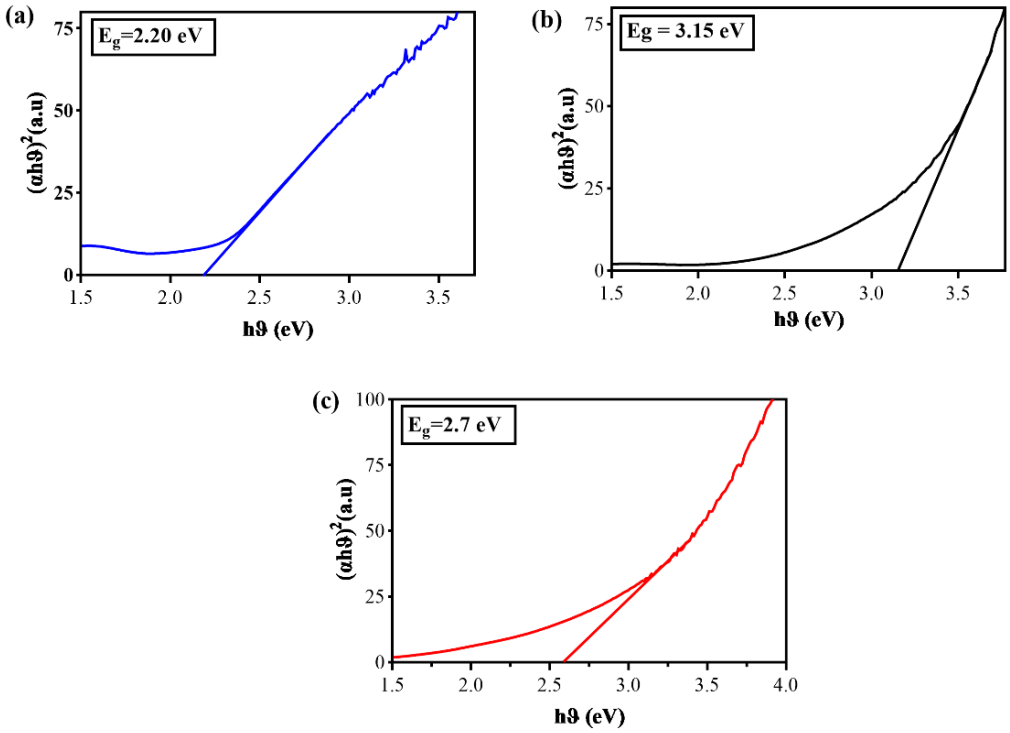

Figure 4.1 Tauc plot of the band gap of (a) $CuWO_4$, (b) TiO_2, and (c)$CuWO_4$@TiO_2

4.1.2 Field Emission Scanning Electron Microscopy (FESEM)

High-resolution imaging by FESEM enables detailed observation of nanomaterials' shape and size distribution, which is crucial for understanding their photocatalytic performance in the process. These images represent the comparison between $CuWO_4$ nanoparticles and $CuWO_4$@TiO_2 nanoparticles in Figure 4.2. In general, the $CuWO_4$ particles are finer, and their outlines are sharp, showing typical characteristics of uncoated nanoparticles. They have a porous and rough surface.

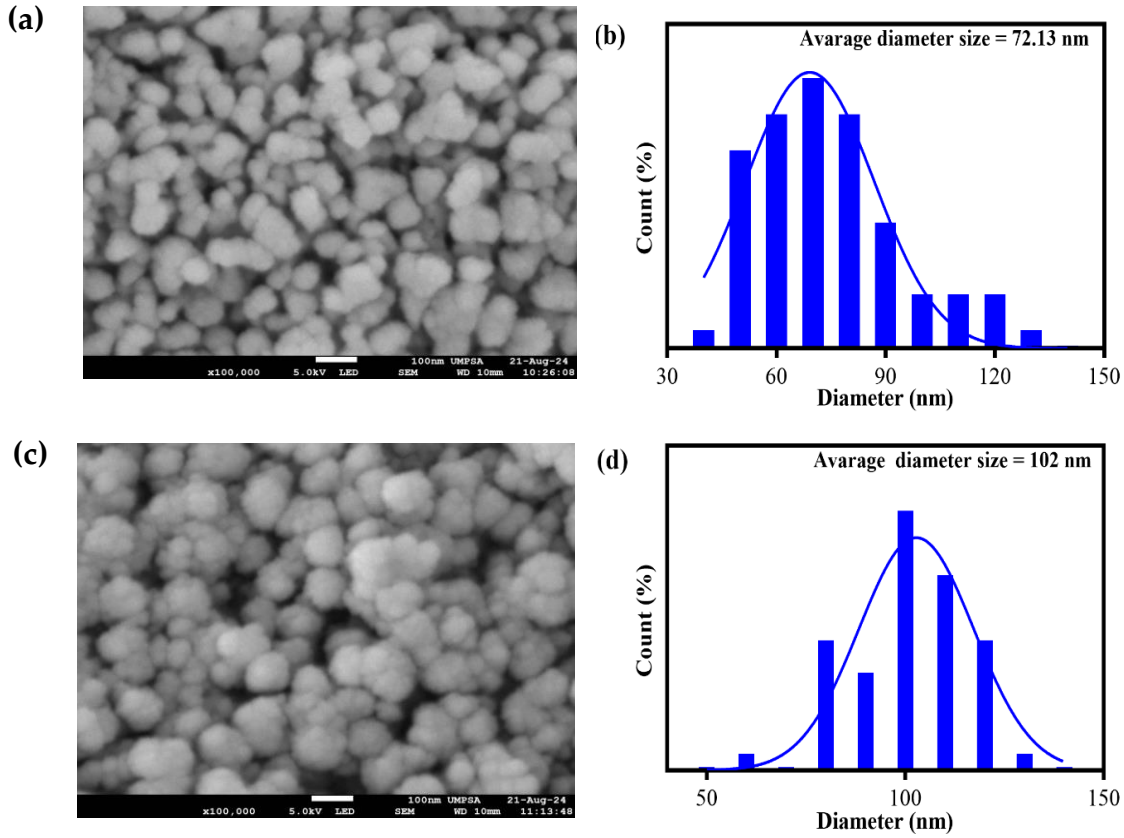

Figure 4.2 FESEM images (a) $CuWO_4$ and (b) $CuWO_4$@TiO_2

After being coated with TiO_2, $CuWO_4$@TiO_2 particles expand and clump together, creating a smooth surface. This suggests that a complete layer of TiO_2 has formed around the $CuWO_4$ core. This modification results in an improvement in the stability and photocatalytic performance of the material. In Fig. (a), the surface image depicts the morphology of $CuWO_4$ nanoparticles, showing spherical and closely packed particles with slight aggregation. The corresponding histogram indicates an average particle size of 72.13 nm, with most particles falling in the 55–85 nm range. The surface is visibly rough and irregular, containing fine granules with micro-porous features. These characteristics are beneficial for active site exposure in photocatalytic and adsorption applications. The nanoscale size suggests homogeneous nucleation with limited directional growth, leading to isotropic morphology. After TiO_2 coating, the morphology changes, as

visualized in Fig. (b). The particles still exhibit a spherical shape but appear slightly larger and more distinct, confirming the formation of a core–shell structure ($CuWO_4$@TiO_2). The histogram shows an average particle diameter of 102 nm, indicating an increase in size due to the deposition of the TiO_2 shell layer. The distribution is relatively narrower, suggesting controlled shell growth over the $CuWO_4$ core.This increase in particle size from 72.13 nm ($CuWO_4$) to 102 nm ($CuWO_4$@TiO_2) provides evidence of successful heterojunction formation between $CuWO_4$ and TiO_2, which is crucial for enhanced charge carrier separation in photocatalytic processes. The rougher texture and enhanced particle dispersion observed in the TiO_2-coated sample suggest improved surface area and light scattering, which are advantageous for catalytic efficiency.These morphological observations are in agreement with crystallite size trends observed in XRD and confirm the successful synthesis of $CuWO_4$@TiO_2 heterostructures. The core–shell morphology with increased surface roughness and particle size supports its potential use in photocatalytic and environmental applications.

4.1.3 X-ray Diffraction Analysis

The X-ray diffraction (XRD) of $CuWO_4$ nanomaterials with different shapes shows variations in crystallinity, phase purity, and structural organization. The XRD pattern of $CuWO_4$ nanoparticles indicates small crystallite sizes and lattice strain, typical of nanoscale materials. The X-ray diffraction (XRD) patterns of pure TiO_2, pure $CuWO_4$, and the $CuWO_4$@TiO_2 composites are presented in (Figure. 4.3). The XRD analysis was conducted to confirm the phase composition, crystallinity, and structural integrity of the synthesized materials, which are crucial for understanding their photocatalytic performance. High crystallinity is essential for effective charge separation and transport in photocatalytic materials, as it reduces the number of defects that can act as recombination centers for photogenerated charge carriers [218]. High crystalline material with strong peaks is formed, as indicated by the $CuWO_4$ pattern. Every peaks is in good alignment with JCPDS card No - 80-1918[219]. Triclinic $CuWO_4$ displayed distinct peak shapes at 2θ values of 15.31°, 19.05°, 23.57°, 24.14°, 25.90°, 28.76°, 30.17°, 31.67°, 32.12°, 35.70°, 36.87°, 38.60°, 39.90°, 41.12°, 42.91°, 44.89°, 47.10°, 48.82°, 49.89°, 51.68°, 53.42°, 55.62°, 59.58°, 62.74°, 63.91°, 66.66°, 73.45°and 74.80° which corresponds to (010), (100), (0-11), (011), (-101), (-1-11), (111), (-111), (1-11), (120), (0-21), (002), (200), (210), (-102), (-121), (112), (030), (130), (-2-21), (221), (-220), (202), (300), (222), (311), (023), (330) and (-3-22) planes respectively [214, 220]. The peaks obtained at 2θ values 25.3°, 38.19°, 48.27°, 53.90°, 55.17°, 62.82°, 70.56°, 75.60° correspond to (101), (004), (200), (105), (211), (204), (220), and (215) crystal planes indicating the formation of anatase phase TiO_2. The observed results agree with JCPDS Card No 21-1272 [218, 221, 222]. The absence of peaks indicating other phases shows the high purity of the synthesized TiO_2. No diffraction peaks from impurities were detected, indicating sample purity [223]. The high intensity and distinct character of the pure TiO_2 and $CuWO_4$ peaks indicate their pure crystalline composition. It is possible to obtain pure $CuWO_4$ through chemical

and calcination processes, as other phases, including impurities or metallic Cu, are absent [224]. The XRD graph shows that the crystalline patterns of $CuWO_4$ and TiO_2 were identified in the $CuWO_4$@TiO_2 combination. The XRD pattern of the composite reveals a decrease in the intensity of the TiO_2 peak due to the improved crystallinity of $CuWO_4$. These results indicate the successful formation of well-defined $CuWO_4$@TiO_2 composites. The average crystallite size of pure oxides and composite materials was also determined using the Debye-Scherer Formula [225]. The average crystallite sizes of $CuWO_4$, and $CuWO_4$@TiO_2 were found to be 72.13 nm, and 102 nm, respectively. The average crystallite size of the composite nanostructure was observed to be more extensive compared to pure oxides. This increase in crystallite size could lead to a reduced band gap and improved visible light absorption. As a result, this may lead to the generation of reactive oxygen species and an increase in degradation [226].

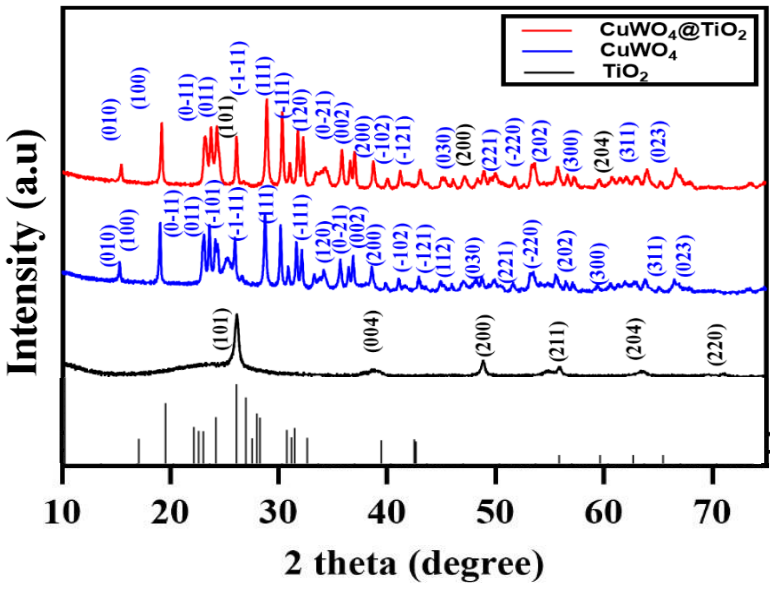

Figure 4.3 XRD analysis of $CuWO_4$, TiO_2 and $CuWO_4$@TiO_2.

4.1.4 X-ray Photoelectron Spectroscopy (XPS)

X-ray photoelectron spectroscopy (XPS) was used to characterize the surface composition and chemical valence states of various elements comparing $CuWO_4$@TiO_2. The XPS survey profile confirmed the presence of Cu, W, O, and Ti in the structure of $CuWO_4$@TiO_2 Figure 4.4(a). The high-resolution Cu 2p, W, O_{1s}, and Ti_{2p} XPS profiles of these nanocomposites are depicted in Figure 4.4(b), (c), (d) and (e), respectively. The copper spectra displayed two significant peaks, one at 933 eV and another at 952.82 eV, in Figure 4.4(b) corresponding to the doublets of $2P_{3/2}$ and $2P_{1/2}$, respectively, and indicate the normal state of Cu^{2+} in the prepared sample[219]. The tungsten XPS spectra exhibit a significant peak at 36 eV ($4f_{7/2}$) and a less intense peak at 37.82 eV ($4f_{5/2}$), in Figure 4.4(c), both these peaks confirm the presence of tungsten in the W^{6+} oxidation state [227]. The high-resolution XPS spectra of O_{1s} Figure 4.4(d) is the further deconvoluted into two peaks. The peak positions at 530.52eV and 531.18eV relate to oxygen coupled with metal ions (Cu-O and W-O)[228]. The O_{1s} spectra of $CuWO_4$ have two peaks: one for the W-O bond, which has a lower binding energy 531.18 eV; the other for the Cu-O bond, which has a binding energy of 530.52eV. Figure 4.4(d) displayed that the XPS patterns for antase TiO_2. The binding energies of about 458.70 and 464.40 eV corresponded to Ti $2p_{3/2}$ and Ti $2p_{1/2}$, respectively Figure 4.4(e). the oxidation state of Ti^{4+} and well fitted with this two peaks are reported [229]. The Ti 2p2/3 and Ti 2p1/2 binding energies differ by 5.7 e.V, indicating that Ti is mainly Ti^{4+} [230]. Through its intensity ratios, a Ti structure free of impurities as well as surface imperfections is created. It was seen that the Ti-O interaction formed at 533.58 eV in the O_{1s} spectrum. These results confirmed the heterojunction was constructed accurately.

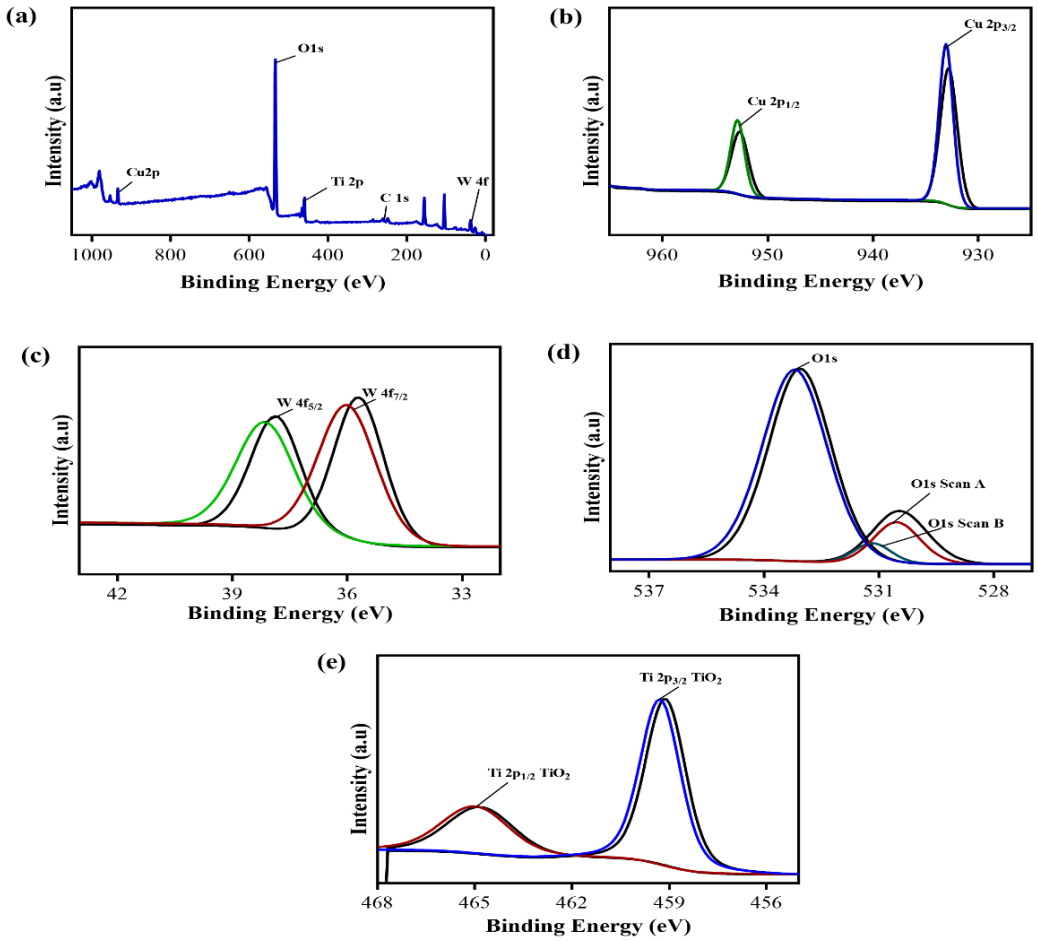

Figure 4.4 XPS Spectra of (a) $CuWO_4$@TiO_2, (b) Cu_{2p} (c) W_{4f} (d) O_{1s} (e) Ti_{2p}

4.1.5 Brunauer-Emmett-Teller (BET) Analysis

To determine the surface area, pore size and pore volume of the $CuWO_4$@TiO_2 photocatalyst the Brunauer-Emmett-Teller (BET) model was employed, using N_2 adsorption-desorption. Figure 4.5 shows the N_2 adsorption/desorption isotherm for the $CuWO_4$ and $CuWO_4$@TiO_2. The BET analysis, summarized in Table 4.1, provides a comprehensive understanding of the surface area and pore characteristics of the TiO_2-coated $CuWO_4$ and $CuWO_4$ materials. The surface area of the $CuWO_4$@TiO_2 composite was 174.0 m^2/g whereas the specific surface area of $CuWO_4$ was only 15.5m^2/g. Core-shell structure of $CuWO_4$@TiO_2 demonstrates significantly greater BET surface area and pore volume than the core $CuWO_4$, allowing for the provision of more active sites and the production of more ROS

[231]. The pore volumes are 0.041548 cm^3/g and 0.258393 cm^3/g, respectively. Furthermore, the Barrett–Joyner–Halenda (BJH) curves obtained from the adsorption branch of isotherms decisively exhibit contrasting pore properties for the two materials. The $CuWO_4$ material at the core (inset of Figure. 4.5(a)) has a considerable pore width of approximately 80.6 nm. The highest pore volume, measured at a rate of change of pore width (dV/dlog(w)), is around 0.0871 cm^3/g. Smaller pores have a minimal impact, indicating a blend of mesoporous and macroporous structures[232].

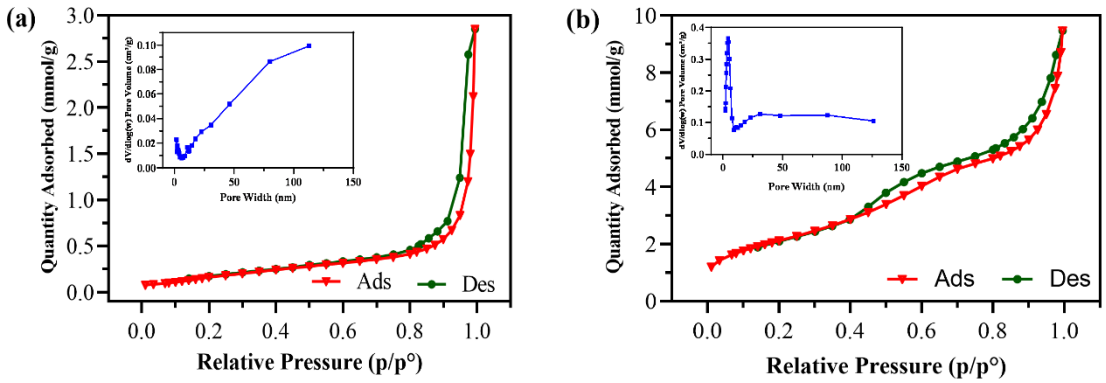

Figure 4.5 N_2 adsorption and desorption isotherms and BJH pore size distribution curves (insets) for (a) $CuWO_4$ and (b) core-shell $CuWO_4$@TiO_2

On the other hand, the $CuWO_4$@TiO_2 material with a core-shell structure (insetof Figure. 4.5(b)) displays a narrower range of pore widths, specifically between3 and 5 nm. Meanwhile, the maximum pore volume (dV/dlog(w)) is substantially greater at around 0.37100 cm^3/g. The distribution of this substance highlights a mostly mesoporous structure, which provides a significant surface area suitable for adsorption. Higher active sites may be produced by the larger specific surface area, perhaps leading to improved photocatalytic activity [233].

Table 4.1. Physicochemical properties of $CuWO_4$ and $CuWO_4@TiO_2$

Characteristics	**Value/Unit**	
	$CuWO_4$	**$CuWO_4@TiO_2$**
BET Surface Area	15.5 m^2/g	174.0 m^2/g
Langmuir Surface Area	25.0 m^2/g	244.5483 m^2/g
Total pore volume	0.04 cm^3/g	0.25 cm^3/g
Pore diameter (BET)	10.7 nm	5.9 nm
BJH pore width	80.6 nm	3-5 nm
BJH pore Volume	0.087 cm^3/g	0.371 cm^3/g

4.1.6 Electrochemical Impedance Spectroscopy (EIS)

The Electrochemical impedance spectroscopy (EIS) spectra is a valuable technique for investigating interfacial charge transfer in a semiconductor materials [234]. Additionally, it offers information on how conductible electrode surfaces are during reduction or oxidation processes. This method also provides details on how an electrodes conductance or impedance changes following modification [235]. A nyquist plot, in which the real component (Z′) and the imaginary component (Z″) of the impedance are displayed on the x-and y- axes, respectively, is commonly used to depict electrochemical impedance spectra [236, 237]. The Nyquist plots of the bare and modified electrodes are shown in the Figure 4.6(a). Randles's equivalent circuit (Figure 4.7) may be used to illustrate it. It is made up of the Warburg impedance (W), charge transfer resistance (R_{ct}), solution resistance (R_s), and double- layer capacitance (Cdl). Table 4.2 lists the values that correspond to these components. As shown in Figure 4.6(a), the Nyquist plots of altered electrodes reveal that the R_{ct} value of $CuWO_4@TiO_2$. $CuWO_4@TiO_2$/GCE nyquist plot (Rct) obtained at 61.6 Ω is used to analyse the EIS parameters from NOVA software. Conversely, bare/GCE, CHI/GCE, and

$CuWO_4$/GCE, had measured Rct values of 81.6 Ω, 72.2 Ω, and 66.9 Ω, correspondingly. Higher electron transfer rates are often indicated by smaller semicircle diameters, whereas slower electron transfer rates are suggested by larger diameters[238]. According to Figure 4.6(a), the modified electrode displays a smaller semicircle, confirming a lower electron transfer resistance, while the bare GCE displays a larger semicircle than other modified GCEs, confirming a higher electron transfer resistance[239].

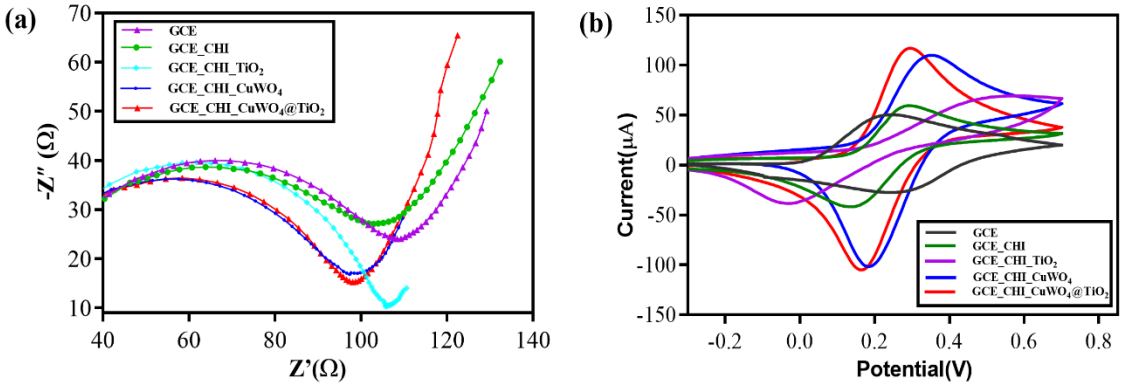

Figure 4.6 Electrochemical analysis of of (a) bare and modified GCE (Inset-Randles equivalent circuit model) and cyclic voltammograms of (b) bare and modified GCE. The measurements were recorded in a 5 mM $K_4Fe(CN)_6$ and 0.1 M KCl at 50 mV/sec scan rate.

Additionally, compared to modified GCE, the $CuWO_4$@TiO_2 modified GCE displays a smaller semicircle, suggesting that $CuWO_4$ could decrease the electron-transfer resistance at the electrode surface.Consequently, the low Rct values of $CuWO_4$@TiO_2/GCE show that it significantly enhances the conductivity and quicker electron transfer rate on the GCE surface[240] . From the Table 4.2, the rise in Cdl in modified indicates an augmented effective surface area, enabling enhanced charge storage at the electrode/electrolyte interface. The Warburg impedance (W) is decreased, indicating improved ion diffusion properties. Rct, Cdl, and *W* improvements collectively show how effective surface modification is at improving the electrode's electrical conductivity and overall performance.

Thus, we can derive the electron transfer behaviour of the modified electrode system and prove that $CuWO_4$ nanocomposites can be used for various photocatalytic applications [241].

Table 4.2. Randles equivalent circuit for both bare and modified electrodes

Electrode	**R_s (Ω)**	**R_{ct} (Ω)**	**C_{dl}(F)**	**W($\Omega s^{-1/2}$)**
GCE	19.7	81.6	7.8×10^{-7}	0.000170
CHI/GCE	20.7	72.2	8.81×10^{-7}	0.000125
$CuWO_4$/GCE	23.6	66.9	1.43×10^{-8}	0.000740
$CuWO_4$@TiO_2/CHI/GCE	27.1	61.6	2.58×10^{-6}	0.000258

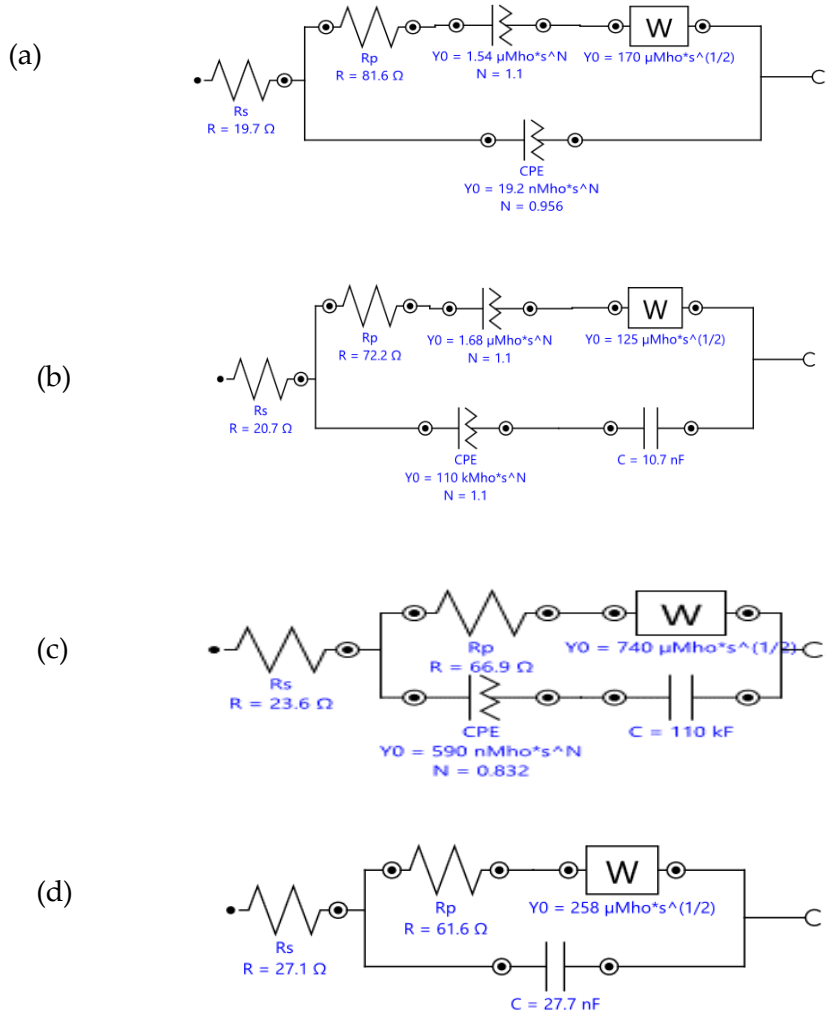

Figure 4.7 Randles equivalent circuit model for bare and modified electrodes: (a)GCE , (b)CHI/GCE, (c)$CuWO_4$/ GCE, and (d)$CuWO_4$@TiO_2/CHI/ GCE

4.1.7 Cyclic Voltammetry (CV)

CV is a very effective method for analysing electroactive molecules, particularly for studying analyte redox reactions (Figure 4.6(b)).The shape and position of these peaks provide insights into the electrochemical activity and reversibility of the redox processes. The CV was used to further investigate the electrochemical behaviour of the unmodified GCE, the modified electrodes such as CHI/GCE, $CuWO_4$/GCE, TiO_2 /GCE and $CuWO_4$@TiO_2 /GCE within the redox reaction at a fixed scan rate of 50 mV/s. It was observed that $CuWO_4$@TiO_2 the displayed the highest anodic current at around 120 μA at a potential of 0.2 V, indicating strong

oxidation activity. In comparison, the $CuWO_4$/GCE, TiO_2 /GCE, CHI/GCE, GCE, showed lower peak currents of 110μA, 67μA, 59μA, and 48 μA, respectively, indicating relatively weaker oxidation activity. Similarly, in the cathodic region, the $CuWO_4$@TiO_2 photocatalyst showed the highest peak current of 105 μA, representing high reduction activities, while the $CuWO_4$/GCE, TiO_2 /GCE, CHI/GCE, GCE again gave lower peak currents (97 μA, 37 μA ,42 μA, and 28 μA, respectively) for reduction. This higher redox performance of $CuWO_4$@TiO_2 indicates a higher electrochemical surface area and a higher amount of electrochemically active sites and structural features help to increase the area related to ion exchange particular surface; hence, $Fe(CN)_6^{3-/4-}$ on the electrode surface may act effectively in rapid interaction between ions and electrons.These results emphasized the crucial role of electron transfer properties in determining the overall electrochemical performance of nanomaterials. Results showed that the efficiency of fast electron transfer and better conductivity of the modified electrode revealed a greater current responsiveness of the redox peak current of $CuWO_4$@TiO_2/GCE in comparison with the bare electrode.

4.2 Theoritical Analysis

To understand the electronic structure and photocatalytic performance, we performed periodic DFT calculations [242, 243]. The results from D3mol calculations for the compound $CuWO_4$ and two models, where Ti is doped at 50% in the Cu and W positions (as surface interaction of core TiO_2 and shell $CuWO_4$) to simulate the experimental conditions, and the results were recorded in Table 4.3.

Table 4.3. Computational results of $CuWO_4$ and $CuWO_4@TiO_2$

Energy	$CuWO_4$	Ti/Cu@ $CuWO_4$	Ti/W@ $CuWO_4$
Total Energy (eV)	-937789	-894730	-151807
Fermi Energy (eV)	-6.24	-5.044	-6.912
DFT Energy Gap (eV)	0.539	0.491	0.833
Binding Energy (eV)	-65.922	-80.915	-62.48
Kinetic Energy (eV)	-530.719	-288.518	-388.75
Electrostatic Energy (eV)	422.486	158.818	288.929
Spin Polarization Energy(eV)	18.496	20.108	15.219
Valence Band Edge (eV)	-6.763	-5.255	-7.328
Conduction Band Edge (eV)	-6.224	-4.764	-6.495

The total energy which represents the stability of the compound and possible interface layers indicates that it is the most stable configuration of the interface of Ti/Cu@$CuWO_4$ (Ti is doped in the Cu position) showing almost similar stability to $CuWO_4$. In contrast, Ti/W@ $CuWO_4$ (Ti-doped in the W position) refers to an unstable configuration, as seen by its much higher total energy. Thus, we focus on the two models of $CuWO_4$ and Ti/Cu@$CuWO_4$ for further investigations.

As well known, a higher Fermi energy typically corresponds to a higher potential for conductivity. Thus, Ti/Cu@$CuWO_4$ increases the Fermi energy from -6.37 eV of $CuWO_4$ to -5.044 eV suggesting an enhancement in conductivity and could exhibit better charge transport than $CuWO_4$, further promoting photocatalytic efficiency. In addition, the slight increase in spin polarization energy when Ti/Cu@$CuWO_4$ suggests enhanced magnetic behavior. The structural properties of $CuWO_4$ and Ti-doped $CuWO_4$ (Ti@$CuWO_4$) were analyzed to understand the effects of doping on the crystal geometry. The pure $CuWO_4$ structure exhibits Cu–O bond lengths of 1.967 Å and 2.076 Å, indicative of slight asymmetry in the coordination environment around the Cu centers.

Upon introducing Ti dopants, significant changes in the local structure are observed. When Ti replaces Cu, the Ti–O bond lengths are reduced to 1.947 Å and 2.151 Å, while replacing W results in even shorter Ti–O bond lengths of 1.866 Å and 2.117 Å. These changes highlight the stronger bonding interactions of Ti compared to Cu or W, leading to localized structural distortions and impacting electronic properties. However, Ti/Cu@$CuWO_4$ raises the valence band edge, making it easier for electrons to be excited at the interface. Similarly, Ti/Cu@$CuWO_4$ increases the conduction band edge significantly, which may make electron conduction easier. As expected, the interface of Ti/Cu@$CuWO_4$ slightly decreases the band gap within the visible light range and boosts charge separation by introducing new states into the conduction and valence bands, reducing recombination rates as shown in the band structure and PDOS of $CuWO_4$ and Ti/Cu@$CuWO_4$ (Figure 4.8).

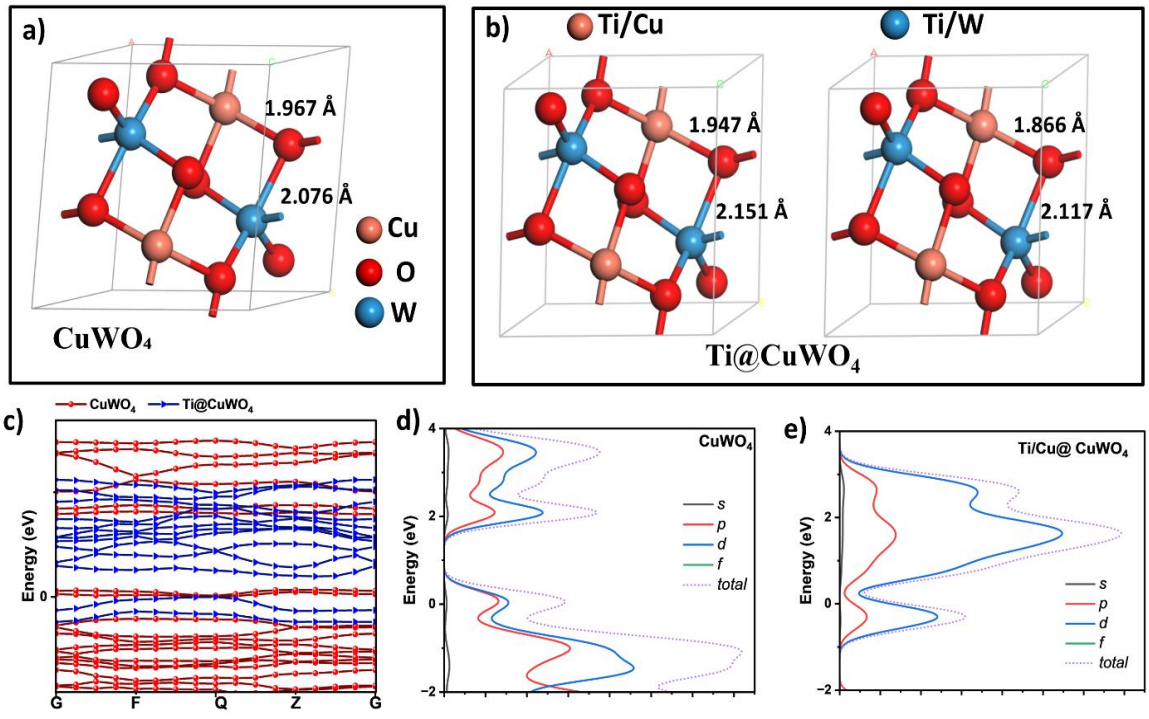

Figure 4.8 Optimized structure of (a) $CuWO_4$, (b)Ti@$CuWO_4$; (c) Band structure; (d) PDOS of $CuWO_4$, and the surface of (e) Ti@$CuWO_4$equivalent circuit model for bare and modified electrodes: (a)GCE, (b)CHI/GCE, (c)$CuWO_4$/ GCE, and (d)$CuWO_4$@TiO_2/CHI/ GCE.

4.3 Descriptive Statistics

The statistical properties of the experimental data points used to examine the degradation of MB dye by a photocatalyst are presented in Table 4.4. The various statistics computed in the analysis by considering four input parameters: concentration of MB (mg/L); catalyst dosage (mg/L); light intensity (mW/cm^2); treatment time (min); and there was only one output parameter reflecting the MB dye degradation, %. The mean values of each variable or parameter denoted its average level with specific values such as a concentration of MB of 10 mg/L, doses of catalyst of 250 mg/L, light intensity of 126.75 mW/cm^2, treatment times of 45 min, and an average MB degradation of 66.71%, as shown in Table 4.4. The standard deviation measured data dispersion around the mean. Minimum and maximum values outline the data's range that can indicate the extent of variability. Percentiles- specifically the 25th, 50th, and 75th - divided the data into quartiles, allowing a view of distribution and identifying potential skewness or outliers. Skewness measured the asymmetry of data distribution, and a value closer to zero indicates greater symmetry in the distribution. Kurtosis provided insight into the shape of the data's distribution, with negative values suggesting a flatter-than-normal distribution. Overall, these statistical measures offered a comprehensive view of the central tendencies, variability, and distributional patterns in the dataset.

Table 4.4. Summarized results of the statistical analysis of the experimental data

Statistics	Concentration of MB (mg/L)	Catalyst dose (mg/L)	Light intensity (mW/cm²)	Treatment time (min)	Degradation of MB (%)
count	189	189	189	189	189
mean	10	250	126.62333	45	66.71
std	4.09	122.79978	26.868743	30.07	31.35
min	5	100	93.74	0	0
25%	5	100	93.74	15	54
50%	10	250	126.75	45	78
75%	15	400	159.38	75	90
max	15	400	159.38	90	100
Skewness	0	0	-0.007090	0	-1.21058
Kurtosis	-1.5	-1.5	-1.50	-1.25	0.196779

In Figure 4.9, the heatmap illustrates the correlation between four input parameters: concentration of MB, catalyst dose, light intensity, and treatment time. The output parameter only measured MB dye degradation efficiency. The analysis revealed a negative correlation (-0.74) between the concentration of MB and the degradation of MB, suggesting that higher concentrations impede the degradation process. The correlations for catalyst dose and light intensity were weaker (-0.22 and -0.15, respectively), implying their negative influence when considered independently, resulting in higher catalyst dose and light intensity reduced the MB degradation rate. Conversely, treatment time showed a significant positive correlation (0.92) with MB degradation efficiency, indicating its critical role in enhancing dye removal. These findings underscore the dominant impact of treatment time on MB dye degradation, with concentration also playing a pivotal role. At the same time, the effects of catalyst dose and light intensity appear less prominent. The dark colors represent the strong correlation

between the inputs and the output variable, while lighter colors indicate a weaker correlation.

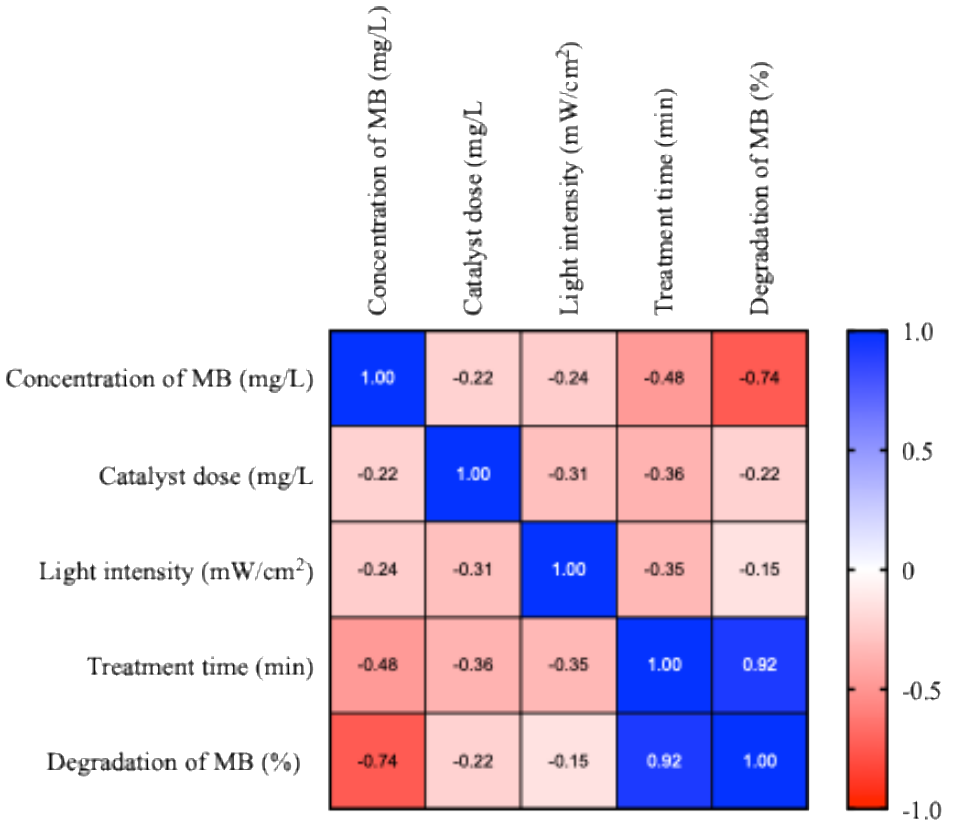

Figure 4.9 Heatmap representation of the experimental datasetRandles

4.4 Model Performance Evaluation

In the current study, we used Bayesian optimization to fine-tune the hyperparameter of ten tested machine learning models with the goal of maximizing the predictive capability. The optimized hyperparameters for the tested model of AdaBoost, Bagging, CatBoost, Decision Tree, Extra Trees, Gradient Boosting, HistGradientBoosting, LightGBM, Random Forest, and XGBoost are shown in Table 4.5. Figure 4.10 provides the scatter plots of these models for the training and test data points. This allowed comparing the experimental and predicted values for each model. Additionally, the plots indicated a strong correlation between experimental and predicted training data, clustering the points near the 45-degree reference line. Each model was trained

and tested using 189 datasets. The hyperparameter setting in machine learning models has a direct and considerable impact on the model's prediction performance (Yang and Shami, 2020). Consequently, optimizing the hyperparameters before the AI model's prediction process is necessary. This study employed the Bayesian optimization (BO) technique to determine the most suitable parameter configuration for 10 machine learning models. The BO technique used the bayes_opt module in the Python computer language (Nogueira, 2014). Furthermore, the BO fine-tuned the hyperparameters across all models, conducting 200 iterations. The optimal hyperparameter values for all 10 models were computed, resulting in the values presented in Table 4.5.

This study utilizes the Bayesian optimization (BO) technique, which treats the objective function as an unknown black box function and aims to identify the optimal solution that maximizes the function value. The utilization of BO techniques necessitates the implementation of two fundamental algorithms to carry out the process of optimization. At first, a surrogate model uses probability to approximate the shape of an objective function that is not known. The acquisition function identifies the most advantageous candidate values for determining the best solution by using a probabilistic estimation of the objective function. The Backtracking Optimisation (BO) repeatedly executes the two fundamental algorithms a specified number of times, consistently identifying potential values that are progressively closer to the accurate solution. Stochastic analysis-based optimization techniques can track the optimal hyperparameters much faster than other automated optimization approaches, including grid search (Victoria and Maragatham, 2021). Table 4.6 outlines the range of hyperparameters and their optimal values, which were determined through Bayesian optimization calculations. After training and fine-tuning the identified ML models, the performance of the corresponding ML models was predicted by

using scatter plots. In these Figures, the black dotted lines refer to the perfect regression line determined by the equation y = x.

Table 4.5. Hyper-parameters' optimal values

Adaboost	Concentration of MB = 0.08818332 Catalyst dose = 0.00717813 Light intensity = 0.04843316 Treatment time = 0.85620540
Bagging	Concentration of MB = 0.1069742 Catalyst dose = 0.01335607 Light intensity = 0.0463456 Treatment time = 0.83332413
CatBoost	Concentration of MB = 0.11675095 Catalyst dose = 0.01765872 Light intensity = 0.05549262 Treatment time = 0.81009770
Decision Tree	Concentration of MB = 0.10496018 Catalyst dose = 0.00859749 Light intensity = 0.05565690 Treatment time = 0.83078543
ExtraTree	Concentration of MB = 0.11053477 Catalyst dose = 0.01261744 Light intensity = 0.04742181 Treatment time = 0.82942598
GradientBoosting	Concentration of MB = 0.11748337 Catalyst dose = 0.01692274

	Light intensity = 0.05443650 Treatment time = 0.81115740
HistGradientBoosting	Concentration of MB = 0.11570924 Catalyst dose = 0.01699747 Light intensity = 0.05559588 Treatment time = 0.81169741
LightBoost	Concentration of MB = 0.11647660 Catalyst dose = 0.01618828 Light intensity = 0.05387521 Treatment time = 0.81345991
Random Forest	Concentration of MB = 0.10700593 Catalyst dose = 0.01344855 Light intensity = 0.04609796 Treatment time = 0.83344756
XGBoost	Concentration of MB = 0.11665398 Catalyst dose = 0.01657912 Light intensity = 0.05383390 Treatment time = 0.81293299

Table 4.6. Hyper-parameters' optimal values

Adaboost	(learning_rate', 0.9878561226091978), ('n_estimators', 200)
Bagging	(max_features', 1.0), ('max_samples', 1.0), ('n_estimators', 126)
CatBoost	(bagging_temperature', 0.0), ('depth', 3), ('iterations', 200), ('l2_leaf_reg', 0.1), ('learning_rate', 0.09457463282239957), ('random_strength', 0.1)
Decision Tree	(ccp_alpha', 1e-06), ('max_depth', 16), ('max_features', 1.0), ('max_leaf_nodes', 100), ('min_samples_leaf', 1), ('min_samples_split', 2), ('min_weight_fraction_leaf', 0.0)
ExtraTree	('max_depth', 15), ('max_features', 0.8814683886261658), ('min_samples_leaf', 1), ('min_samples_split', 2), ('n_estimators', 140)
GradientBoosting	('learning_rate', 0.08474802210335118), ('max_depth', 3), ('max_features', 1.0), ('min_samples_leaf', 1), ('min_samples_split', 20), ('n_estimators', 200), ('subsample', 0.5)
HistGradientBoosting	(l2_regularization', 0.1), ('learning_rate', 0.29999999999999993), ('max_bins', 50), ('max_depth', 3), ('max_iter', 92), ('max_leaf_nodes', 20), ('min_samples_leaf', 10)
LightBoost	('colsample_bytree', 0.8303967118108533), ('learning_rate', 0.29999999999999993), ('max_depth', 3), ('min_child_samples', 3), ('n_estimators', 79), ('num_leaves', 281), ('subsample', 1.0)])
Random forest	max_depth', 9), ('max_features', 0.7576556648677808), ('min_samples_leaf', 1), ('min_samples_split', 2), ('n_estimators', 200)
XGBoost	('colsample_bytree', 0.8259641168870455), ('learning_rate', 0.06981634148413023), ('max_depth', 3), ('min_child_weight', 1), ('n_estimators', 200), ('subsample', 0.5)

The scattered plots in Figure 4.10 compare the performance of ten different ML models and predict their dye degradation efficiencies. Each plot displays the training and test data points where the pink points represent the training data, and the blue points represent the test data. Ideally, the points should align closely with the diagonal line, representing a perfect correlation between the predicted and experimental values, indicating the model's accuracy. Among the models, CatBoost (Figure 4.10(c)), Gradient Boosting (Figure 4.10(f)), HistGradientBoosting (Figure 4.10(g)), Light GBM (Figure 4.10(h)) and XGBoost (Figure 4.10(j)) demonstrate the closest alignment to the diagonal line, showcasing their superior predictive performance with minimal deviation for training and testing data points. The strong correlation shown in these models indicates their resilience and excellent capacity to forecast the efficiency of MB degradation. Notably, the Bagging, Decision Tree, Extra Trees and Random Forest ML models (as shown in Figures 4.10(b), (d), (e), and (i), respectively) displayed a wider distribution around the diagonal line, especially in the testing dataset. These ML models suggested that the four models demonstrated relatively low predictive accuracy and that they might encounter overfitting problems during the training phase. The scatter plots for the AdaBoost model (Figure 4.10(a)) exhibit a moderate level of performance, characterized by a more compact clustering around the diagonal line compared to the weaker models, albeit not as close as the top-performing models. This model offers predictions with a moderate level of variation, suggesting a balanced performance across the datasets. The scatter plots provide a visual comparison of the predictive capability of each model, emphasizing the strengths of ensemble-based approaches such as CatBoost, HGB, GB, LightGBM and XGBoost in modeling complex nonlinear interactions such as MB dye deterioration.

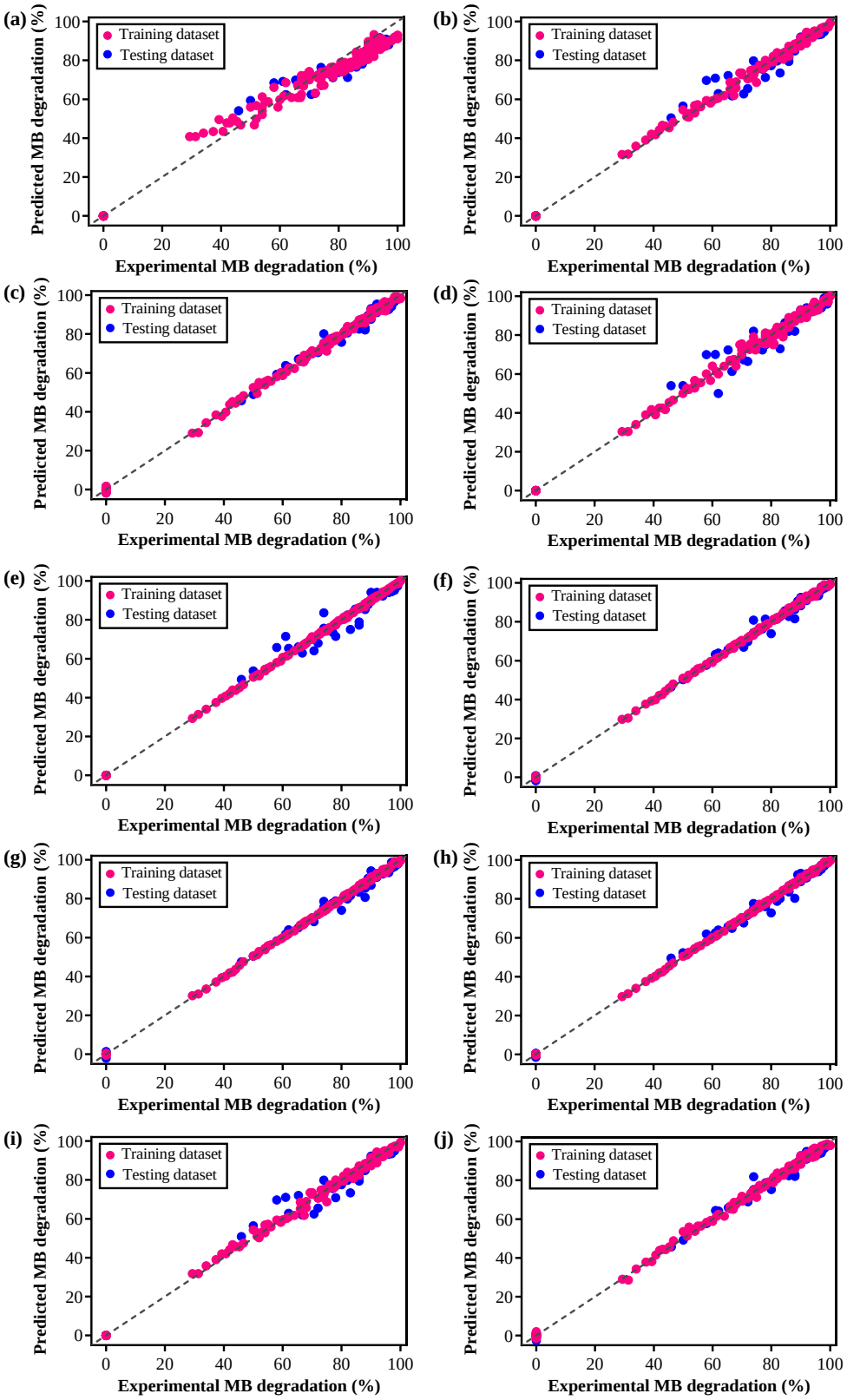

Figure 4.10 The scatter plot illustrates the correlation of experimental and predicted MB dye degradation efficacy as evaluated by the (a) AB, (b) Bagging, (c) CB, (d) DT, (e) ET, (f) GB, (g) HGB, (h) LGB, (i) RF and (j) XGBoost models.

To further interpret the assessment and analysis of the predicted results obtained from the models developed, a residual plot was designed and presented in Figure 4.11. The data points were sorted in an ascending magnitude order in the x-axis and then filtered using Bayesian methods. Residuals are close to the zero-line, indicating that the model is also reliable and follows a normal distribution [244]. In this light, the residual divergence of the AdaBoost, Bagging, Decision Tree, and Random Forest are very high, especially within higher percentage predictions for MB dye degradation. The residual plots show a big spread in the variance between the experimental and predicted values. The y-axis ranges from -15 to +15, with some values gathering above and below zero. Higher residue ranges indicate that the models give high residue errors that demonstrate poor model accuracy in predicting the degradation of MB for larger actual degradation data. Hence, predictions made by the models are less accurate. This could also mean problems with model generalization, particularly for the more extreme values within the dataset, which is evidenced by the presence of an unsmooth residual distribution.

For the residuals plot, the y-axis of the HGB model shows a range of -8 to +8. This indicates a larger degree of accuracy and practically no margin of error in the model's predictions. Residuals are evenly distributed along the expected range of MB degradation, suggesting that this model has the ability to make consistent predictions of dye degradation without any significant bias or variance. The even distribution of residuals indicates that this model can handle the intricacies of this dataset and can thus be very reliable for real-world applications. Among the models, a special mention goes to the compact clustering around zero of CB (Figure 4.11(c)), GB (f), LightGBM (h), and XGBoost (j), showing a slightly wider distribution (-10 to +10) compared to HGB (g). The plot exhibit a uniform

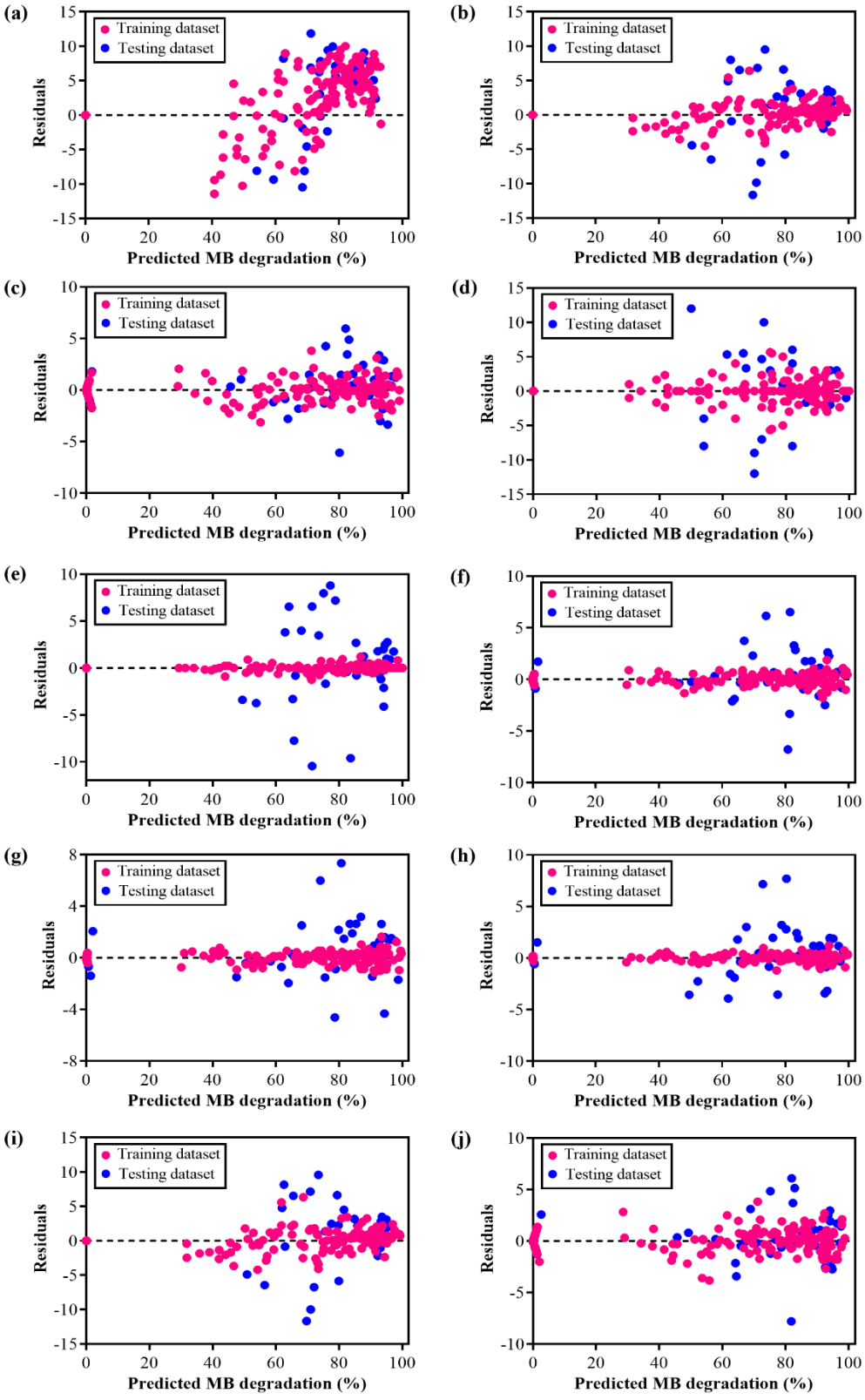

Figure 4.11 The residual plot illustrates the correlation of experimental and predicted MB dye degradation efficacy as evaluated by the (a) AB, (b) Bagging, (c) CB, (d) DT, (e) ET, (f) GB, (g) HGB, (h) LGB, (i) RF and (j) XGBoost models.

distribution, suggesting that these models provide robust prediction capabilities with only a few exceptional cases.

These outliers may arise due to the models' susceptibility to certain data points or fluctuations in the dataset. Nevertheless, these occurrences are infrequent, indicating that the models are typically dependable but might be improved through more fine-tuning or changed to enhance their prediction precision. The ET model, depicted in Figure 4.11e, has residuals that are closely grouped around the zero line, particularly for the training dataset, similar to the HGB model, but gives more scatter data points for testing. This arrangement between these factors demonstrates highly accurate forecasting ability with little systematic and random errors, even when considering various levels of MB degradation for testing prediction. The minimal spread of errors indicates the model's ability to extrapolate from the training data to the testing data, rendering them highly suitable for precise and dependable predictions.

The evaluation of ten studied machine learning models was assessed through five common statistical metrics such as R^2, MSE, RMSE, MAE, and MedAE, to investigate further their accuracy, robustness, and overall predictive capability for predicting photocatalytic degradation. The coefficient of determination (R^2) describes quantitatively how well the model explains the variance in the degradation efficiency of input variables alone. A higher R^2 means the model captures the most vital factors determining photocatalytic performance. The R^2 values of nearly 1 reflect a strong relationship between experimental and prediction values, reflecting an accurate model fit. The near-perfect R^2 scores observed in the training dataset are indicative of excellent fine-tuning of hyperparameters [42, 43]. The Mean Squared Error (MSE) and the Root Mean Squared Error (RMSE) calculate the average squared and square-rooted deviations between predictions and actual values, respectively [42]. While MSE focuses more on large deviations due to its quadratic term, RMSE yields an

interpretable error metric in the same units as the target variable, and hence offers ease of interpretation with regards to the accuracy of the prediction [43, 245].

Table 4.7. Performance matrices of studied ML models

Model		**R^2**	**MSE**	**RMSE**	**MAE**	**MedAE**
AdaBoost	Training	0.9758	24.988	4.998	4.006	4.0
	Testing	0.9351	42.907	6.550	5.691	6.519
Bagging	Training	0.9976	2.445	1.563	1.062	0.698
	Testing	0.9686	20.740	4.554	3.375	2.293
CatBoost	Training	0.9987	1.251	1.118	0.866	0.729
	Testing	0.9910	5.915	2.432	1.901	1.430
Decision Tree	Training	0.9973	2.782	1.668	1.008	0.500
	Testing	0.9650	23.119	4.808	3.465	2.500
Extra Trees	Training	0.9998	0.110	0.332	0.194	0.066
	Testing	0.9728	17.939	4.235	3.055	2.050
Gradient Boosting	Training	0.9997	0.281	0.530	0.411	0.311
	Testing	0.9911	5.865	2.420	1.708	0.980
HistGradient Boosting	Training	0.9998	0.206	0.454	0.354	0.292
	Testing	0.9915	5.592	2.365	1.781	1.473
LightGBM	Training	0.9998	0.131	0.732	0.274	0.230
	Testing	0.9900	6.566	2.696	1.917	1.660
Random Forest	Training	0.9977	2.378	1.542	1.047	0.650
	Testing	0.9682	20.983	4.581	3.378	2.230
XGBoost	Training	0.9986	1.356	1.164	0.868	0.668
	Testing	0.9800	6.591	2.567	1.835	1.261

Mean Absolute Error (MAE) provides a simple estimate of the average prediction error that does not give heavy penalties to outliers and hence gives an overall

view of model accuracy over typical cases. On the other hand, Median Absolute Error (MedAE) is the median of absolute errors, which is useful when there are outliers or anomalous conditions of degradation since it identifies the typical error of the prediction. Low values of MSE, MAE, and MedAE reflect better performance in that model, with minimum deviation of the model's predictions from the actual data points. Similarly, a lower RMSE means that the predictions are more accurate [42, 246]. Collectively, these metrics allow an overall model performance evaluation, thereby supporting the selection of models that give not only sufficient accuracy in predicting photocatalytic degradation but also robustness in response to changes in experimental conditions. These metrics also provide significant information about the ability of each model to accurately fit the training data and generate predictions on unknown data. The comprehensive findings are included in Table 4.7, and the radar plot in Figure 4.12.

The HGB model performed outstandingly well on both the training and testing data. In this model, the R^2 for the training set was very high at 0.9998, and the error metrics were all the lowest compared to all the metrics: MSE of 0.206, RMSE of 0.454, MAE of 0.354, and MedAE of 0.292. These metrics show a robust fitting result for the training data. During the testing phase, the model consistently achieved a good R^2 value of 0.9915 while exhibiting rather low error metrics: 5.592 for MSE, 2.365 for RMSE, 1.781 for MAE, and 1.473 for MedAE. So, the HGB model could achieve a substantial balance between high precision and efficient generalization to unseen data. The performances of Gradient Boosting (GB) and CatBoost (CB) models exhibited good performance, with high values of R^2 and showing a relatively small difference in other metrics. For example, the GB model has a training set R^2 value of 0.9997 and a testing set R^2 value of 0.9911, along with low values of MSE, RMSE, MAE, and MedAE (Table 4.7). Similarly, the CB provides an R^2 of 0.9987 on the training set and 0.9910 on the testing set. Both models have demonstrated excellent accuracy during training, while their results

on the testing set are excellent but slightly higher error matrices than the HGB model. Therefore, the performance of these models is comparatively lower for the prediction of MB. Extra Trees achieves an R^2 of 0.9998 on the training set but faces a significant drop in performance on the test set, with a mere R^2 value of 0.9728. LightGBM and XGBoost attained an outstanding performance in training efficiency. Similarly, XGBoost demonstrated strong performance, as evidenced by an R^2 value of 0.9986 in training and 0.9800 in the testing phase. However, both of these models exhibited comparatively higher evaluation metrics errors than the HGB, CB and GB models. In Random Forest, R^2 drops from 0.9976 during training to 0.9686 during testing. Accompanied by high testing error values: MSE of 20.983, RMSE of 4.581, MAE of 3.378, and a MedAE of 2.230. Decision Tree faced a drastic drop in R^2 values from 0.9973 during training to 0.9650 during testing. Although it performs well, other slightly larger metrics on the testing data (Table 4.7) suggest that the model might overfit, especially with simpler, unoptimized tree structures.

Among the diverse ensemble and boosting models, both AdaBoost and Bagging showed moderate performances. For example, the AdaBoost attained a respectable R^2 value both on the training data at 0.9760 and on the test set at 0.9317; hence, it can explain a great deal of variance in dye degradation. However, its relatively high RMSE values, which were 4.991 for training and 6.719 for testing, indicate problems in dealing with complex interactions within the data. Therefore, it may lead to overfitting with respect to robust models, such as HistGradientBoosting or CatBoost model. The Bagging ensemble exhibited slightly better predictive stability with R^2 scores of 0.9976 for the training and 0.9686 for testing. Additionally, it recorded a lower RMSE values: 1.563 for training and 4.554 for testing, showing better balancing between accuracy and generalization. Though this Bagging model performs better in generalizability and lower prediction error variance, it still falls short of the top execution models,

considering that CatBoost and HistGradientBoosting produced higher R^2 scores with less than the other four metrics. These observations indicate that while AdaBoost and Bagging perform well, they tend to lose some precision and robustness in fully modeling the complexity of photocatalytic dye degradation compared to the advanced ensemble methods.

The radar plot presents a comprehensive visualization of a model's performance for photocatalytic dye degradation. The purple and brown-shaded areas represent the training and testing metrics, respectively. The compact purple area indicates the lower values of error metrics such as R^2 score, MSE, RMSE, MAE, and MedAE, reflecting that the model achieves high accuracy and minimal prediction errors on training data, as shown in Figure 4.12. In contrast, the broader brown area for the testing data represents higher values of the given error metrics, suggesting larger prediction errors and lower accuracy when the studied model is applied to new, unseen data [42, 43]. The difference between the training and testing metrics indicates possible overfitting where the model excels on the training set but generalizes poorly on the testing set. Thus, the radar plot depicts the limitation of the model in the prediction of unseen data and ascertains further tuning or regularization to improve generalisation and reduce the performance differences between training and testing.

In the radar plot analysis of training datasets, distinguished models such as CatBoost (Figure 4.12(c)), Gradient Boosting (Figure 4.12(f)), and HGB (Figure 4.12(g)) presented great areas in the upper-performance region. These models displayed high training values of R^2, indicating a very good fit with the data on which the models were trained, whereas each model gives relatively low error metrics: MSE, RMSE, MAE, and MedAE. The distribution values of these metrics are located across large and well-concentrated areas in the radar plots, which can better interpret training data (purple-shaded area) into models with less error, but test datasets (brown-shaded area) reveal variations in the generalization

capabilities of the models. Among them, the HGB model (Figure 4.12(g)) surpasses the other models because it retains a significant portion of its optimal performance area, reflecting its robustness and good generalization to unseen data. The matrices of the testing set represent a relatively large region of the radar plot, and the model's high R^2 as well as the low error of metrics (MSE = 0.21, RMSE = 0.45, MAE = 0.35, and MedAE = 0.29), reveal uniqueness in generalization of the HGB model. Conversely, some models like AdaBoost (Figure 4.12(a)), Bagging (Figure 4.12(b)), Decision Tree (Figure 4.12(d)), Extra Trees (Figure 4.12(e)), and Random Forest (Figure 4.12(i)) show more significant gaps between the performances of training versus testing. It points out that performance decreases, which means these models are susceptible to overfitting despite the successful training metrics. AdaBoost exhibits a much larger area on the testing plot for their respective metrics (MSE = 42.91, RMSE = 6.55, MAE = 5.69, and MedAE = 6.52) and a much smaller area on the training plot (MSE = 24.99, RMSE = 5.00, MAE = 4.01, and MedAE = 4.0), indicating potential overfitting. Similarly, Bagging, DT, ET and RF also demonstrate significant performance drop in the testing set, with radar plots showing smaller areas in the optimal range and larger areas indicating poorer performance. These discrepancies are reflected in increased error metrics and reduced values of R^2, highlighting the challenges models face, from training data to unseen data. The sensitive variations in predictive capabilities stem from several factors, including data characteristics, the diversity of photocatalyst, the nature of contaminant, the input variables, and the algorithms employed. Despite these variations, the favorable R^2 values across all ten studied models indicate a high level of accuracy and a reliable correlation between experimental and predicted data. This indicates that these models are well for predicting MB dye degradation by photocatalysts in aqueous media.

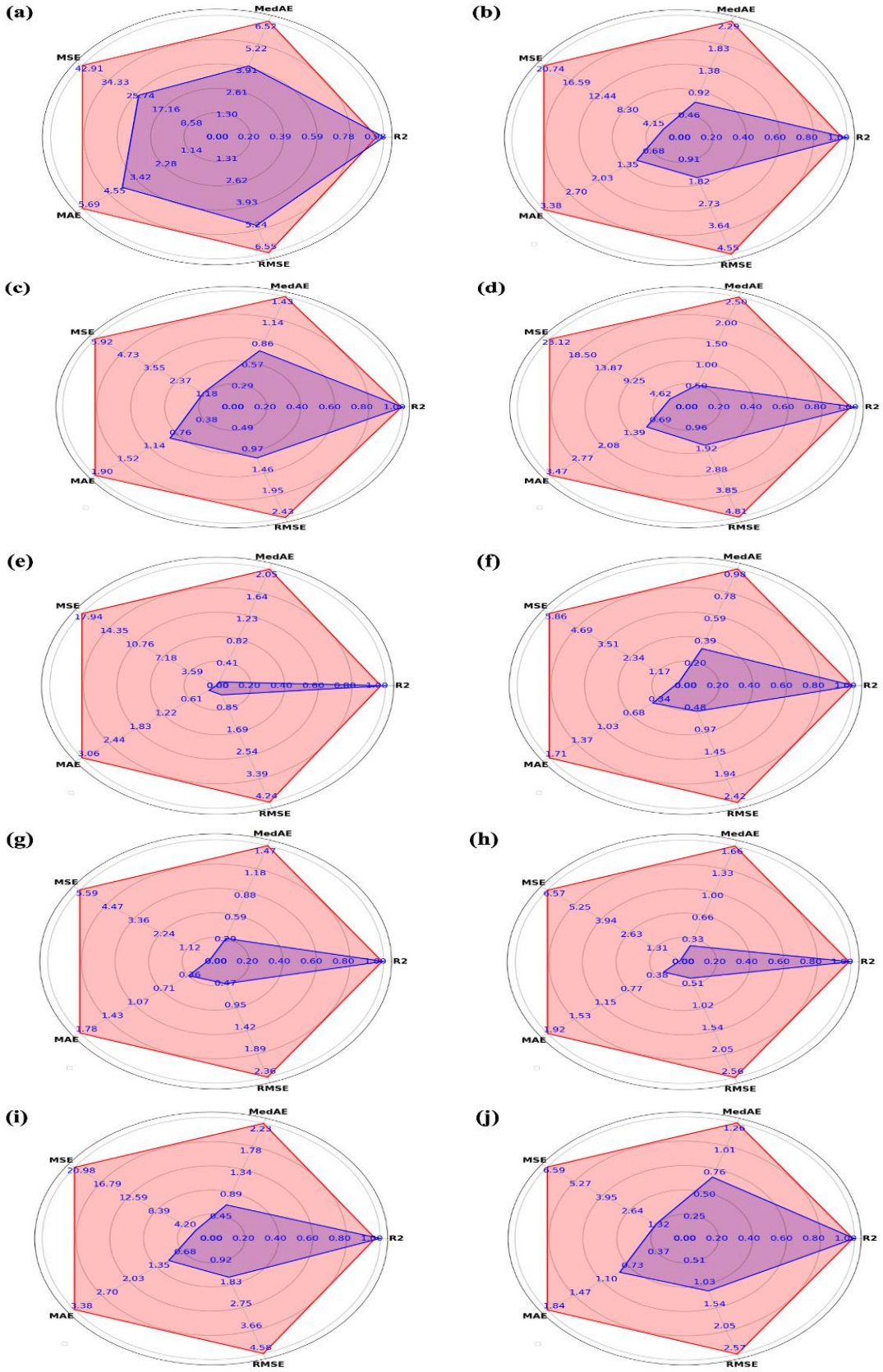

Figure 4.12 The radar plot on training and testing data (a) AB, (b) Bagging, (c) CB, (d) DT, (e) ET, (f) GB, (g) HGB, (h) LGB, (i) RF and (j) XGBoost models.

4.5 Normalized Importance of Variables

Several factors influence the degradation of methylene blue on the photocatalyst, and the significance of these factors varies. Figure 4.13 presents a comprehensive relationship between input features and the efficiency of MB dye degradation. The Figure illustrates the various normalized importance that affects the MB degradation efficiency. It showed that the treatment time was a pivotal factor in all models (> 0.80). The concentration of MB dye in the photocatalytic process is identified as the second most critical factor across all models, exhibiting a normalized importance over 0.10. It's worth noting that the consideration of the contaminant concentration was vital across the 189 datasets of the photocatalytic process. This indicates that a higher concentration of dye materials necessitates greater doses of photocatalyst. The dye degradation performance is also affected by light intensity, which can influence the efficiency of MB dye degradation and alter the surface charge density of the photocatalyst. This was the third key feature of this study [247, 248]. The physical properties of photocatalysts have a substantial impact on dye degradation, aligning with the traditional concept of dye breakdown. Assessing the significance of various input parameters can provide insights into understanding the mechanisms involved in dye degradation and inform potential improvements in the photocatalytic process in the future. Table 4.5 outlines the feature importance of each variable in the studied model and their influence on the photocatalytic dye degradation process. Thoughtful decisions were made when optimizing the machine learning model for specific tasks, striking a balance between the network's complexity and regularization in order to maximize its learning performance.

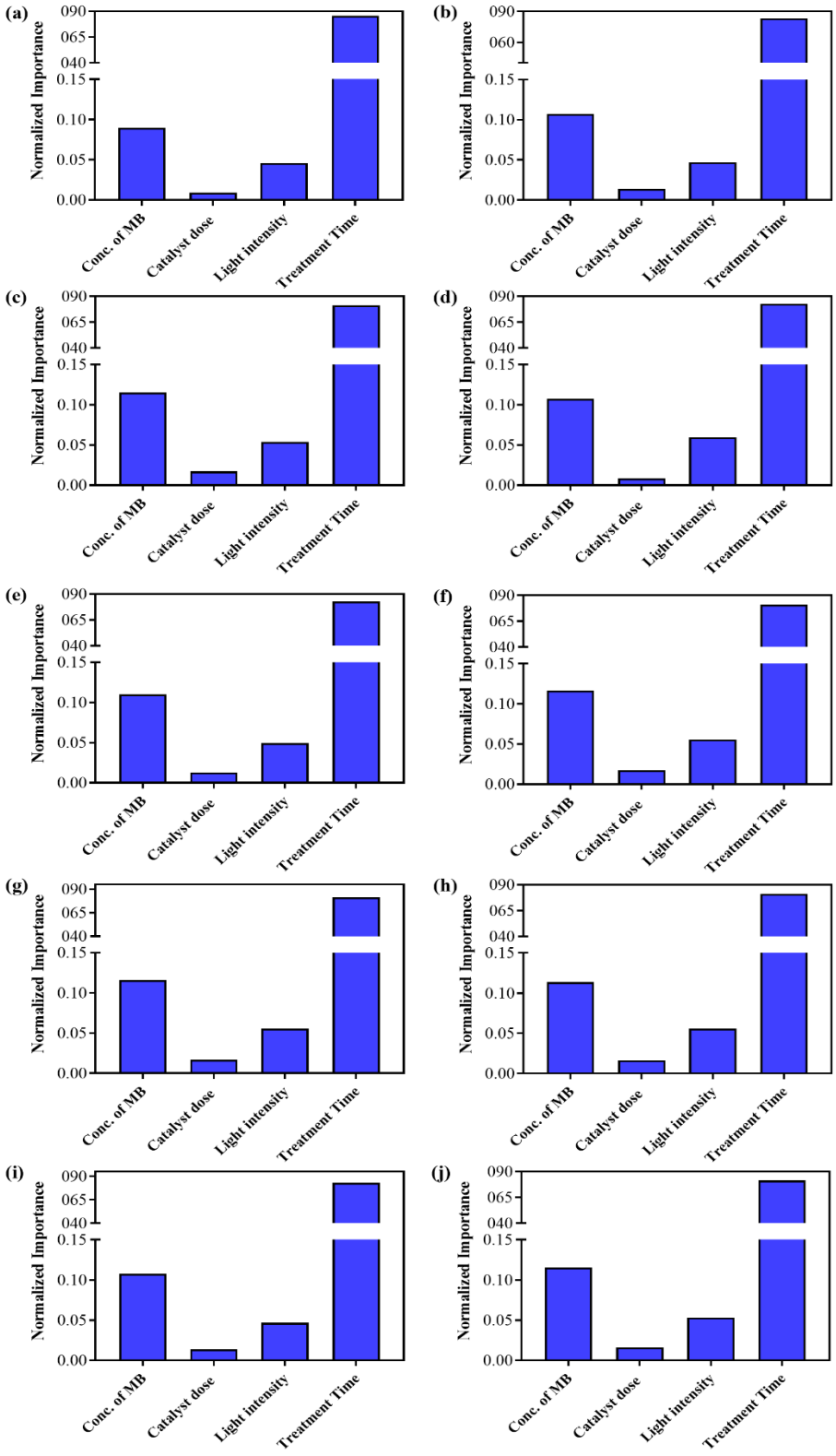

Figure 4.13 The Feature importance analysis for the input and output parameters for MB dye degradation efficiency as evaluated by (a) AB, (b)Bagging, (c) CB, (d) DT, (e) ET, (f) GB, (g) HGB, (h) LGB, (i) RF and (j) XGBoost model.

4.6 Best Model and Its Validation

Model robustness is defined as the ability of a model to maintain consistent performance when faced with new data rather than test data. It is crucial to show the stable performance of an effective model. An assessment was conducted to ascertain the accuracy of predictions through a robustness study. Three sets of modified testing datasets were generated by introducing different levels of Gaussian white noise into the original test datasets [249]. The robustness of the HGB model clearly exhibited its constant performance across a range of Gaussian white noise levels Table 4.8. Although noise levels were between 60% and 80%, the model achieved impressive R^2 scores, demonstrating a strong relationship between experimental and predicted values. It was able to retain an R^2 value of >0.9902 at three noise levels from 60% to 80%, while keeping the very same MSE of 6.3168, RMSE of 2.5133, MAE of 1.9721, and MedAE of 1.3734 at 60% noise as proof of its resilience in maintaining high accuracy against extreme perturbation in the data. At 80% noise, the model performance interestingly bit reduced and fewer error metrics of MSE: 6.5610, RMSE: 2.5614, MAE: 1.9990, MedAE:1.4753, which is indicative that the model is not just robust but can adapt to a certain noise level. These findings underpin the robustness of the HGB model when it comes to making reliable predictions in noisy data with position and pose the model as a forceful candidate in real-world deployment, where the data quality may vary.

Table 4.8. Model robustness test by introducing Gaussian white noise.

Percentage of Noise	R^2 Score	MedAE	MSE	MAE	RMSE
60%	0.9903	1.3734	6.3168	1.9721	2.5133
70%	0.9905	1.5397	6.2048	1.9205	2.4909
80%	0.9902	1.4753	6.5610	1.9990	2.5614

SHapley Additive exPlanations (SHAP) analysis offers a robust and precise measure for assessing the feature importance by attributing the variation in the model output to specific features. This approach provides a comprehensive analysis of the ways in which each feature contributes to the predictions derived from cooperative game theory. It enables the visualization and understanding of how individual features influence the model's predictions, fostering transparency and confidence in its functioning. Figure 14a shows the plot of the importance of the studied best HGB model globally for the features in predicting MB dye degradation efficiency. The treatment time, with the importance score of +22.26, was the most affecting variable, followed by concentration of MB with +6.08, light intensity with +3.72, while catalysts doses had minor effects with +2.82. This plot shows the most informative features about the decisions that are coming out of the model. The SHAP summary plot presented in Figure 4.14(b) confirms this research observation by showing each feature and how it has influenced the HGB model output. The SHAP values indicate that the treatment time, concentration of MB, light intensity and doses of photocatalyst have a significant impact on the model's predictions. This confirms the importance of feature ranking illustrated in Figure 4.14.

The evaluation metrics of the studied ML models is illustrated in Table 4.7. Among these, the HGB model with optimized Bayesian techniques exhibited superior efficacy to predict methylene blue. The HGB model identified an

optimal predicted value (Table 4.9) for experimental validation, forecasting a maximum MB dye degradation efficiency of 98.99% under the following conditions: an initial MB concentration of 10 mg/L, a catalyst dose of 200 mg/L, a light intensity of 150 mW/cm², and a treatment time of 88.6 minutes. Experimental results yielded approximately the same degradation efficiency of 98.50% under the same conditions. The final model metrics, including an R^2 score of 0.9915, MedAE of 1.171, MSE of 5.634, MAE of 1.735, and RMSE of 2.374 suggest that the Bayesian-optimized model efficiently predicts MB dye degradation.

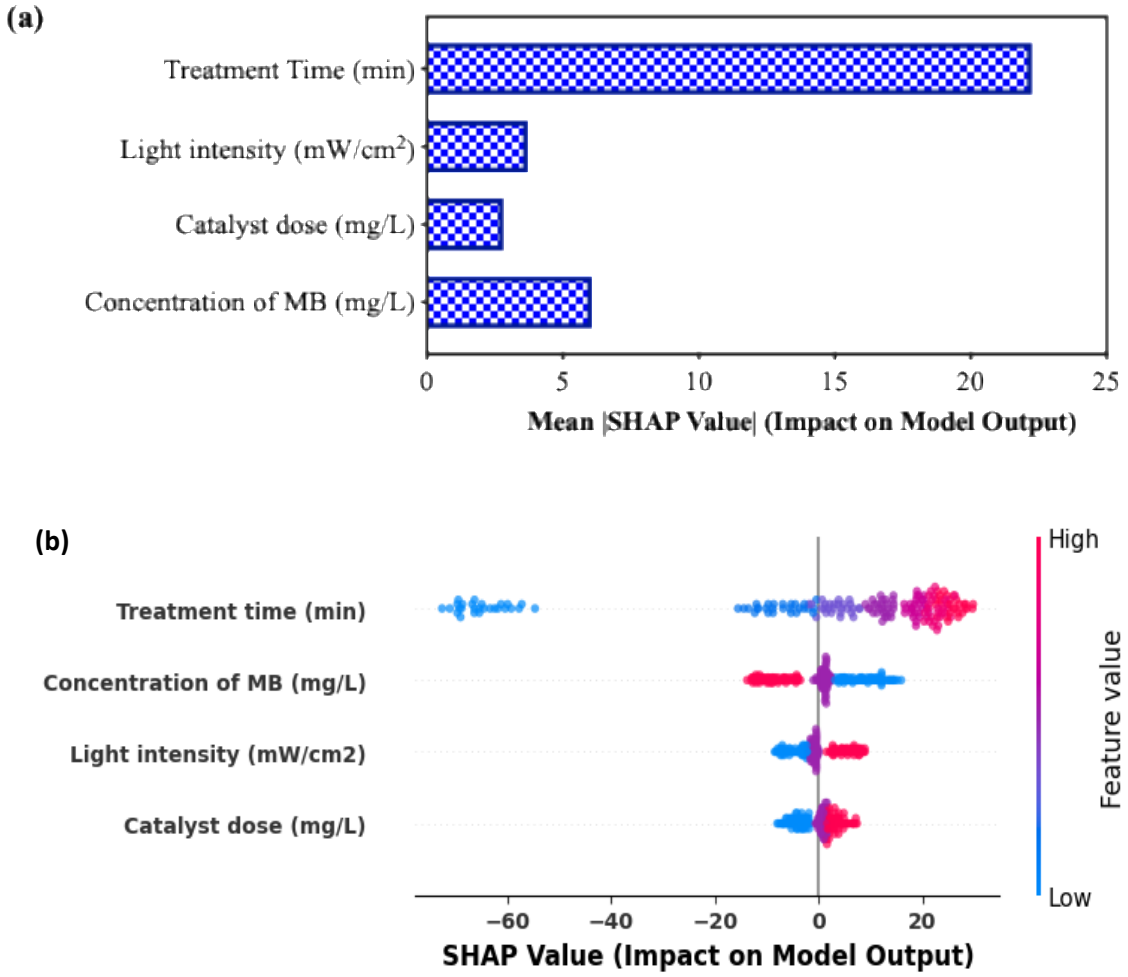

Figure 4.14 (a) Global feature importance assessed through SHAP values, (b) The summary plot (beeswarm plot) illustrates the distribution of feature impacts on HGB model.

Table 4.9. Optimized parameters for the HGB model

Initial Conc. of MB (mg/L)	Catalyst dose (mg/L)	Light intensity (mW/cm²)	Treatment time (min)	Predicted MB degradation efficiency (%)	Experimental MB degradation efficiency (%)
10	200	150	88.6	98.99	98.50

4.7 Comparision for the Prediction dye Degradation

The validation of the studied ML was conducted using data sources from a range of existing literature that examines the prediction of chemical contaminants, especially pharmaceutical compounds and dye material degradation performance in different water metrices. The removal efficiency of dye contaminants by various nanomaterials and/or catalysts, and the predictive capabilities of diverse ML approaches is detailed in Table 4.10. This research encompasses 189 data sets along with four input features; however, the dataset analyzed is comparatively higher for some experimental data [250-252] but lower than some reported data [253-255]. The inclusion of numerous variables is generally unfavourable, as it tends to increase both computational time and data collection expenses. The superior R^2 value evident in the current study, when compared to previous research [250-254], can be attributed to various factors. In the context of performance metrics, an R^2 value of 0.8 is indicative of strong regression model performance [245]. Considering that some sources do not provide values for all the required variables, the incompleteness of the data input significantly lowers the accuracy of the prediction. Thus, the predictive power of this model can be further improved. Table 4.10 presents a comparison between the results obtained in the current study and those reported in earlier published studies regarding the catalytic degradation of organic dye pollutants. It was observed from the results that the HGB model developed in this work outperforms most of the previously published models, with higher R^2 and lower

MAE, MSE, RMSE, MedAE values. Therefore, the HGB model developed from this research enjoys much better predictive performance and is closer to real-world applications.

Table 4.10. Removal of various chemical contaminants and their prediction using different machine learning models.

Contaminants and photocatalyst	**ML algorithms**	**Best model**	**Number of data points**	**Number of input features**	**R^2**	**Ref.**
Ethyl violet by Mn-doped Fe -modified reduced graphene oxide	RSM, ANN-GA and ANN-PSO	ANN-GA	30	4	0.9940	[251]
Methylene blue and rhodamine B by six metal oxide (ZnO, SnO_2, Fe_2O_3, TiO_2, WO_3, and β-MnO_2)	CGCNN-MF-ANN	CGCNN-MF-ANN	50	7	0.746	[256]
Eriochrome black-T-modified clay	RSM, ANFIS and ANN	ANFIS	234	4	0.9920	[253]
Methylene blue by graphene oxide/chitosan composites	RSM and ANN-PSO	ANN-PSO	17	3	0.998	[252]
Malachite green by noble metal-doped $BiFeO_3$ (NM-$BiFeO_3$)	Bagging, CB, DT, ET, GB, HGB, LGBM, GaussianProcess, ANN and LightLSTM	CB	1200	10	0.999	[254]

Malachite green by noble metal-doped $BiFeO_3$ (NM-$BiFeO_3$)	Gaussian process regression (GPR)	Matern-GPR	1200	10	1.00	[257]
Methyl orange and crystal violet by MgFeAl-layered triple hydroxide	DT, RF, ET	ET	40	4	0.9970	[250]
Rhodamine B by neodymium-doped titanium dioxide (Nd-TiO_2)	ANN	ANN	308	7	0.99	[255]
Methylene blue by $CuWO_4$@TiO_2 photocatalyst	AB, Bagging, CB, DT, ET, GB, HGB, LGBM, RF and XGB	HGB	189	4	0.9915	This study

4.8 Degradation of MB by $CuWO_4$@TiO_2 NCs Using Photocatalysis Process

The extensive utilization of heterogeneous catalysis processes for the degradation of dyes has garnered significant interest due to their exceptional efficiency. The $CuWO_4$@TiO_2 nanocomposite serve as a solid-phase catalyst in the Photocatalysis processe, thereby producing various ROS, that degrades the dyes present in aqueous solution. To know photocatalytic performance on the degradation of MB dyes was investigated for the reaction conditions (10 mg/L of MB, 150 mW/cm^2 light intensity, 200 mg/L of $CuWO_4$@TiO_2 nanocomposite, reaction time 90 minutes) by changing the photocatalysis process.

4.8.1 Degradation of Methylene Blue by Photocatalysis Process

Recent advancements in semiconductor and composite photocatalysts have focused on their ability to degrade ecologically hazardous organic dyes under solar irradiation. The photocatalytic performance of TiO_2, $CuWO_4$, and $CuWO_4@TiO_2$ nanocomposites (NCs) was systematically evaluated for methylene blue (MB) dye removal under solar-simulated light ($\lambda \geq 665$ nm), as illustrated in Figure 4.15.

Prior to irradiation, all dye-catalyst mixtures were kept in the dark for 15 minutes to ensure adsorption–desorption equilibrium. As seen in Fig. 4.15(a), the UV–Vis absorption spectra of MB in the presence of $CuWO_4@TiO_2$ show a continuous decrease in intensity at the characteristic peak near 664 nm over 90 minutes, indicating efficient degradation. The initially deep blue color of the MB solution progressively faded and became almost colorless, visually confirming the breakdown of dye molecules.Comparative studies (Fig. 4.15 b–d) revealed that both $CuWO_4$ and TiO_2 demonstrated relatively lower degradation efficiencies under identical conditions. While $CuWO_4$ showed moderate activity, TiO_2 was the least effective—attributable to its limited visible-light absorption and faster electron–hole recombination. Control experiments in the absence of photocatalysts showed negligible changes, confirming the stability of MB under solar irradiation alone.The degradation kinetics (Fig. 4.15e) further validated the superior photocatalytic activity of $CuWO_4@TiO_2$. After 90 minutes of irradiation, $CuWO_4@TiO_2$ achieved ~100% MB degradation, compared to ~80% for $CuWO_4$ and ~75% for TiO_2. The blank control showed no significant degradation, reinforcing the essential role of photocatalysts.This enhanced performance of $CuWO_4@TiO_2$ nanocomposites is attributed to the formation of an effective heterojunction, which facilitates improved charge carrier separation and reduces recombination. Additionally, the broader light absorption capability due to the $CuWO_4$ core allows better harvesting of the solar spectrum. In conclusion, $CuWO_4@TiO_2$ nanocomposites exhibit the most efficient photocatalytic

performance among the tested materials, making them a strong candidate for environmentally friendly wastewater treatment applications under solar illumination.

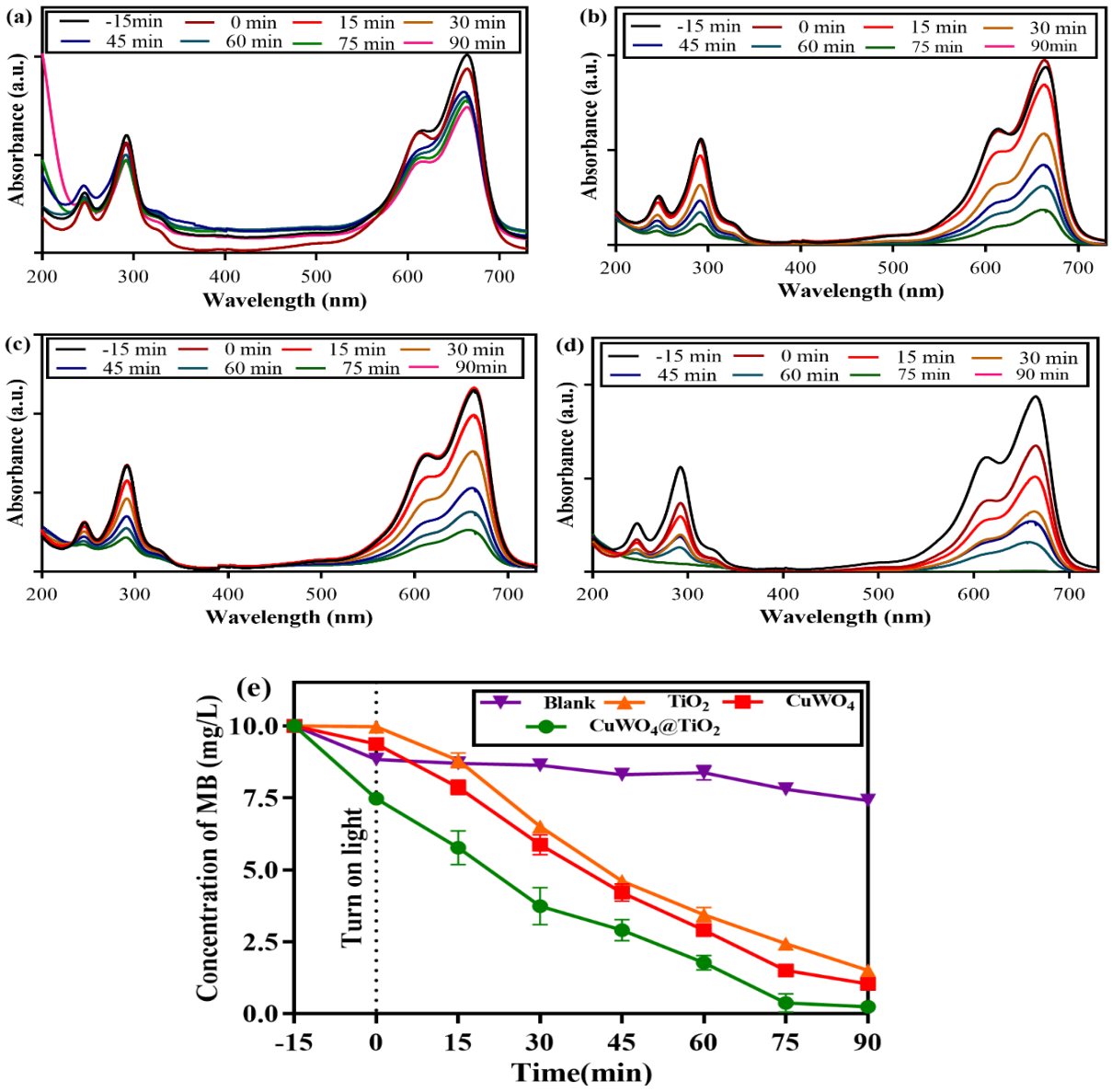

Figure 4.15 Photocatalytic MB dye degradation by $CuWO_4@TiO_2$, (b) $CuWO_4$, (c) $CuWO_4@TiO_2$, (d) TiO_2 MB dye under solar simulated light by photocatalysis process at the following reaction conditions: 10 mg/L of MB, 150 mW/cm^2 light intensity, 200 mg/L of $CuWO_4@TiO_2$ photocatalyst, reaction time 90 minutes.

4.8.2 Kinetics of Photocatalytic MB Dye Degradation Reaction

For a better understanding of the efficient degradation of the prepared catalyst, the 1st order reaction through a Langmuir-Hinshelwood (LH) rule was used to measure the degradation of dyes is expressed in the following equation [258].

$$\ln (C_0/C) = kt \qquad (4.1)$$

where k is the first-order rate constant, C_0 and C are the initial and residual concentrations of MB, respectively, after irradiation time t (min). The pseudo-first-order kinetics modelling of the $CuWO_4$, TiO_2 and $CuWO_4$@TiO_2 were shown in Figure 4.16.

Table 4.11. Kinetic data for the degradation rate of MB

Photocatalysts	Rate constant	Correlation coefficient
$CuWO_4$@TiO_2	0.03018	0.9914
$CuWO_4$	0.01966	0.9754
TiO_2	0.0167	0.9159

All samples show a high determination coefficient value (R^2) indicating a good fit with the model. Moreover, the slope of the linear fit, which is define as the photocatalytic degradation rate were also calculated and the value were given in Table 4.11. It shows that $CuWO_4$ combine with TiO_2 increase the photocatalytic degradation towards MB dyes.

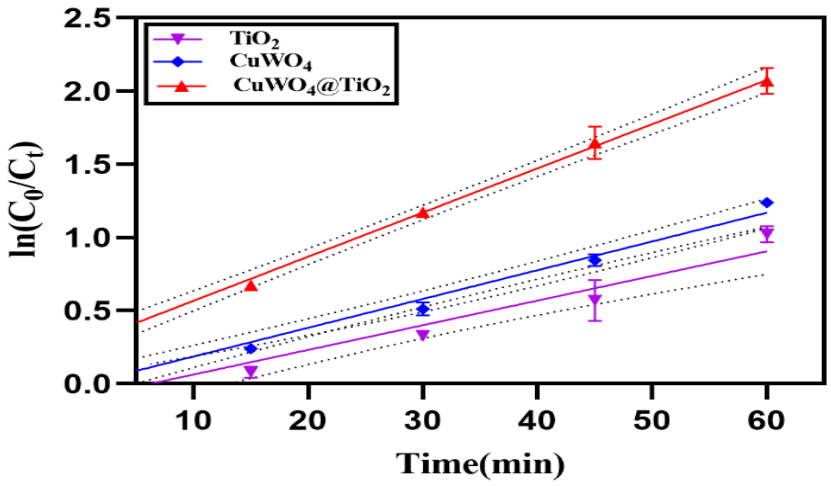

Figure 4.16 Kinetics of photocatalytic MB dye degradation reaction

4.9 Reactive Species Analysis of $CuWO_4@TiO_2$ NCs

To identify the dominant ROS in MB degradation, sodium azide (SA), potassium dichromate ($K_2Cr_2O_7$), superoxide dismutase (SOD), triethanolamine (TEOA), and isopropanol (IPA) were employed as radical scavengers for singlet oxygen ($^1O_2$), electrons (e^-), superoxide radicals ($O_2^{\bullet-}$), holes (h^+), and hydroxyl radicals ($HO^\bullet$), respectively [259, 260]. Each radical scavenger was dosed separately prior to catalyst addition, quenching its corresponding radical prior to reaction with the contaminants. The results of the scavenger tests, shown in Figure. 4.17(a) and 4.17(b) indicate that the addition of scavengers has been shown to reduce the efficiency of degradation by 89 %, 86 %, 78 %, 76 % and 88 % for TEOA, SA, IPA, SOD, and $K_2Cr_2O_7$), respectively. The data indicate that hydroxyl radicals, superoxide radicals, electrons, and holes played a pivotal role in the photodegradation process. The order of the active species in the photodegradation tests of MB dye with $CuWO_4@TiO_2$ is as follows: superoxide radicals are at the top, followed by $HO^\bullet$ radicals, electrons, singlet oxygen, and holes. When isopropanol and superoxide dismutase were added, the MB dye photodegradation process became less effective. The rates of degradation and

rate constants show that $HO^{\bullet}$ and $O_2^{\bullet-}$ radicals played a big role in slowing down the reduction and oxidation processes in the photocatalytic reaction.

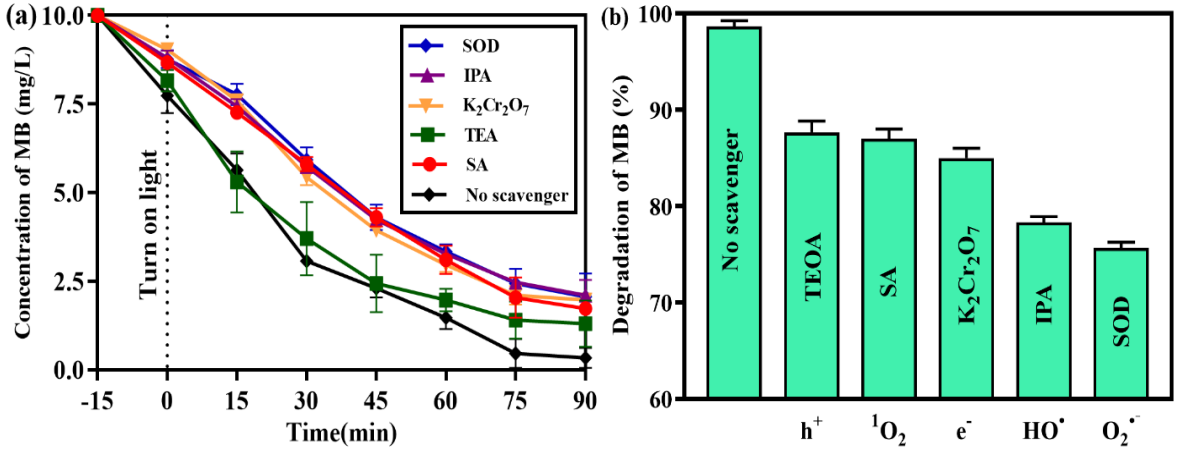

Figure 4.17 MB degradation by $CuWO_4$@TiO_2 with different scavengers

4.10 Proposed Reaction Mechanism

In the presence of a $CuWO_4/TiO_2$ heterojunction, the photocatalytic degradation rate of methylene blue (MB) is significantly enhanced under visible light irradiation. This improvement can be attributed to efficient charge separation and reactive oxygen species (ROS) formation due to the mechanism. The photogenerated charge carriers possess strong redox abilities but generally do not react directly with the organic dyes. Instead, they generate active species such as $HO^{\bullet}$ and $O_2^{\bullet-}$ radicals through the reaction of H_2O or O_2 by charge transfer and absorption. It is well learned that holes (h^+), $HO^{\bullet}$ and $O_2^{\bullet-}$ radicals are regarded as the reactive species of photocatalytic degradation of organic pollutants [261]. When the $CuWO_4/TiO_2$ heterojunction is irradiated by visible light with energy greater than or equal to its bandgap energy ($h\nu \geq Eg$), electron-hole pairs are generated in both semiconductors [262]. The electrons in the valence bands (VB) of both $CuWO_4$ and TiO_2 absorb energy and are excited to their respective conduction bands (CB), leaving holes in the valence bands. The conduction band of $CuWO_4$ is lower than that of TiO_2, so the photoexcited electrons in the CB of TiO_2 are transferred to the CB of $CuWO_4$. Concurrently, the holes in the VB of

$CuWO_4$ are transferred to the VB of TiO_2, creating a spatial charge separation that minimizes electron-hole recombination, thereby enhancing the photocatalytic degradation of MB using the $CuWO_4/TiO_2$ heterojunction [263]. The holes in the VB of TiO_2 can quickly react with adsorbed H_2O or OH^- to produce $HO^\bullet$. radicals. These $HO^\bullet$ along with $O_2^\bullet$ produced by the reduction of O_2 by electrons in the CB of $CuWO_4$, are the primary ROS responsible for the photodegradation of MB [261]. Electrons from the conduction region of TiO_2 recombine with holes in the valence region of $CuWO_4$, while the remaining high-energy electrons in $CuWO_4$ and holes in TiO_2 participate in redox reactions with water and oxygen [263].

The photodegradation mechanism of MB over $CuWO_4@TiO_2$ heterojunctions is proposed based on the interaction of the two semiconductors under visible light irradiation. The photocatalytic activity mainly arises from effectively separating photoinduced electrons and holes in the heterojunction [264]. When both $CuWO_4$ and TiO_2 are exposed to visible light, the electrons in their VB are excited to their respective CB, leaving holes in the valence band. The energy alignment between the two semiconductors helps separate charges, which is essential for degradation. The conduction band of $CuWO_4$ is at a lower energy level compared to that of TiO_2 [220]. As a result, the photogenerated electrons in the conduction band of TiO_2 migrate the conduction region of $CuWO_4$. Simultaneously, the holes in the valence region of $CuWO_4$ are moved the valence band of TiO_2 [265]. This charge migration enhances charge separation efficiency and minimizes the recombination of electrons and holes, a critical factor in improving the heterojunction system's photocatalytic activity. The holes in the valence band of TiO_2 possess strong oxidative potential. They can react with adsorbed H_2O or OH^- ion to produce $HO^\bullet$, which are highly reactive species in the degradation process [266]. The electrons in the conduction band of $CuWO_4$ can simultaneously reduce O_2 to produce $O_2^{\bullet-}$ anions. These ROS such as $HO^\bullet$ and $O_2^{\bullet-}$ are the primary agents that cause the oxidative degradation of MB.

The following set of reactions can describe the overall photocatalytic process:

$$CuWO_4@TiO_2 + h\nu \rightarrow CuWO_4(e^-_{CB}) + TiO_2(h^+_{VB})$$

$$e^-_{CB}\ (TiO_2) \rightarrow e^-_{CB}\ (CuWO_4)$$

$$h^+_{VB}(\ CuWO_4) \rightarrow h^+_{VB}(TiO_2)$$

$$h^+_{VB}(TiO_2) + H_2O \rightarrow H^+ + HO^\bullet$$

$$e^-_{CB}(\ CuWO_4) + O_2 \rightarrow 0^{\bullet -}_2$$

$$HO^\bullet + MB \rightarrow \text{Degraded Products}$$

$$0^{\bullet -}_2 + MB \rightarrow \text{Degraded Products}$$

4.11 Stability and Reusability Test of $CuWO_4@TiO_2$ NCs

The catalyst's stability under solar light irradiation is critical to implementing the photocatalysis technique in real time. Figure 4.18 shows the regeneration analysis under natural solar light irradiation with MB dye degradation over $CuWO_4@TiO_2$ NCs. According to the regeneration cycle data, $CuWO_4@TiO_2$ NCs can decompose MB and sustain a relatively high level. We conducted six sequential tests under the same conditions to study photocatalyst reuse. We recovered the materials by filtering, ethanol washing, and drying after each degrading cycle and then utilized them in the subsequent cycle. As seen in (Figure. 4.18), the regenerated catalyst's performance after five consecutive cycles is still outstanding for the photocatalytic degradation of MB. $CuWO_4@TiO_2$ NCs shows the maximum degradation efficiency for the first cycle was observed (99.99%), whereas an efficiency decrease was obtained for the third (96%) and fifth (92%) cycles in 90 min. After the sixth cycle, $CuWO_4@TiO_2$ ability to break down MB photocatalytically decreased by 10%. This shows that the catalyst is stable during

the continuous cycle of MB photodegradation, which suggests that it could be used as a stable photocatalyst for polluting dye for a long time.

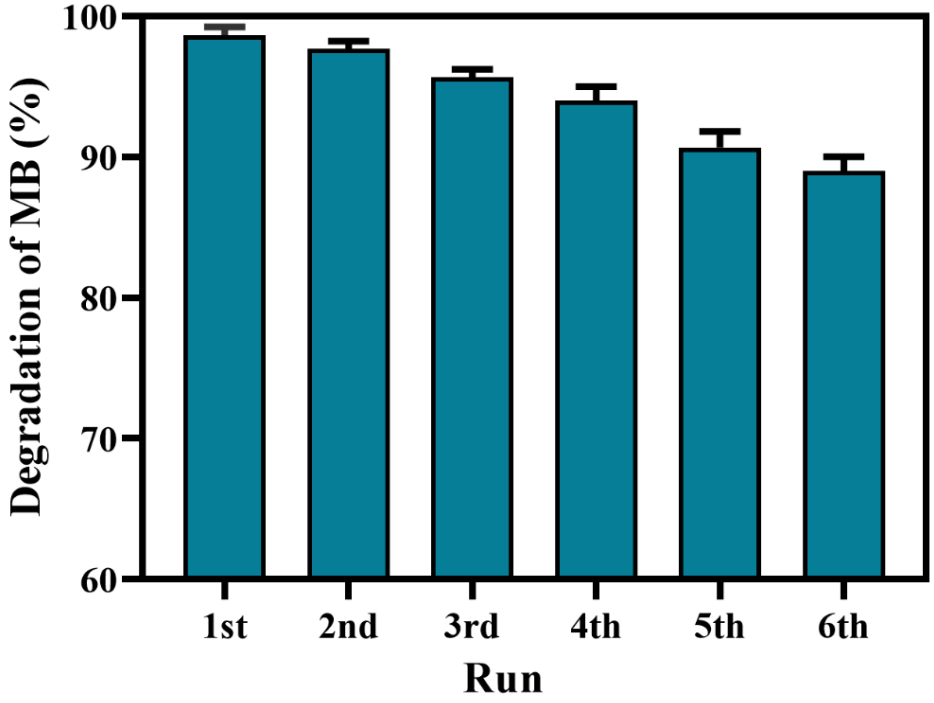

Figure 4.18 Stability and reusability test of $CuWO_4$@TiO_2 nanocomposites

Chapter 5: CONCLUSION & RECOMMENDATION

5.1 General Conclusion

The $CuWO_4$@TiO_2 nanocomposite was synthesized using a hydrothermal method to enhance photocatalytic degradation of methylene blue (MB) under visible light. Characterization revealed a low bandgap of 0.491 eV for the Ti/Cu@$CuWO_4$ configuration, which contributes to improved charge separation and photocatalytic efficiency. The degradation process followed a pseudo-first-order model, exhibiting a rate constant of 0.030 min^{-1}.

Machine learning models, particularly HistGradientBoosting, demonstrated high predictive accuracy, achieving R^2 values of 0.9998 for the training set and 0.9915 for the test set in forecasting degradation efficiency. The $CuWO_4$@TiO_2 nanocomposite outperformed both pure $CuWO_4$ and TiO_2, attributed to enhanced charge separation, and showed excellent reusability, making it a promising candidate for sustainable wastewater treatment.

This research advances the development of efficient photocatalytic materials and serves as a foundation for future studies aimed at applying these findings to real-world wastewater scenarios.

5.2 Key Findings

$CuWO_4$@TiO_2 nanocomposite exhibited significantly higher photocatalytic activity than pure $CuWO_4$ and TiO_2.

DFT analysis revealed improved electronic structure, charge transfer, and strong interaction between $CuWO_4$ and TiO_2, further supporting the enhanced photocatalytic performance

Methylene blue degradation reached up to 98.50% under optimized condition included 200 mg/L photocatalyst, 154 mW/cm^2 light intensity, 88 min reaction time, and 10 mg/L MB concentration.

Machine learning models predicted degradation efficiency with high accuracy, with HistGradientBoosting achieving $R^2 = 0.9915$.

$O_2^{\bullet-}$ and $OH^{\bullet}$ were identified as the dominant reactive species in MB degradation.

Six cycles of reuse demonstrated the stability and reusability of the $CuWO_4@TiO_2$ nanocomposite for wastewater treatment.

The integrated photocatalysis, machine learning, and computational DFT approach presents a promising, scalable solution for environmental remediation.

5.3 Limitation of the Study

The limitation of the study is that it was carried out only on a lab-scale base experiment.

5.4 Recommendation for Further Study

Given the growing concerns over water pollution, further research should focus on the practical application of $CuWO_4@TiO_2$ nanocomposites in real wastewater treatment to evaluate their effectiveness beyond controlled laboratory conditions. Expanding the scope of degradation to include a wider range of organic pollutants, industrial dyes, would provide a more comprehensive understanding of the catalyst's potential. Additionally, investigating the long-term stability and regeneration capacity of the nanocomposite across multiple reuse cycles is essential for assessing its economic feasibility. The role of active species in the degradation process should be further explored to optimize photocatalytic performance. Integrating advanced machine learning techniques for predictive modeling and process optimization could significantly enhance large-scale applicability. Moreover, the combination of $CuWO_4@TiO_2$ with other advanced oxidation processes may lead to improved degradation efficiency and a broader application spectrum.

REFERENCES

1. S. W. Cooley, J. C. Ryan, and L. C. Smith, "Human alteration of global surface water storage variability," *Nature*, vol. 591, no.7848, pp. 78-81, 2021.
2. M. Hao, M. Qiu, H. Yang, B. Hu, and X. Wang, "Recent advances on preparation and environmental applications of MOF-derived carbons in catalysis," *Science of The Total Environment*, vol. 760, 143333, 2021.
3. C. Yao, W. Zhang, L. Xu, M. Cheng, Y. Su, J. Xue, J. Liu, and S. Hou, "A facile synthesis of porous MXene-based freestanding film and its spectacular electrosorption performance for organic dyes," *Separation and Purification Technology*, vol. 263, 118365, 2021.
4. P. Ahuja, S. K. Ujjain, R. Kanojia, and P. Attri Transition Metal Oxides and Their Composites for Photocatalytic Dye Degradation. Journal of Composites Science, 2021. 5, DOI: 10.3390/jcs5030082.
5. N. C. Joshi, P. Gururani, and S. P. Gairola, "Metal oxide nanoparticles and their nanocomposite-based materials as photocatalysts in the degradation of dyes," *Biointerface Res. Appl. Chem*, vol. 12, 6557-6579, 2022.
6. J. R. Rajabathar, R. Thankappan, A. Sutha, H. Al-Lohedan, A. Mahmoud Karami, S. Ashok Kumar, G. Devendrapandi, S. Roji Marjorie, and R. Balu, "Enhanced photocatalytic activity of magnetite/titanate (Fe_3O_4/TiO_2) nanocomposite for methylene blue dye degradation under direct sunlight," *Optical Materials*, vol. 148, 114820, 2024.
7. I. Khan, K. Saeed, I. Zekker, B. Zhang, A. H. Hendi, A. Ahmad, S. Ahmad, N. Zada, H. Ahmad, L. A. Shah, T. Shah, and I. Khan Review on Methylene Blue: Its Properties, Uses, Toxicity and Photodegradation. Water, 2022. 14, DOI: 10.3390/w14020242.
8. C. Chen, W. Bi, Z. Xia, W. Yuan, and L. Li, "Hydrothermal Synthesis of the $CuWO_4$/ZnO Composites with Enhanced Photocatalytic Performance," *ACS Omega*, vol. 5, no.22, pp. 13185-13195, 2020.
9. L. Spitaleri, G. Nicotra, M. Zimbone, A. Contino, G. Maccarrone, A. Alberti, and A. Gulino, "Fast and Efficient Sun Light Photocatalytic Activity of Au_ZnO Core–Shell Nanoparticles Prepared by a One-Pot Synthesis," *ACS Omega*, vol. 4, no.12, pp. 15061-15066, 2019.
10. G. Tian, G. Yuan, A. Aleksandrov, T. Zhang, Z. Li, A. M. Fathollahi-Fard, and M. Ivanov, "Recycling of spent Lithium-ion Batteries: A comprehensive review for identification of main challenges and future research trends," *Sustainable Energy Technologies and Assessments*, vol. 53, 102447, 2022.

11. M. Aadil, S. Zulfiqar, M. Shahid, P. O. Agboola, N. F. Al-Khalli, M. F. Warsi, and I. Shakir, "Fabrication of CNTs supported binary nanocomposite with multiple strategies to boost electrochemical activities," *Electrochimica Acta*, vol. 383, 138332, 2021.

12. G. Liao, X. Tao, and B. Fang, "An innovative synthesis strategy for high-efficiency and defects-switchable-hydrogenated TiO_2 photocatalysts," *Matter*, vol. 5, no.2, pp. 377-379, 2022.

13. D. Manoj, S. Rajendran, Y. Vasseghian, S. Ansar, F. Gracia, and M. Soto-Moscoso, "Tailoring the heterojunction of TiO_2 with multivalence CeO_2 nanocrystals - for detection of toxic 2-aminophenol," *Food and Chemical Toxicology*, vol. 165, 113182, 2022.

14. R. Rajendran, S. Vignesh, S. Suganthi, V. Raj, G. Kavitha, B. Palanivel, M. Shkir, and H. Algarni, "g-C_3N_4/TiO_2/CuO S-scheme heterostructure photocatalysts for enhancing organic pollutant degradation," *Journal of Physics and Chemistry of Solids*, vol. 161, 110391, 2022.

15. M. Dubey, R. Kumar, S. K. Srivastava, and M. Joshi, "Visible light induced photodegradation of chlorinated organic pollutants using highly efficient magnetic Fe_3O_4/TiO_2 nanocomposite," *Optik*, vol. 243, 167309, 2021.

16. N. R. Khalid, A. Majid, M. B. Tahir, N. A. Niaz, and S. Khalid, "Carbonaceous-TiO_2 nanomaterials for photocatalytic degradation of pollutants: A review," *Ceramics International*, vol. 43, no.17, pp. 14552-14571, 2017.

17. E. Pližingrová, M. Klementová, P. Bezdička, J. Boháček, Z. Barbieriková, D. Dvoranová, M. Mazúr, J. Krýsa, J. Šubrt, and V. Brezová, "2D-Titanium dioxide nanosheets modified with Nd, Ag and Au: Preparation, characterization and photocatalytic activity," *Catalysis Today*, vol. 281, 165-180, 2017.

18. H. Hamad, M. Abd El-Latif, A. E.-H. Kashyout, W. Sadik, and M. Feteha, "Synthesis and characterization of core–shell–shell magnetic ($CoFe_2O_4$–SiO_2–TiO_2) nanocomposites and TiO_2 nanoparticles for the evaluation of photocatalytic activity under UV and visible irradiation," *New Journal of Chemistry*, vol. 39, no.4, pp. 3116-3128, 2015.

19. R. Acharya and K. Parida, "A review on TiO_2/g-C_3N_4 visible-light-responsive photocatalysts for sustainable energy generation and environmental remediation," *Journal of Environmental Chemical Engineering*, vol. 8, no.4, pp. 103896, 2020.

20. N. Madkhali, C. Prasad, K. Malkappa, H. Y. Choi, V. Govinda, I. Bahadur, and R. A. Abumousa, "Recent update on photocatalytic degradation of

pollutants in waste water using TiO_2-based heterostructured materials," *Results in Engineering*, vol. 17, 100920, 2023.

21. K. Pan, K. Shan, S. Wei, Y. Zhao, L. Xu, J. Zhu, and H.-H. Wu, "Two-step alcohothermal synthesis and characterization of enhanced visible-light-active WO_3-coated TiO_2 heterostructure," *Ceramics International*, vol. 46, no.2, pp. 2102-2109, 2020.

22. G. K. Upadhyay, J. K. Rajput, T. K. Pathak, V. Kumar, and L. P. Purohit, "Synthesis of ZnO:TiO_2 nanocomposites for photocatalyst application in visible light," *Vacuum*, vol. 160, 154-163, 2019.

23. S. Meng, W. Sun, S. Zhang, X. Zheng, X. Fu, and S. Chen, "Insight into the Transfer Mechanism of Photogenerated Carriers for WO_3/TiO_2 Heterojunction Photocatalysts: Is It the Transfer of Band–Band or Z-Scheme? Why?," *The Journal of Physical Chemistry C*, vol. 122, no.46, pp. 26326-26336, 2018.

24. C. R. Lhermitte and B. M. Bartlett, "Advancing the Chemistry of $CuWO_4$ for Photoelectrochemical Water Oxidation," *Accounts of Chemical Research*, vol. 49, no.6, pp. 1121-1129, 2016.

25. F. Ahmadi, M. Rahimi-Nasrabadi, and M. Eghbali-Arani, "The synthesize of $CuWO_4$ nano particles by a new morphological control method, characterization of its photocatalytic activity," *Journal of Materials Science: Materials in Electronics*, vol. 28, no.7, pp. 5244-5249, 2017.

26. A. E. B. Lima, M. J. S. Costa, R. S. Santos, N. C. Batista, L. S. Cavalcante, E. Longo, and G. E. Luz, "Facile preparation of $CuWO_4$ porous films and their photoelectrochemical properties," *Electrochimica Acta*, vol. 256, 139-145, 2017.

27. Q. Wang, Q. Xue, T. Chen, J. Li, Y. Liu, X. Shan, F. Liu, and J. Jia, "Recent advances in electrochemical sensors for antibiotics and their applications," *Chinese Chemical Letters*, vol. 32, no.2, pp. 609-619, 2021.

28. A. S. Ganie, S. Bano, S. Sultana, S. Sabir, and M. Z. Khan, "Ferrite nanocomposite based electrochemical sensor: characterization, voltammetric and amperometric studies for electrocatalytic detection of formaldehyde in aqueous media," *Electroanalysis*, vol. 33, no.1, pp. 233-248, 2021.

29. C. H. Lin, J. Rohilla, H. H. Kuo, C. Y. Chen, T. F. Mark Chang, M. Sone, P. P. Ingole, Y. C. Lo, and Y. J. Hsu, "Density-Functional Theory Studies on Photocatalysis and Photoelectrocatalysis: Challenges and Opportunities," *Solar RRL*, 2300948, 2024.

30. X. Wu, F. Kang, W. Duan, and J. Li, "Density functional theory calculations: A powerful tool to simulate and design high-performance

energy storage and conversion materials," *Progress in Natural Science: Materials International*, vol. 29, no.3, pp. 247-255, 2019.

31. A. K. Sharma, G. R. Nishad, P. K. Vishwakarma, and P. S. Jaget, Chapter 7 - Density functional theory (DFT)-based molecular modeling, in *Computational Modelling and Simulations for Designing of Corrosion Inhibitors*, D. K. Verma, C. Verma, and J. Aslam, Editors. Elsevier. pp. 115-133,2023.

32. J. H. Friedman, "Greedy function approximation: A Gradient boosting machine," *The Annals of Statistics*, vol. 29, no.5, pp. 1189-1232, 2001.

33. L. Prokhorenkova, G. Gusev, A. Vorobev, A. V. Dorogush, and A. Gulin, "CatBoost: unbiased boosting with categorical features," *Advances in neural information processing systems*, vol. 31, 2018.

34. G. Ke, Q. Meng, T. Finley, T. Wang, W. Chen, W. Ma, Q. Ye, and T.-Y. Liu, LightGBM: a highly efficient gradient boosting decision tree, in Proceedings of the 31st International Conference on Neural Information Processing Systems. Curran Associates Inc.: Long Beach, California, USA. pp. 3149–3157, 2017.

35. M. S. Alam, A. A. Akinpelu, M. K. Nazal, and S. M. Rahman, "Removal of N-nitrosodiphenylamine from contaminated water: A novel modeling framework using metaheuristic-based ensemble models," *Journal of Environmental Management*, vol. 365, 121503, 2024.

36. S. Manzetti and R. Ghisi, "The environmental release and fate of antibiotics," *Marine Pollution Bulletin*, vol. 79, no.1, pp. 7-15, 2014.

37. L. O. Omuferen, B. Maseko, and J. Olowoyo, "Occurrence of antibiotics in wastewater from hospital and convectional wastewater treatment plants and their impact on the effluent receiving rivers: current knowledge between 2010 and 2019," *Environmental Monitoring and Assessment*, vol. 194, no.4, pp. 306, 2022.

38. N. B. Alhaji, I. A. Odetokun, A. M. Adamu, A. Hassan, M. K. Lawan, and F. O. Fasina, "Antimicrobial usage and associated residues and resistance emergence in smallholder beef cattle production systems in Nigeria: A One Health challenge," *Veterinary Research Communications*, vol. 47, no.1, pp. 233-245, 2023.

39. O. Adebowale, 18 - Antimicrobial therapy and the risk for antimicrobial resistance in milk-borne diseases, in *The Microbiology, Pathogenesis and Zoonosis of Milk Borne Diseases*, T. Rana, Editor. Academic Press. pp. 333-356,2024.

40. M. J. Focazio, D. W. Kolpin, K. K. Barnes, E. T. Furlong, M. T. Meyer, S. D. Zaugg, L. B. Barber, and M. E. Thurman, "A national reconnaissance for pharmaceuticals and other organic wastewater contaminants in the

United States — II) Untreated drinking water sources," *Science of The Total Environment*, vol. 402, no.2, pp. 201-216, 2008.

41. M. Bilal, S. Mehmood, T. Rasheed, and H. M. N. Iqbal, "Antibiotics traces in the aquatic environment: persistence and adverse environmental impact," *Current Opinion in Environmental Science & Health*, vol. 13, 68-74, 2020.

42. Y. Ahmed, A. A. Siddiqua Maya, P. Akhtar, M. S. Alam, H. AlMohamadi, M. N. Islam, O. A. Alharbi, and S. M. Rahman, "A novel interpretable machine learning and metaheuristic-based protocol to predict and optimize ciprofloxacin antibiotic adsorption with nano-adsorbent," *Journal of Environmental Management*, vol. 370, 122614, 2024.

43. Y. Ahmed, M. M. Rahman, M. S. Alam, M. I. Miah, M. S. H. Choudhury, O. A. Alharbi, P. Akhtar, and S. M. Rahman, "Harnessing neural network model with optimization for enhanced ciprofloxacin antibiotic adsorption from contaminated water: A transparent and objective framework," *Journal of Water Process Engineering*, vol. 65, 105724, 2024.

44. J. Guo, Y. Wang, Y. Ahmed, M. Jin, and J. Li, Control strategies to combat dissemination of antibiotic resistance in urban water systems, in *Antibiotic Resistance in the Environment : A Worldwide Overview*, C. M. Manaia, E. Donner, I. Vaz-Moreira, and P. Hong, Editors. Springer International Publishing: Cham. pp. 147-187,2020.

45. Y. Ahmed, J. Zhong, Z. Wang, L. Wang, Z. Yuan, and J. Guo, "Simultaneous removal of antibiotic resistant bacteria, antibiotic resistance genes, and micropollutants by FeS_2@GO-based heterogeneous photo-Fenton process," *Environmental Science & Technology*, vol. 56, no.21, pp. 15156-15166, 2022.

46. Y. Ahmed, J. Zhong, Z. Yuan, and J. Guo, "Simultaneous removal of antibiotic resistant bacteria, antibiotic resistance genes, and micropollutants by a modified photo-Fenton process," *Water Research*, vol. 197, 117075, 2021.

47. Y. Ahmed, J. Lu, Z. Yuan, P. L. Bond, and J. Guo, "Efficient inactivation of antibiotic resistant bacteria and antibiotic resistance genes by photo-Fenton process under visible LED light and neutral pH," *Water Research*, vol. 179, 115878, 2020.

48. J. Zhong, Y. Ahmed, G. Carvalho, Z. Wang, L. Wang, J. F. Mueller, and J. Guo, "Simultaneous removal of micropollutants, antibiotic resistant bacteria, and antibiotic resistance genes using graphitic carbon nitride under simulated solar irradiation," *Chemical Engineering Journal*, vol. 433, 133839, 2022.

49. J. Zhong, Y. Ahmed, Z. Yu, J. F. Mueller, and J. Guo, "Synergistic combination of graphitic carbon nitride and peroxymonosulfate for efficient photocatalytic destruction of emerging contaminants under simulated solar irradiation," *ACS ES&T Water*, vol. 3, no.1, pp. 6-15, 2023.

50. Y. Ahmed, T. Akter, M. Prima, K. R. Dutta, S. Mukut, M. Ahsan, M. M. Rahman, P. Akhtar, and M. K. M. Z. Hyder, "Advanced ciprofloxacin quantification: A machine learning and metaheuristic approach using ultrasensitive chitosan-gold nanoparticle based electrochemical sensor," *Journal of Environmental Chemical Engineering*, 115094, 2024.

51. P. Dadgostar, "Antimicrobial resistance: implications and costs," *Infection and drug resistance*, 3903-3910, 2019.

52. K. Kümmerer, "Antibiotics in the aquatic environment – A review – Part II," *Chemosphere*, vol. 75, no.4, pp. 435-441, 2009.

53. P. Akhtar, Y. Ahmed, F. Islam, K. Alam, M. Mary, M. Z. Islam, M. M. H. Bhuiyan, and Z. Yaakob, "Efficiency of effluent treatment plants and threat to human health and aquatic environment in Bangladesh," *Asian Journal of Chemistry*, vol. 28, no.1, pp. 60-68, 2016.

54. Y. Ahmed, J. Zhong, Z. Yuan, and J. Guo, "Roles of reactive oxygen species in antibiotic resistant bacteria inactivation and micropollutant degradation in Fenton and photo-Fenton processes," *Journal of Hazardous Materials*, vol. 430, 128408, 2022.

55. K.-J. Choi, S.-G. Kim, and S.-H. Kim, "Removal of antibiotics by coagulation and granular activated carbon filtration," *Journal of Hazardous Materials*, vol. 151, no.1, pp. 38-43, 2008.

56. Y.-M. Zhu, Y. Chen, H. Lu, K. Jin, Y. Lin, H. Ren, and K. Xu, "Simultaneous efficient removal of tetracycline and mitigation of antibiotic resistance genes enrichment by a modified activated sludge process with static magnetic field," *Water Research*, vol. 262, 122107, 2024.

57. Z. Lu, G. Liu, H. Xie, Y. Zhai, and X. Li, "Advances and solutions in biological treatment for antibiotic wastewater with resistance genes: A review," *Journal of Environmental Management*, vol. 368, 122115, 2024.

58. N. S. Mdluli, P. N. Nomngongo, and N. Mketo, The occurrence, effect and biodegradation of antibiotics using metallic biogenic nanomaterials in water, in *Biogenic Nanomaterials for Environmental Sustainability: Principles, Practices, and Opportunities*. Springer. pp. 473-495,2024.

59. S. Li, N. Hofstra, M. G. M. van de Schans, J. Yang, Y. Li, Q. Zhang, L. Ma, M. Strokal, C. Kroeze, X. Chen, X. Chen, and F. Zhang, "Riverine antibiotics from animal production and wastewater," *Environmental Science & Technology Letters*, vol. 10, no.11, pp. 1059-1067, 2023.

60. J. Jeong, W. Song, W. J. Cooper, J. Jung, and J. Greaves, "Degradation of tetracycline antibiotics: Mechanisms and kinetic studies for advanced oxidation/reduction processes," *Chemosphere*, vol. 78, no.5, pp. 533-540, 2010.

61. J. A. Garrido-Cardenas, B. Esteban-García, A. Agüera, J. A. Sánchez-Pérez, and F. Manzano-Agugliaro, "Wastewater teatment by advanced oxidation process and their worldwide research trends," *International Journal of Environmental Research and Public Health*, vol. 17, no.1, pp. 170, 2020.

62. S. S. Boxi and S. Paria, "Visible light induced enhanced photocatalytic degradation of organic pollutants in aqueous media using Ag doped hollow TiO_2 nanospheres," *RSC Advances*, vol. 5, no.47, pp. 37657-37668, 2015.

63. Z. Li, J. Wang, J. Chang, B. Fu, and H. Wang, "Insight into advanced oxidation processes for the degradation of fluoroquinolone antibiotics: Removal, mechanism, and influencing factors," *Science of The Total Environment*, vol. 857, 159172, 2023.

64. X. Wang, J. Jing, M. Zhou, and R. Dewil, "Recent advances in H_2O_2-based advanced oxidation processes for removal of antibiotics from wastewater," *Chinese Chemical Letters*, vol. 34, no.3, pp. 107621, 2023.

65. Z. Honarmandrad, X. Sun, Z. Wang, M. Naushad, and G. Boczkaj, "Activated persulfate and peroxymonosulfate based advanced oxidation processes (AOPs) for antibiotics degradation – A review," *Water Resources and Industry*, vol. 29, 100194, 2023.

66. Y. Ahmed, A. A. S. Maya, P. Akhtar, H. AlMohamadi, A. W. Mohammad, S. M. Ashekuzzaman, A. I. Olbert, and M. G. Uddin, "Advancements and challenges in Fenton-based advanced oxidation processes for antibiotic removal in wastewater: From the laboratory to practical applications," *Journal of Environmental Chemical Engineering*, 115068, 2024.

67. Y. Zhang, Y.-G. Zhao, F. Maqbool, and Y. Hu, "Removal of antibiotics pollutants in wastewater by UV-based advanced oxidation processes: Influence of water matrix components, processes optimization and application: A review," *Journal of Water Process Engineering*, vol. 45, 102496, 2022.

68. Z. Lu, Y. Ling, W. Sun, C. Liu, T. Mao, X. Ao, and T. Huang, "Antibiotics degradation by UV/chlor (am) ine advanced oxidation processes: A comprehensive review," *Environmental Pollution*, vol. 308, 119673, 2022.

69. A. J. dos Santos, M. S. Kronka, G. V. Fortunato, and M. R. V. Lanza, "Recent advances in electrochemical water technologies for the treatment of

antibiotics: A short review," *Current Opinion in Electrochemistry*, vol. 26, 100674, 2021.

70. X. Bai, W. Chen, B. Wang, T. Sun, B. Wu, and Y. Wang, "Photocatalytic degradation of some typical antibiotics: Recent advances and future outlooks," *International Journal of Molecular Sciences*, vol. 23, no.15, pp. 8130, 2022.

71. X. Wang, R. Yin, L. Zeng, and M. Zhu, "A review of graphene-based nanomaterials for removal of antibiotics from aqueous environments," *Environmental Pollution*, vol. 253, 100-110, 2019.

72. M.-f. Li, Y.-g. Liu, G.-m. Zeng, N. Liu, and S.-b. Liu, "Graphene and graphene-based nanocomposites used for antibiotics removal in water treatment: A review," *Chemosphere*, vol. 226, 360-380, 2019.

73. H. Zeng, J. Li, W. Zhao, J. Xu, H. Xu, D. Li, and J. Zhang, "The current status and prevention of antibiotic pollution in groundwater in China," *International Journal of Environmental Research and Public Health*, vol. 19, no.18, pp. 11256, 2022.

74. J. A. Galarza, L. Murphy, and J. Mappes, "Antibiotics accelerate growth at the expense of immunity," *Proceedings of the Royal Society B*, vol. 288, no.1961, pp. 20211819, 2021.

75. K. C. Leung, Q. Huang, S. St-Hilaire, H. Liu, X. Zheng, K. B. Cheung, and I. M. Zwetsloot, "Fraudulent antibiotic products on the market for aquaculture use," *Preventive Veterinary Medicine*, vol. 181, 105052, 2020.

76. K. Wang, T. Zhuang, Z. Su, M. Chi, and H. Wang, "Antibiotic residues in wastewaters from sewage treatment plants and pharmaceutical industries: Occurrence, removal and environmental impacts," *Science of The Total Environment*, vol. 788, 147811, 2021.

77. S. I. Polianciuc, A. E. Gurzău, B. Kiss, M. G. Ştefan, and F. Loghin, "Antibiotics in the environment: causes and consequences," *Medicine and pharmacy reports*, vol. 93, no.3, pp. 231, 2020.

78. R. Wang, M. Ji, H. Zhai, Y. Guo, and Y. Liu, "Occurrence of antibiotics and antibiotic resistance genes in WWTP effluent-receiving water bodies and reclaimed wastewater treatment plants," *Science of The Total Environment*, vol. 796, 148919, 2021.

79. J. Xue, D. Lei, X. Zhao, Y. Hu, S. Yao, K. Lin, Z. Wang, and C. Cui, "Antibiotic residue and toxicity assessment of wastewater during the pharmaceutical production processes," *Chemosphere*, vol. 291, 132837, 2022.

80. N. Hassoun-Kheir, Y. Stabholz, J.-U. Kreft, R. de la Cruz, J. L. Romalde, J. Nesme, S. J. Sørensen, B. F. Smets, D. Graham, and M. Paul, "Comparison

of antibiotic-resistant bacteria and antibiotic resistance genes abundance in hospital and community wastewater: A systematic review," *Science of The Total Environment*, vol. 743, 140804, 2020.

81. C. Bhagat, M. Kumar, V. K. Tyagi, and P. K. Mohapatra, "Proclivities for prevalence and treatment of antibiotics in the ambient water: a review," *npj Clean Water*, vol. 3, no.1, pp. 42, 2020.

82. D. Fatta-Kassinos, M. I. Vasquez, and K. Kümmerer, "Transformation products of pharmaceuticals in surface waters and wastewater formed during photolysis and advanced oxidation processes–degradation, elucidation of byproducts and assessment of their biological potency," *Chemosphere*, vol. 85, no.5, pp. 693-709, 2011.

83. M. Corredor and A. Muñoz-Gómez, Pharmaceutical antibiotics at a significant level in nature: From hospitals, livestock, and plants to soil, water, and sea. Emerging Contaminants. 2021.

84. A. Singh and S. Saluja, Microbial Degradation of Antibiotics from Effluents, in *Recent Advances in Microbial Degradation*, Inamuddin, M. I. Ahamed, and R. Prasad, Editors. Springer Singapore: Singapore. pp. 389-404,2021.

85. P. Chaturvedi, P. Shukla, B. S. Giri, P. Chowdhary, R. Chandra, P. Gupta, and A. Pandey, "Prevalence and hazardous impact of pharmaceutical and personal care products and antibiotics in environment: A review on emerging contaminants," *Environmental Research*, vol. 194, 110664, 2021.

86. R. Lulijwa, E. J. Rupia, and A. C. Alfaro, "Antibiotic use in aquaculture, policies and regulation, health and environmental risks: a review of the top 15 major producers," *Reviews in Aquaculture*, vol. 12, no.2, pp. 640-663, 2020.

87. A. Krishnan, A. Swarnalal, D. Das, M. Krishnan, V. S. Saji, and S. M. A. Shibli, "A review on transition metal oxides based photocatalysts for degradation of synthetic organic pollutants," *Journal of Environmental Sciences*, vol. 139, 389-417, 2024.

88. A. Kaur, B. Bajaj, A. Kaushik, A. Saini, and D. Sud, "A review on template assisted synthesis of multi-functional metal oxide nanostructures: Status and prospects," *Materials Science and Engineering: B*, vol. 286, 116005, 2022.

89. K. Qin, Q. Zhao, H. Yu, X. Xia, J. Li, S. He, L. Wei, and T. An, "A review of bismuth-based photocatalysts for antibiotic degradation: Insight into the photocatalytic degradation performance, pathways and relevant mechanisms," *Environmental Research*, vol. 199, 111360, 2021.

90. T. Velempini, E. Prabakaran, and K. Pillay, "Recent developments in the use of metal oxides for photocatalytic degradation of pharmaceutical

pollutants in water—a review," *Materials Today Chemistry*, vol. 19, 100380, 2021.

91. A. M. El-Khawaga, A. Zidan, and A. I. A. A. El-Mageed, "Preparation methods of different nanomaterials for various potential applications: A review," *Journal of Molecular Structure*, vol. 1281, 135148, 2023.

92. T. Suwannaruang, P. Kidkhunthod, T. Butburee, H. P. Shivaraju, B. Shahmoradi, and K. Wantala, "Facile synthesis of cooperative mesoporous-assembled $Ce_xSr_{1-x}Fe_xTi_{1-x}O_3$ perovskite catalysts for enhancement beta-lactam antibiotic photodegradation under visible light irradiation," *Surfaces and Interfaces*, vol. 23, 101013, 2021.

93. Z. Zhao, J. Fan, X. Deng, and J. Liu, "One-step synthesis of phosphorus-doped g-C_3N_4/Co_3O_4 quantum dots from vitamin B_{12} with enhanced visible-light photocatalytic activity for metronidazole degradation," *Chemical Engineering Journal*, vol. 360, 1517-1529, 2019.

94. G. Li, R. Wang, B. Wang, and J. Zhang, "Sm-doped mesoporous g-C_3N_4 as efficient catalyst for degradation of tylosin: Influencing factors and toxicity assessment," *Applied Surface Science*, vol. 517, 146212, 2020.

95. J.-H. Shen, Y.-H. Tang, Z.-W. Jiang, D.-Q. Liao, and J.-J. Horng, "Optimized preparation and characterization of Co-N codoped TiO_2 with enhanced visible light activity: An insight into effect of dopants on surface redox reactions of photogenerated charge carriers for hydroxyl radical formation," *Journal of Alloys and Compounds*, vol. 862, 158697, 2021.

96. M. S. Rahman, M. A. H. Suvo, M. M. T. Islam, A. R. Noor, N. Yeachin, and M. A. Bhuiyan, "Fast and efficient removal of metronidazole from aqueous solution using graphene oxide (GO) supported nitrogen (N) doped zinc oxide (ZnO) nanoparticles," *Colloids and Surfaces A: Physicochemical and Engineering Aspects*, vol. 690, 133660, 2024.

97. T.-B. Nguyen, C. P. Huang, R.-a. Doong, C.-W. Chen, and C.-D. Dong, "Visible-light photodegradation of sulfamethoxazole (SMX) over Ag-P-codoped g-C_3N_4 (Ag-P@UCN) photocatalyst in water," *Chemical Engineering Journal*, vol. 384, 123383, 2020.

98. X. Huang, W. Yang, G. Zhang, L. Yan, Y. Zhang, A. Jiang, H. Xu, M. Zhou, Z. Liu, H. Tang, and D. D. Dionysiou, "Alternative synthesis of nitrogen and carbon co-doped TiO_2 for removing fluoroquinolone antibiotics in water under visible light," *Catalysis Today*, vol. 361, 11-16, 2021.

99. R. Kumar, A. Sudhaik, Sonu, V.-H. Nguyen, Q. Van Le, T. Ahamad, S. Thakur, N. Kumar, C. M. Hussain, P. Singh, and P. Raizada, "Graphene oxide modified K, P co-doped g-C_3N_4 and $CoFe_2O_4$ composite for

photocatalytic degradation of antibiotics," *Journal of the Taiwan Institute of Chemical Engineers*, vol. 150, 105077, 2023.

100. D. Chen, Y. Cheng, N. Zhou, P. Chen, Y. Wang, K. Li, S. Huo, P. Cheng, P. Peng, R. Zhang, L. Wang, H. Liu, Y. Liu, and R. Ruan, "Photocatalytic degradation of organic pollutants using TiO_2-based photocatalysts: A review," *Journal of Cleaner Production*, vol. 268, 121725, 2020.

101. W. Yu, J. Zhang, and T. Peng, "New insight into the enhanced photocatalytic activity of N-, C- and S-doped ZnO photocatalysts," *Applied Catalysis B: Environmental*, vol. 181, 220-227, 2016.

102. Y. Ren, D. Zeng, and W.-J. Ong, "Interfacial engineering of graphitic carbon nitride (g-C_3N_4)-based metal sulfide heterojunction photocatalysts for energy conversion: A review," *Chinese Journal of Catalysis*, vol. 40, no.3, pp. 289-319, 2019.

103. T. D. Nguyen, T. Lee, T. Van Tran, V. H. Nguyen, L. X. Nong, L. G. Bach, and D.-V. N. Vo, "Multicomponent photocatalysts for synergic removal of antibiotics in aqueous media: a review," *Environmental Chemistry Letters*, vol. 21, no.2, pp. 935-980, 2023.

104. K. Wu, Z. Qin, X. Zhang, R. Guo, X. Ren, and X. Pu, "Z-scheme BiOCl/Bi–Bi_2O_3 heterojunction with oxygen vacancy for excellent degradation performance of antibiotics and dyes," *Journal of Materials Science*, vol. 55, no.9, pp. 4017-4029, 2020.

105. K. Wang, G. Zhang, J. Li, Y. Li, and X. Wu, "0D/2D Z-scheme heterojunctions of bismuth tantalate quantum dots/ultrathin g-C_3N_4 nanosheets for highly efficient visible light photocatalytic degradation of antibiotics," *ACS Applied Materials & Interfaces*, vol. 9, no.50, pp. 43704-43715, 2017.

106. M. Ren, Y. Ao, P. Wang, and C. Wang, "Construction of silver/graphitic-C_3N_4/bismuth tantalate Z-scheme photocatalyst with enhanced visible-light-driven performance for sulfamethoxazole degradation," *Chemical Engineering Journal*, vol. 378, 122122, 2019.

107. K. Rasouli, A. Alamdari, and S. Sabbaghi, "Ultrasonic-assisted synthesis of α-Fe_2O_3@TiO_2 photocatalyst: Optimization of effective factors in the fabrication of photocatalyst and removal of non-biodegradable cefixime via response surface methodology-central composite design," *Separation and Purification Technology*, vol. 307, 122799, 2023.

108. Y. M. Hunge, A. A. Yadav, S.-W. Kang, S. Jun Lim, and H. Kim, "Visible light activated MoS_2/ZnO composites for photocatalytic degradation of ciprofloxacin antibiotic and hydrogen production," *Journal of Photochemistry and Photobiology A: Chemistry*, vol. 434, 114250, 2023.

109. B. Gao, S. Dong, J. Liu, L. Liu, Q. Feng, N. Tan, T. Liu, L. Bo, and L. Wang, "Identification of intermediates and transformation pathways derived from photocatalytic degradation of five antibiotics on $ZnIn_2S_4$," *Chemical Engineering Journal*, vol. 304, 826-840, 2016.

110. L. Chen, W. Ma, J. Dai, J. Zhao, C. Li, and Y. Yan, "Facile synthesis of highly efficient graphitic-C_3N_4/$ZnFe_2O_4$ heterostructures enhanced visible-light photocatalysis for spiramycin degradation," *Journal of Photochemistry and Photobiology A: Chemistry*, vol. 328, 24-32, 2016.

111. R. M. Mohamed, A. A. Ismail, and M. Alhaddad, "A novel design of porous Cr_2O_3@ZnO nanocomposites as highly efficient photocatalyst toward degradation of antibiotics: A case study of ciprofloxacin," *Separation and Purification Technology*, vol. 266, 118588, 2021.

112. L. Hu, M. Xing, X. He, K. Yang, J. Zhu, J. Wang, J. He, and J. Shi, "Photocatalytic degradation of tetracycline hydrochloride by ZnO/TiO_2 composite photocatalyst," *Journal of Materials Science: Materials in Electronics*, vol. 34, no.36, pp. 2273, 2023.

113. S. Yu, J. Zhou, Y. Ren, Z. Yang, M. Zhong, X. Feng, B. Su, and Z. Lei, "Excellent adsorptive-photocatalytic performance of zinc oxide and biomass derived N, O-contained biochar nanocomposites for dyes and antibiotic removal," *Chemical Engineering Journal*, vol. 451, 138959, 2023.

114. N. Roy, K. Kannabiran, and A. Mukherjee, "Integrated adsorption and photocatalytic degradation based removal of ciprofloxacin and sulfamethoxazole antibiotics using Fc@rGO-ZnO nanocomposite in aqueous systems," *Chemosphere*, vol. 333, 138912, 2023.

115. T. Senasu, T. Narenuch, K. Wannakam, T. Chankhanittha, and S. Nanan, "Solvothermally grown BiOCl catalyst for photodegradation of cationic dye and fluoroquinolone-based antibiotics," *Journal of Materials Science: Materials in Electronics*, vol. 31, 9685-9694, 2020.

116. G. Wang, S. Zhang, H. Lu, C. Lu, M. Yang, K. Tang, and A. Tang, "Montmorillonite helps BiOCl photodegradation of antibiotics," *Environmental Science: Nano*, vol. 10, no.12, pp. 3423-3438, 2023.

117. V. Subhiksha, S. Kokilavani, and S. Sudheer Khan, "Recent advances in degradation of organic pollutant in aqueous solutions using bismuth based photocatalysts: A review," *Chemosphere*, vol. 290, 133228, 2022.

118. L. Chen, Y. Li, J. Zhang, M. Li, W. Yin, and X. Chen, "Oxidative degradation of tetracycline hydrochloride by Mn_2O_3/Bi_2O_3 photocatalysis activated peroxymonosulfate," *Inorganic Chemistry Communications*, vol. 140, 109414, 2022.

119. A. Ren, C. Liu, Y. Hong, W. Shi, S. Lin, and P. Li, "Enhanced visible-light-driven photocatalytic activity for antibiotic degradation using magnetic $NiFe_2O_4/Bi_2O_3$ heterostructures," *Chemical Engineering Journal*, vol. 258, 301-308, 2014.

120. Y. Zhu, J. Xue, T. Xu, G. He, and H. Chen, "Enhanced photocatalytic activity of magnetic core–shell Fe_3O_4@ Bi_2O_3–RGO heterojunctions for quinolone antibiotics degradation under visible light," *Journal of Materials Science: Materials in Electronics*, vol. 28, 8519-8528, 2017.

121. M. Chen, J. Yao, Y. Huang, H. Gong, and W. Chu, "Enhanced photocatalytic degradation of ciprofloxacin over $Bi_2O_3/(BiO)_2CO_3$ heterojunctions: Efficiency, kinetics, pathways, mechanisms and toxicity evaluation," *Chemical Engineering Journal*, vol. 334, 453-461, 2018.

122. V. Thakur, S. Singh, P. Kumar, S. Rawat, V. Chandra Srivastava, S.-L. Lo, and U. Lavrenčič Štangar, "Photocatalytic behaviors of bismuth-based mixed oxides: Types, fabrication techniques and mineralization mechanism of antibiotics," *Chemical Engineering Journal*, vol. 475, 146100, 2023.

123. M. Wang, G. Lu, R. Jiang, T. Dang, and J. Liu, "Degradation and detoxification of broad-spectrum antibiotics by small molecular intercalated BiOCl under visible light," *Journal of Colloid and Interface Science*, vol. 622, 995-1007, 2022.

124. R. Hao, X. Xiao, X. Zuo, J. Nan, and W. Zhang, "Efficient adsorption and visible-light photocatalytic degradation of tetracycline hydrochloride using mesoporous BiOI microspheres," *Journal of Hazardous Materials*, vol. 209-210, 137-145, 2012.

125. Q. He, M. Ge, and Q. Yu, "Synergistic degradation of tetracycline by BiOBr microspheres combined with peroxydisulfate under visible LED light irradiation," *Journal of Chemical Sciences*, vol. 133, 1-14, 2021.

126. F. Chen, H. Huang, L. Guo, Y. Zhang, and T. Ma, "The role of polarization in photocatalysis," *Angewandte Chemie International Edition*, vol. 58, no.30, pp. 10061-10073, 2019.

127. L. Yang, J. Wang, Y. Zhang, B. Zhou, P. Tan, and J. Pan, "Construction of S-scheme BiOCl/CdS composite for enhanced photocatalytic degradation of antibiotic," *Journal of Materials Science: Materials in Electronics*, vol. 33, no.16, pp. 13303-13315, 2022.

128. R. Koutavarapu, W. Y. Jang, M. C. Rao, M. Arumugam, and J. Shim, "Novel $BiVO_4$-nanosheet-supported MoS_2-nanoflake-heterostructure with synergistic enhanced photocatalytic removal of tetracycline under visible light irradiation," *Chemosphere*, vol. 305, 135465, 2022.

129. T. Wang, H. Shi, A. Kumar, D. Zhang, H. Wang, S. Wang, and J. Zheng, "Efficient visible-light photocatalysis of chloramphenicol using novel engineered biochar-based Ti-doped Bi_2WO_6 composite: Mechanisms, degradation pathways, and applications," *Separation and Purification Technology*, vol. 332, 125780, 2024.

130. F. Zhu, Y. Lv, J. Li, J. Ding, X. Xia, L. Wei, J. Jiang, G. Zhang, and Q. Zhao, "Enhanced visible light photocatalytic performance with metal-doped Bi_2WO_6 for typical fluoroquinolones degradation: Efficiencies, pathways and mechanisms," *Chemosphere*, vol. 252, 126577, 2020.

131. R. Huang, J. Wu, M. Zhang, B. Liu, Z. Zheng, and D. Luo, "Strategies to enhance photocatalytic activity of graphite carbon nitride-based photocatalysts," *Materials & Design*, vol. 210, 110040, 2021.

132. A. Balakrishnan and M. Chinthala, "Comprehensive review on advanced reusability of g-C_3N_4 based photocatalysts for the removal of organic pollutants," *Chemosphere*, vol. 297, 134190, 2022.

133. J. Chen, Z. Yan, Y. Chen, K. Yao, and Z. Xu, "Enhanced solar-induced photocatalytic removal of antibiotics over molecularly reconstituted graphitic carbon nitride," *Applied Surface Science*, vol. 634, 157637, 2023.

134. Q. Li, N. Wen, W. Zhang, L. Yu, J. Shen, S. Li, and Y. Lv, "Preparation of g-C_3N_4/TCNQ composite and photocatalytic degradation of pefloxacin," *Micromachines*, vol. 14, no.5, pp. 941, 2023.

135. X. Zhan, Y. Zhao, Y. Sun, C. Lei, H. Wang, and H. Shi, "Pyridazine doped g-C_3N_4 with nitrogen defects and spongy structure for efficient tetracycline photodegradation and photocatalytic H_2 evolution," *Chemosphere*, vol. 307, 136087, 2022.

136. J. Xing, N. Wang, X. Li, J. Wang, M. Taiwaikuli, X. Huang, T. Wang, L. Zhou, and H. Hao, "Synthesis and modifications of g-C_3N_4-based materials and their applications in wastewater pollutants removal," *Journal of Environmental Chemical Engineering*, vol. 10, no.6, pp. 108782, 2022.

137. X. Wang, P. Zhang, L. Li, N. Li, X. Su, X. Wei, and L. Han, "Preparation of a high-performance N-defect ZnO@g-C_3N_4 nanocomposite and its photocatalytic degradation of tetracycline," *Materials Today Communications*, vol. 36, 106732, 2023.

138. G. Li, B. Wang, J. Zhang, R. Wang, and H. Liu, "Rational construction of a direct Z-scheme g-C_3N_4/CdS photocatalyst with enhanced visible light photocatalytic activity and degradation of erythromycin and tetracycline," *Applied Surface Science*, vol. 478, 1056-1064, 2019.

139. J. Niu, Y. Xie, H. Luo, Q. Wang, Y. Zhang, and Y. Wang, "Cobalt oxide loaded graphitic carbon nitride as adsorptive photocatalyst for

tetracycline removal from aqueous solution," *Chemosphere*, vol. 218, 169-178, 2019.

140. H.-Y. Liu, C. Liang, C.-G. Niu, D.-W. Huang, Y.-B. Du, H. Guo, L. Zhang, Y.-Y. Yang, and G.-M. Zeng, "Facile assembly of g-C_3N_4/Ag_2CO_3/graphene oxide with a novel dual Z-scheme system for enhanced photocatalytic pollutant degradation," *Applied Surface Science*, vol. 475, 421-434, 2019.

141. M. F. R. Samsudin, C. Frebillot, Y. Kaddoury, S. Sufian, and W.-J. Ong, "Bifunctional Z-Scheme Ag/$AgVO_3$/g-C_3N_4 photocatalysts for expired ciprofloxacin degradation and hydrogen production from natural rainwater without using scavengers," *Journal of Environmental Management*, vol. 270, 110803, 2020.

142. A. Sanei, K. Dashtian, J. Yousefi Seyf, F. Seidi, and E. Kolvari, "Biomass derived reduced-graphene-oxide supported α-Fe_2O_3/ZnO S-scheme heterostructure: Robust photocatalytic wastewater remediation," *Journal of Environmental Management*, vol. 332, 117377, 2023.

143. Y. Li, Z. Lai, Z. Huang, H. Wang, C. Zhao, G. Ruan, and F. Du, "Fabrication of BiOBr/MoS_2/graphene oxide composites for efficient adsorption and photocatalytic removal of tetracycline antibiotics," *Applied Surface Science*, vol. 550, 149342, 2021.

144. P. Karaolia, I. Michael-Kordatou, E. Hapeshi, C. Drosou, Y. Bertakis, D. Christofilos, G. S. Armatas, L. Sygellou, T. Schwartz, N. P. Xekoukoulotakis, and D. Fatta-Kassinos, "Removal of antibiotics, antibiotic-resistant bacteria and their associated genes by graphene-based TiO_2 composite photocatalysts under solar radiation in urban wastewaters," *Applied Catalysis B: Environmental*, vol. 224, 810-824, 2018.

145. S. Naraginti, Y.-Y. Yu, Z. Fang, and Y.-C. Yong, "Novel tetrahedral Ag_3PO_4@N-rGO for photocatalytic detoxification of sulfamethoxazole: Process optimization, transformation pathways and biotoxicity assessment," *Chemical Engineering Journal*, vol. 375, 122035, 2019.

146. T. T. Nguyen, S.-N. Nam, J. Son, and J. Oh, "Tungsten trioxide (WO_3)-assisted photocatalytic degradation of amoxicillin by simulated solar irradiation," *Scientific reports*, vol. 9, no.1, pp. 9349, 2019.

147. W. Zhu, F. Sun, R. Goei, and Y. Zhou, "Construction of WO_3–gC_3N_4 composites as efficient photocatalysts for pharmaceutical degradation under visible light," *Catalysis Science & Technology*, vol. 7, no.12, pp. 2591-2600, 2017.

148. W. Zhu, F. Sun, R. Goei, and Y. Zhou, "Facile fabrication of RGO-WO_3 composites for effective visible light photocatalytic degradation of

sulfamethoxazole," *Applied Catalysis B: Environmental*, vol. 207, 93-102, 2017.

149. M. Yan, Y. Wu, F. Zhu, Y. Hua, and W. Shi, "The fabrication of a novel Ag_3VO_4/WO_3 heterojunction with enhanced visible light efficiency in the photocatalytic degradation of TC," *Physical Chemistry Chemical Physics*, vol. 18, no.4, pp. 3308-3315, 2016.

150. W. Zhu, Z. Li, C. He, S. Faqian, and Y. Zhou, "Enhanced photodegradation of sulfamethoxazole by a novel WO_3-CNT composite under visible light irradiation," *Journal of Alloys and Compounds*, vol. 754, 153-162, 2018.

151. T. Wang, W. Quan, D. Jiang, L. Chen, D. Li, S. Meng, and M. Chen, "Synthesis of redox-mediator-free direct Z-scheme AgI/WO_3 nanocomposite photocatalysts for the degradation of tetracycline with enhanced photocatalytic activity," *Chemical Engineering Journal*, vol. 300, 280-290, 2016.

152. L. Zhou, W. Zhang, L. Chen, H. Deng, and J. Wan, "A novel ternary visible-light-driven photocatalyst $AgCl/Ag_3PO_4/g\text{-}C_3N_4$: Synthesis, characterization, photocatalytic activity for antibiotic degradation and mechanism analysis," *Catalysis Communications*, vol. 100, 191-195, 2017.

153. H. Zhang, Z. Wang, R. Li, J. Guo, Y. Li, J. Zhu, and X. Xie, "TiO_2 supported on reed straw biochar as an adsorptive and photocatalytic composite for the efficient degradation of sulfamethoxazole in aqueous matrices," *Chemosphere*, vol. 185, 351-360, 2017.

154. X. Xie, S. Li, H. Zhang, Z. Wang, and H. Huang, "Promoting charge separation of biochar-based $Zn\text{-}TiO_2$/pBC in the presence of ZnO for efficient sulfamethoxazole photodegradation under visible light irradiation," *Science of The Total Environment*, vol. 659, 529-539, 2019.

155. M. Jahdi, S. B. Mishra, E. N. Nxumalo, S. D. Mhlanga, and A. K. Mishra, "Smart pathways for the photocatalytic degradation of sulfamethoxazole drug using F-Pd co-doped TiO_2 nanocomposites," *Applied Catalysis B: Environmental*, vol. 267, 118716, 2020.

156. M. Sarafraz, M. Sadeghi, A. Yazdanbakhsh, M. M. Amini, M. Sadani, and A. Eslami, "Enhanced photocatalytic degradation of ciprofloxacin by black $Ti^{3+}/N\text{-}TiO_2$ under visible LED light irradiation: Kinetic, energy consumption, degradation pathway, and toxicity assessment," *Process Safety and Environmental Protection*, vol. 137, 261-272, 2020.

157. X. Chen, X. Peng, L. Jiang, X. Yuan, J. Fei, and W. Zhang, "Photocatalytic removal of antibiotics by MOF-derived Ti^{3+}- and oxygen vacancy-doped anatase/rutile TiO_2 distributed in a carbon matrix," *Chemical Engineering Journal*, vol. 427, 130945, 2022.

158. M. Abdullah, J. Iqbal, M. S. Ur Rehman, U. Khalid, F. Mateen, S. N. Arshad, A. G. Al-Sehemi, H. Algarni, O. A. Al-Hartomy, and T. Fazal, "Removal of ceftriaxone sodium antibiotic from pharmaceutical wastewater using an activated carbon based TiO_2 composite: Adsorption and photocatalytic degradation evaluation," *Chemosphere*, vol. 317, 137834, 2023.

159. S. Sukidpaneenid, C. Chawengkijwanich, C. Pokhum, T. Isobe, P. Opaprakasit, and P. Sreearunothai, "Multi-function adsorbent-photocatalyst MXene-TiO_2 composites for removal of enrofloxacin antibiotic from water," *Journal of Environmental Sciences*, vol. 124, 414-428, 2023.

160. J. S. Jeyaprakash, M. Rajamani, P. Mani, C. Yazhini, S. H. Sonawane, and B. Neppolian, "Highly efficient ultrasound-driven Ti^{3+}-doped TiO_2 with oxygen vacancies: A promising visible-light catalyst for complete sonophotocatalytic degradation of tetracycline," *Industrial & Engineering Chemistry Research*, 2024.

161. C. Chen, H. Zeng, M. Yi, G. Xiao, S. Xu, S. Shen, and B. Feng, "In-situ growth of Ag_3PO_4 on calcined Zn-Al layered double hydroxides for enhanced photocatalytic degradation of tetracycline under simulated solar light irradiation and toxicity assessment," *Applied Catalysis B: Environmental*, vol. 252, 47-54, 2019.

162. S. Dong, L. Cui, W. Zhang, L. Xia, S. Zhou, C. K. Russell, M. Fan, J. Feng, and J. Sun, "Double-shelled $ZnSnO_3$ hollow cubes for efficient photocatalytic degradation of antibiotic wastewater," *Chemical Engineering Journal*, vol. 384, 123279, 2020.

163. Z. Jia, T. Li, Z. Zheng, J. Zhang, J. Liu, R. Li, Y. Wang, X. Zhang, Y. Wang, and C. Fan, "The BiOCl/diatomite composites for rapid photocatalytic degradation of ciprofloxacin: Efficiency, toxicity evaluation, mechanisms and pathways," *Chemical Engineering Journal*, vol. 380, 122422, 2020.

164. S. Wu, Y. Su, Y. Zhu, Y. Zhang, and M. Zhu, "In-situ growing Bi/BiOCl microspheres on Ti_3C_2 nanosheets for upgrading visible-light-driven photocatalytic activity," *Applied Surface Science*, vol. 520, 146339, 2020.

165. T. Senasu, N. Lorwanishpaisarn, K. Hemavibool, S. Nijpanich, N. Chanlek, and S. Nanan, "Construction of g-C_3N_4/BiOCl/CdS heterostructure photocatalyst for complete removal of oxytetracycline antibiotic in wastewater," *Separation and Purification Technology*, vol. 306, 122735, 2023.

166. X. Ma, K. Chen, B. Niu, Y. Li, L. Wang, J. Huang, H. She, and Q. Wang, "Preparation of $BiOCl_{0.9}I_{0.1}$/β-Bi_2O_3 composite for degradation of tetracycline hydrochloride under simulated sunlight," *Chinese Journal of Catalysis*, vol. 41, no.10, pp. 1535-1543, 2020.

167. W. Wang, Q. Han, Z. Zhu, L. Zhang, S. Zhong, and B. Liu, "Enhanced photocatalytic degradation performance of organic contaminants by heterojunction photocatalyst $BiVO_4/TiO_2$/RGO and its compatibility on four different tetracycline antibiotics," *Advanced Powder Technology*, vol. 30, no.9, pp. 1882-1896, 2019.

168. X. Zheng, Y. Li, H. Peng, Z. Huang, H. Wang, and J. Wen, "Efficient solar-light photodegradation of tetracycline hydrochloride using $BiVO_4/MoO_3$ composites," *Colloids and Surfaces A: Physicochemical and Engineering Aspects*, vol. 621, 126599, 2021.

169. N. T. Dieu Cam, H.-D. Pham, T.-D. Pham, T. T. Thu Phuong, C. Van Hoang, M. H. Thanh Tung, N. T. Trung, N. T. Huong, and T. T. Thu Hien, "Novel photocatalytic performance of magnetically recoverable $MnFe_2O_4/BiVO_4$ for polluted antibiotics degradation," *Ceramics International*, vol. 47, no.2, pp. 1686-1692, 2021.

170. H. B. Truong, B. T. Huy, S. K. Ray, G. Gyawali, Y.-I. Lee, J. Cho, and J. Hur, "Magnetic visible-light activated photocatalyst $ZnFe_2O_4/BiVO_4$/g-C_3N_4 for decomposition of antibiotic lomefloxacin: Photocatalytic mechanism, degradation pathway, and toxicity assessment," *Chemosphere*, vol. 299, 134320, 2022.

171. Q. Yang, G. Tan, L. Yin, W. Liu, B. Zhang, S. Feng, Y. Bi, Y. Liu, T. Liu, Z. Wang, H. Ren, and A. Xia, "Full-spectrum broad-spectrum degradation of antibiotics by $BiVO_4$@BiOCl crystal plane S-type and Z-type heterojunctions," *Chemical Engineering Journal*, vol. 467, 143450, 2023.

172. X. Yuan, D. Shen, Q. Zhang, H. Zou, Z. Liu, and F. Peng, "Z-scheme $Bi_2WO_6/CuBi_2O_4$ heterojunction mediated by interfacial electric field for efficient visible-light photocatalytic degradation of tetracycline," *Chemical Engineering Journal*, vol. 369, 292-301, 2019.

173. Z. Zhu, C. Wang, L. Liang, D. Yu, J. Sun, L. Zhang, S. Zhong, and B. Liu, "Synthesis of novel ternary photocatalyst Ag_3PO_4/Bi_2WO_6/multi-walled carbon nanotubes and its enhanced visible-light photoactivity for photodegradation of norfloxacin," *Journal of Nanoscience and Nanotechnology*, vol. 20, no.4, pp. 2247-2258, 2020.

174. J. Sun, C.-H. Shen, J. Guo, H. Guo, Y.-F. Yin, X.-J. Xu, Z.-H. Fei, Z.-T. Liu, and X.-J. Wen, "Highly efficient activation of peroxymonosulfate by Co_3O_4/Bi_2WO_6 p-n heterojunction composites for the degradation of ciprofloxacin under visible light irradiation," *Journal of Colloid and Interface Science*, vol. 588, 19-30, 2021.

175. Z. Chen, J. Liang, X. Xu, G. He, and H. Chen, "CdS–Bi_2MoO_6/RGO nanocomposites for efficient degradation of ciprofloxacin under visible light," *Journal of Materials Science*, vol. 55, no.14, pp. 6065-6077, 2020.

176. J. Guo, L. Wang, X. Wei, Z. A. Alothman, M. D. Albaqami, V. Malgras, Y. Yamauchi, Y. Kang, M. Wang, W. Guan, and X. Xu, "Direct Z-scheme $CuInS_2/Bi_2MoO_6$ heterostructure for enhanced photocatalytic degradation of tetracycline under visible light," *Journal of Hazardous Materials*, vol. 415, 125591, 2021.

177. W. Cao, C. Jiang, C. Chen, H. Zhou, and Y. Wang, "A novel Z-scheme $CdS/Bi_4O_5Br_2$ heterostructure with mechanism analysis: Enhanced photocatalytic performance," *Journal of Alloys and Compounds*, vol. 861, 158554, 2021.

178. T. Chankhanittha, V. Somaudon, T. Photiwat, S. Youngme, K. Hemavibool, and S. Nanan, "Enhanced photocatalytic performance of ZnO/Bi_2WO_6 heterojunctions toward photodegradation of fluoroquinolone-based antibiotics in wastewater," *Journal of Physics and Chemistry of Solids*, vol. 153, 109995, 2021.

179. F. Hasanvandian, M. Moradi, S. Aghaebrahimi Samani, B. Kakavandi, S. Rahman Setayesh, and M. Noorisepehr, "Effective promotion of $g–C_3N_4$ photocatalytic performance via surface oxygen vacancy and coupling with bismuth-based semiconductors towards antibiotics degradation," *Chemosphere*, vol. 287, 132273, 2022.

180. R. Zhang, J. Jiang, and K. Zeng, "Synthesis of $Bi_2WO_6/g\text{-}C_3N_4$ heterojunction on activated carbon fiber membrane as a thin-film photocatalyst for treating antibiotic wastewater," *Inorganic Chemistry Communications*, vol. 140, 109418, 2022.

181. E.-C. Cho, Y.-S. Hsiao, J.-H. Huang, M.-Y. Sung, Y.-L. Chen, N.-J. Wu, S.-C. Hsu, H. C. Weng, and K.-C. Lee, "Construction of $BiVO_4/Bi_2WO_6/WO_3$ heterojunctions with improved photocatalytic capability in elimination of dye and antibiotics and inactivation of *E. coli*," *Journal of the Taiwan Institute of Chemical Engineers*, vol. 149, 104991, 2023.

182. Q. Yan, Z. Guo, P. Wang, Y. Cheng, C. Wu, and H. Zuo, "Facile construction of 0D/2D In_2O_3/Bi_2WO_6 Z-scheme heterojunction with enhanced photocatalytic activity for antibiotics removal," *Journal of Alloys and Compounds*, vol. 937, 168362, 2023.

183. B. Ma, Y. Zha, P. Yu, G. Chen, Y. Guo, Y. Lan, J. Li, W. Xia, and B. Zhao, "Hydrothermal nanoarchitectonics of Z-scheme $g\text{-}C_3N_4/Bi_2WO_6$ heterojunction with enhanced adsorption and photocatalytic activity for fluoroquinolone antibiotics removal: Kinetics, mechanism and degradation pathway," *Journal of Alloys and Compounds*, vol. 952, 170061, 2023.

184. Y. Hong, C. Li, G. Zhang, Y. Meng, B. Yin, Y. Zhao, and W. Shi, "Efficient and stable Nb_2O_5 modified g-C_3N_4 photocatalyst for removal of antibiotic pollutant," *Chemical Engineering Journal*, vol. 299, 74-84, 2016.

185. C. Zhou, C. Lai, D. Huang, G. Zeng, C. Zhang, M. Cheng, L. Hu, J. Wan, W. Xiong, M. Wen, X. Wen, and L. Qin, "Highly porous carbon nitride by supramolecular preassembly of monomers for photocatalytic removal of sulfamethazine under visible light driven," *Applied Catalysis B: Environmental*, vol. 220, 202-210, 2018.

186. C. Zhou, Z. Zeng, G. Zeng, D. Huang, R. Xiao, M. Cheng, C. Zhang, W. Xiong, C. Lai, Y. Yang, W. Wang, H. Yi, and B. Li, "Visible-light-driven photocatalytic degradation of sulfamethazine by surface engineering of carbon nitride : Properties, degradation pathway and mechanisms," *Journal of Hazardous Materials*, vol. 380, 120815, 2019.

187. H. Ji, P. Du, D. Zhao, S. Li, F. Sun, E. C. Duin, and W. Liu, "2D/1D graphitic carbon nitride/titanate nanotubes heterostructure for efficient photocatalysis of sulfamethazine under solar light: Catalytic "hot spots" at the rutile–anatase–titanate interfaces," *Applied Catalysis B: Environmental*, vol. 263, 118357, 2020.

188. D. Balarak, N. Mengelizadeh, P. Rajiv, and K. Chandrika, "Photocatalytic degradation of amoxicillin from aqueous solutions by titanium dioxide nanoparticles loaded on graphene oxide," *Environmental Science and Pollution Research*, vol. 28, no.36, pp. 49743-49754, 2021.

189. D. Qiao, Z. Li, J. Duan, and X. He, "Adsorption and photocatalytic degradation mechanism of magnetic graphene oxide/ZnO nanocomposites for tetracycline contaminants," *Chemical Engineering Journal*, vol. 400, 125952, 2020.

190. S. Kumar, P. Karfa, K. C. Majhi, and R. Madhuri, "Photocatalytic, fluorescent $BiPO_4$@Graphene oxide based magnetic molecularly imprinted polymer for detection, removal and degradation of ciprofloxacin," *Materials Science and Engineering: C*, vol. 111, 110777, 2020.

191. Y. Vasseghian, D. Sezgin, D. C. Nguyen, H. Y. Hoang, and M. Sari Yilmaz, "A hybrid nanocomposite based on CuFe layered double hydroxide coated graphene oxide for photocatalytic degradation of trimethoprim," *Chemosphere*, vol. 322, 138243, 2023.

192. A. Raja, P. Rajasekaran, K. Selvakumar, M. Arunpandian, K. Kaviyarasu, S. Asath Bahadur, and M. Swaminathan, "Visible active reduced graphene oxide-$BiVO_4$-ZnO ternary photocatalyst for efficient removal of ciprofloxacin," *Separation and Purification Technology*, vol. 233, 115996, 2020.

193. M. Xu, Y. Wang, E. Ha, H. Zhang, and C. Li, "Reduced graphene oxide/$Bi_4O_5Br_2$ nanocomposite with synergetic effects on improving adsorption and photocatalytic activity for the degradation of antibiotics," *Chemosphere*, vol. 265, 129013, 2021.

194. K. O. Sodeinde, S. O. Olusanya, O. S. Lawal, M. Sriariyanun, and A. A. Adediran, "Enhanced adsorptional-photocatalytic degradation of chloramphenicol by reduced graphene oxide-zinc oxide nanocomposite," *Scientific Reports*, vol. 12, no.1, pp. 17054, 2022.

195. J. Wang, L. Zang, L. Wang, Y. Tian, Z. Yang, Y. Yue, and L. Sun, "Magnetic cobalt ferrite/reduced graphene oxide (CF/rGO) porous balls for efficient photocatalytic degradation of oxytetracycline," *Journal of Environmental Chemical Engineering*, vol. 10, no.5, pp. 108259, 2022.

196. A. Dal Conti-Lampert, R. C. Testolin, C. A. Somensi, G. I. Almerindo, T. M. Wagner, O. M. S. Gerlach, E. Sanches-Simões, R. Ariente-Neto, S. Y. G. González, and C. M. Radetski, "Antibiotic degradation and mineralization: efficiency increase on combining different chemical treatment processes," *Journal of Environmental Science and Health, Part A*, vol. 57, no.11, pp. 987-996, 2022.

197. S. Mahalingam, Y. D. Neelan, S. Bakthavatchalam, L. A. Al-Humaid, N. D. Al- Dahmash, H. Santhanam, T.-Y. Yang, N. Hossain, S. H. Park, and J. Kim, "Effective visible-light-driven photocatalytic degradation of harmful antibiotics using reduced graphene oxide-zinc sulfide-copper sulfide nanocomposites as a catalyst," *ACS Omega*, vol. 8, no.36, pp. 32817-32827, 2023.

198. S. Kar, T. Pal, and S. Ghosh, "Reduced graphene oxide–SnSe nanocomposite photocatalyst with high apparent quantum yield for the photodegradation of norfloxacin," *ACS Applied Nano Materials*, vol. 7, no.6, pp. 6516-6524, 2024.

199. W. Zhu, J. Liu, S. Yu, Y. Zhou, and X. Yan, "Ag loaded WO_3 nanoplates for efficient photocatalytic degradation of sulfanilamide and their bactericidal effect under visible light irradiation," *Journal of Hazardous Materials*, vol. 318, 407-416, 2016.

200. V. T. Quyen, J. Kim, P.-M. Park, P. T. Huong, N. M. Viet, and P. Q. Thang, "Enhanced the visible light photocatalytic decomposition of antibiotic pollutant in wastewater by using Cu doped WO_3," *Journal of Environmental Chemical Engineering*, vol. 9, no.1, pp. 104737, 2021.

201. L. Hu, Z. Wang, Y. Shi, C. Liu, Y. Hou, J. Bi, and L. Wu, "Coordination activation enhanced photocatalytic performance for levofloxacin degradation over defect-rich WO_3 nanosheets," *Journal of Environmental Chemical Engineering*, vol. 10, no.6, pp. 108738, 2022.

202. A. Hosseinzadeh, J. L. Zhou, J. Zyaie, N. AlZainati, I. Ibrar, and A. Altaee, "Machine learning-based modeling and analysis of PFOS removal from contaminated water by nanofiltration process," *Separation and Purification Technology*, vol. 289, 120775, 2022.

203. A. Casas, D. Rodríguez-Llorente, G. Rodríguez-Llorente, J. García, and M. Larriba, "Machine learning screening tools for the prediction of extraction yields of pharmaceutical compounds from wastewaters," *Journal of Water Process Engineering*, vol. 62, 105379, 2024.

204. L. Breiman, "Bagging predictors," *Machine Learning*, vol. 24, no.2, pp. 123-140, 1996.

205. P. Geurts, A. Irrthum, and L. Wehenkel, "Supervised learning with decision tree-based methods in computational and systems biology," *Molecular Biosystems*, vol. 5, no.12, pp. 1593-1605, 2009.

206. D. Opitz and R. Maclin, "Popular ensemble methods: An empirical study," *Journal of artificial intelligence research*, vol. 11, 169-198, 1999.

207. P. Geurts, D. Ernst, and L. Wehenkel, "Extremely randomized trees," *Machine Learning*, vol. 63, no.1, pp. 3-42, 2006.

208. A. Natekin and A. Knoll, "Gradient boosting machines, a tutorial," *Frontiers in Neurorobotics*, vol. 7, 2013.

209. L. Xia, P. Zheng, J. Li, X. Huang, and R. X. Gao, "Histogram-based Gradient boosting tree: A federated learning approach for collaborative fault diagnosis," *IEEE/ASME Transactions on Mechatronics*, 1-12, 2023.

210. L. Breiman, "Random Forests," *Machine Learning*, vol. 45, no.1, pp. 5-32, 2001.

211. T. Chen and C. Guestrin. *XGBoost: A scalable tree boosting system*. in *Proceedings of the 22nd acm sigkdd international conference on knowledge discovery and data mining*. 2016.

212. R. Katwal, R. Kothari, and D. Pathania, Chapter 10 - An overview on degradation kinetics of organic dyes by photocatalysis using nanostructured electrocatalyst, in *Delivering Low-Carbon Biofuels with Bioproduct Recovery*, L. Singh and D. M. Mahapatra, Editors. Elsevier. pp. 195-213,2021.

213. T. T. My Hang, N. H. Thao Vy, N. T. Hanh, T.-D. Pham, and L. T. Hoang Yen, "Facile synthesis of copper tungstate ($CuWO_4$) for novel photocatalytic degradation of tetracycline under visible light," *Sustainable Chemistry and Pharmacy*, vol. 21, 100407, 2021.

214. U. Bharagav, N. R. Reddy, V. N. Rao, P. Ravi, M. Sathish, M. V. Shankar, and M. M. Kumari, "$CuWO_4$ as a novel Z-scheme partner to construct TiO_2

based stable and efficient heterojunction for photocatalytic hydrogen generation," *International Journal of Hydrogen Energy*, vol. 47, no.95, pp. 40391-40406, 2022.

215. A. Raza, H. Shen, A. A. Haidry, L. Sun, R. Liu, and S. Cui, "Studies of Z-scheme WO_3-TiO_2/Cu_2ZnSnS_4 ternary nanocomposite with enhanced CO_2 photoreduction under visible light irradiation," *Journal of CO_2 Utilization*, vol. 37, 260-271, 2020.

216. M. M. Rhaman, S. Ganguli, S. Bera, S. B. Rawal, and A. K. Chakraborty, "Visible-light responsive novel WO_3/TiO_2 and Au loaded WO_3/TiO_2 nanocomposite and wastewater remediation: Mechanistic inside and photocatalysis pathway," *Journal of Water Process Engineering*, vol. 36, 101256, 2020.

217. J. Gupta and A. S. Ahmed, "Interfacial exchange coupling and defects driven magnetic and optical properties of Co_3O_4-NiO nanocomposites," *Physica B: Condensed Matter*, vol. 599, 412383, 2020.

218. A. K. John, S. Palaty, and S. S. Sharma, "Greener approach towards the synthesis of titanium dioxide nanostructures with exposed {001} facets for enhanced visible light photodegradation of organic pollutants," *Journal of Materials Science: Materials in Electronics*, vol. 31, no.23, pp. 20868-20882, 2020.

219. V. Gajraj and C. R. Mariappan, "$CuWO_4$: A promising multifunctional electrode material for energy storage as in redox active solid-state asymmetric supercapacitor and an electrocatalyst for energy conversion in methanol electro-oxidation," *Journal of Electroanalytical Chemistry*, vol. 895, 115504, 2021.

220. X. Xiong, H. Chen, and Y. Xu, "Improved Photocatalytic Activity of TiO_2 on the Addition of $CuWO_4$," *The Journal of Physical Chemistry C*, vol. 119, no.11, pp. 5946-5953, 2015.

221. G. Žerjav, M. S. Arshad, P. Djinović, J. Zavašnik, and A. Pintar, "Electron trapping energy states of TiO_2–WO_3 composites and their influence on photocatalytic degradation of bisphenol A," *Applied Catalysis B: Environmental*, vol. 209, 273-284, 2017.

222. X. Wu, X. Wang, Y. Xie, N. Ren, J. Ma, and P. Ning, "Facile in-situ construction of highly dispersed nano zero-valent iron modified black TiO_2 Z-scheme recyclable heterojunction with highly efficient visible-light-driven photocatalytic activity," *Applied Catalysis B: Environmental*, vol. 310, 121325, 2022.

223. K. Santhi, M. Navaneethan, S. Harish, S. Ponnusamy, and C. Muthamizhchelvan, "Synthesis and characterization of TiO_2 nanorods by

hydrothermal method with different pH conditions and their photocatalytic activity," *Applied Surface Science*, vol. 500, 144058, 2020.

224. F. Han, V. S. R. Kambala, M. Srinivasan, D. Rajarathnam, and R. Naidu, "Tailored titanium dioxide photocatalysts for the degradation of organic dyes in wastewater treatment: A review," *Applied Catalysis A: General*, vol. 359, no.1, pp. 25-40, 2009.

225. M. Rafieezadeh and A. H. Kianfar, "Synthesis and characterization of the magnetic submicrocube $Fe_3O_4/TiO_2/CuO$ as a reusable photocatalyst for the degradation of dyes under sunlight irradiation," *Environmental Technology & Innovation*, vol. 23, 101756, 2021.

226. A. S. Ganie, N. Bashar, S. Bano, S. Hijazi, S. Sultana, S. Sabir, and M. Z. Khan, "Development and application of redox active GO supported CeO_2/In_2O_3 nanocomposite for photocatalytic degradation of toxic dyes and electrochemical detection of sulfamaxole," *Surfaces and Interfaces*, vol. 38, 102774, 2023.

227. U. Bharagav, N. R. Reddy, V. N. Koteswararao, P. Ravi, P. K, M. Sathish, K. K. Cheralathan, M. V. Shankar, and M. M. Kumari, "Heterojunction of CdS Nanocapsules–WO_3 Nanosheets Composite as a Stable and Efficient Photocatalyst for Hydrogen Evolution," *Energy & Fuels*, vol. 34, no.11, pp. 14598-14610, 2020.

228. X. Bao, X. Wang, X. Li, L. Qin, S. Han, and S.-Z. Kang, "$CuWO_4$-x nanoparticles incorporated brookite TiO_2 porous nanospheres: Preparation and dramatic photocatalytic activity for light driven H_2 generation," *Materials Research Bulletin*, vol. 136, 111171, 2021.

229. N. Ramesh Reddy, M. Mamatha Kumari, M. V. Shankar, K. Raghava Reddy, S. Woo Joo, and T. M. Aminabhavi, "Photocatalytic hydrogen production from dye contaminated water and electrochemical supercapacitors using carbon nanohorns and TiO2 nanoflower heterogeneous catalysts," *Journal of Environmental Management*, vol. 277, 111433, 2021.

230. H. Hamad, M. M. Elsenety, W. Sadik, A.-G. El-Demerdash, A. Nashed, A. Mostafa, and S. Elyamny, "The superior photocatalytic performance and DFT insights of S-scheme $CuO@TiO_2$ heterojunction composites for simultaneous degradation of organics," *Scientific Reports*, vol. 12, no.1, pp. 2217, 2022.

231. Y. Han, X.-X. Qi, Y.-C. Liu, Y. Wang, Z. Xiang, and X. Wang, "Preparation of $CuWO_4/Bi_2WO_6$ composite and its sonocatalytic removal of tetracycline by combined persulfate," *Journal of Alloys and Compounds*, vol. 1010, 177505, 2025.

232. S. Yurdakal, C. Garlisi, L. Özcan, M. Bellardita, and G. Palmisano, Chapter 4 - (Photo)catalyst Characterization Techniques: Adsorption Isotherms and BET, SEM, FTIR, UV–Vis, Photoluminescence, and Electrochemical Characterizations, in *Heterogeneous Photocatalysis*, G. Marcì and L. Palmisano, Editors. Elsevier. pp. 87-152,2019.

233. Z. A. Chen, X. Yan, and M. Zhi, "Reduced $CuWO_4$ photocatalysts for photocatalytic non-oxidative coupling of methane reaction," *Colloids and Surfaces A: Physicochemical and Engineering Aspects*, vol. 680, 132712, 2024.

234. S. Guan, R. Li, X. Sun, T. Xian, and H. Yang, "Construction of novel ternary Au/$LaFeO_3$/Cu_2O composite photocatalysts for RhB degradation via photo-Fenton catalysis," *Materials Technology*, vol. 36, no.10, pp. 603-615, 2021.

235. X. Li, J. Wan, Y. Ma, J. R. Zhao, and Y. Wang, "Mesopores octahedron GCNOX/Cu_2O@ C inhibited photo-corrosion as an efficient visible-light catalyst derived from oxidized g-C_3N_4/HKUST-1 composite structure," *Applied Surface Science*, vol. 510, 145459, 2020.

236. H. Ali, E. Khan, and I. Ilahi, "Environmental Chemistry and Ecotoxicology of Hazardous Heavy Metals: Environmental Persistence, Toxicity, and Bioaccumulation," *Journal of Chemistry*, vol. 2019, no.1, pp. 6730305, 2019.

237. M. Ahsan, M. M. Rahman, A. E. Alsafrani, M. A. Aziz, A. Almahri, H. M. Marwani, M. M. Rahman, and M. A. Hasnat, "Immobilization of poly(o-aminophenol) film on Pt surface: A robust sensor for detecting As(III) in an acidic medium," *Surfaces and Interfaces*, vol. 39, 102976, 2023.

238. H. S. Magar, R. Y. A. Hassan, and A. Mulchandani, "Electrochemical impedance spectroscopy (EIS): Principles, construction, and biosensing applications," *Sensors*, vol. 21, no.19, pp. 6578, 2021.

239. A. R. Rajamani and S. C. Peter, "Novel Nanostructured Pt/CeO_2@Cu_2O Carbon-Based Electrode To Magnify the Electrochemical Detection of the Neurotransmitter Dopamine and Analgesic Paracetamol," *ACS Applied Nano Materials*, vol. 1, no.9, pp. 5148-5157, 2018.

240. T. Kokulnathan, J. V. Kumar, S.-M. Chen, R. Karthik, A. Elangovan, and V. Muthuraj, "One-step sonochemical synthesis of 1D β-stannous tungstate nanorods: An efficient and excellent electrocatalyst for the selective electrochemical detection of antipsychotic drug chlorpromazine," *Ultrasonics Sonochemistry*, vol. 44, 231-239, 2018.

241. B. Ranjani, J. Kalaiyarasi, D. M. Soundari, K. Pandian, and S. C. B. Gopinath, "Synthesis of novel nanostructured copper tungstate/GCE electrochemical system in deep eutectic solvent medium for simultaneous

detection of dopamine and paracetamol," *Inorganic Chemistry Communications*, vol. 145, 109879, 2022.

242. Q. Shi, Z. Luo, L. Jiang, X. Li, C. Bai, and Q. Yu, "Fabrication and photocatalytic properties of Co doped ZnO nanomaterials," *Materials Letters*, vol. 350, 134952, 2023.

243. O. Messaoudi, A. Mabrouki, M. Moufida, L. Alfhaid, A. Azhary, and S. Elgharbi, "Correlation between experimental and DFT calculations of photocatalytic and optical properties of $La_{0.8}Nd_{0.1}Sr_{0.1}MnO_3$ perovskite: degradation efficiency of methyl orange dye under visible-irradiated conditions," *Journal of Materials Science: Materials in Electronics*, vol. 32, no.17, pp. 22481-22492, 2021.

244. Z. H. Jaffari, A. Abbas, C.-M. Kim, J. Shin, J. Kwak, C. Son, Y.-G. Lee, S. Kim, K. Chon, and K. H. Cho, "Transformer-based deep learning models for adsorption capacity prediction of heavy metal ions toward biochar-based adsorbents," *Journal of Hazardous Materials*, vol. 462, 132773, 2024.

245. D. Chicco, M. J. Warrens, and G. Jurman, "The coefficient of determination R-squared is more informative than SMAPE, MAE, MAPE, MSE and RMSE in regression analysis evaluation," *Peerj computer science*, vol. 7, e623, 2021.

246. R. Selvaraj, S. Jogi, G. Murugesan, N. R. Srinivasan, L. C. Goveas, T. Varadavenkatesan, A. Samanth, R. Vinayagam, M. Ali Alshehri, and A. Pugazhendhi, "Machine learning and statistical physics modeling of tetracycline adsorption using activated carbon derived from *Cynometra ramiflora* fruit biomass," *Environmental Research*, vol. 252, 118816, 2024.

247. R. Antonelli, G. R. P. Malpass, M. G. C. da Silva, and M. G. A. Vieira, "Adsorption of ciprofloxacin onto thermally modified bentonite clay: Experimental design, characterization, and adsorbent regeneration," *Journal of Environmental Chemical Engineering*, vol. 8, no.6, pp. 104553, 2020.

248. N. Watanabe, S. Horikoshi, H. Hidaka, and N. Serpone, "On the recalcitrant nature of the triazinic ring species, cyanuric acid, to degradation in Fenton solutions and in UV-illuminated TiO_2 (naked) and fluorinated TiO_2 aqueous dispersions," *Journal of Photochemistry and Photobiology A: Chemistry*, vol. 174, no.3, pp. 229-238, 2005.

249. M. Cai, M. Pipattanasomporn, and S. Rahman, "Day-ahead building-level load forecasts using deep learning vs. traditional time-series techniques," *Applied Energy*, vol. 236, 1078-1088, 2019.

250. G. M. BinMakhashen, S. A. Bahadi, H. A. Al-Jamimi, and S. A. Onaizi, "Ensemble meta machine learning for predicting the adsorption of anionic

and cationic dyes from aqueous solutions using Polymer/graphene/clay/ MgFeAl-LTH nanocomposite," *Chemosphere*, vol. 349, 140861, 2024.

251. Y. Hou, J. Qi, J. Hu, Y. Xiang, L. Xin, and X. Wei, "Mesoporous Mn-doped Fe nanoparticle-modified reduced graphene oxide for ethyl violet elimination: Modeling and optimization using artificial intelligence," *Processes*, vol. 8, no.4, pp. 488, 2020.

252. G. K. Khiam, R. R. Karri, N. M. Mubarak, M. Khalid, R. Walvekar, E. C. Abdullah, and M. E. Rahman, "Modelling and optimization for methylene blue adsorption using graphene oxide/chitosan composites via artificial neural network-particle swarm optimization," *Materials Today Chemistry*, vol. 24, 100946, 2022.

253. C. E. Onu, J. T. Nwabanne, P. E. Ohale, and C. O. Asadu, "Comparative analysis of RSM, ANN and ANFIS and the mechanistic modeling in eriochrome black-T dye adsorption using modified clay," *South African Journal of Chemical Engineering*, vol. 36, 24-42, 2021.

254. Z. H. Jaffari, A. Abbas, S.-M. Lam, S. Park, K. Chon, E.-S. Kim, and K. H. Cho, "Machine learning approaches to predict the photocatalytic performance of bismuth ferrite-based materials in the removal of malachite green," *Journal of Hazardous Materials*, vol. 442, 130031, 2023.

255. S. Kohzadi, M. Bundschuh, R. Rezaee, N. Marzban, Z. Vahabzadeh, S. A. Johari, B. Shahmoradi, N. Amini, and A. Maleki, "Integrating machine learning with experimental investigation for optimizing photocatalytic degradation of Rhodamine B using neodymium-doped titanium dioxide: a comprehensive approach with toxicity assessment," *Environmental Science and Pollution Research*, vol. 31, no.43, pp. 55301-55316, 2024.

256. Z. Jiang, J. Hu, M. Tong, A. C. Samia, H. Zhang, and X. Yu, "A Novel Machine Learning Model to Predict the Photo-Degradation Performance of Different Photocatalysts on a Variety of Water Contaminants," *Catalysts*, vol. 11, no.9, pp. 1107, 2021.

257. I. Salahshoori, A. Yazdanbakhsh, and A. Baghban, "Machine learning-powered estimation of malachite green photocatalytic degradation with NML-$BiFeO_3$ composites," *Scientific Reports*, vol. 14, no.1, pp. 8676, 2024.

258. T. Thiyagarajan, V. Deivasigamani, M. Raj, C. Joseph, T. Dheivasigamani, B. Palanivel, M. S. Hamdy, and M. Shkir, "Facile synthesis and characterization of WO_3/$CuWO_4$ nanocomposites for the removal of toxic methylene blue dye," *Korean Journal of Chemical Engineering*, vol. 38, no.5, pp. 952-965, 2021.

259. F. Bairamis and I. Konstantinou WO_3 fibers/g-C_3N_4 Z-scheme heterostructure photocatalysts for simultaneous oxidation/reduction of

phenol/Cr (VI) in aquatic media. Catalysts, 2021. 11, 792, DOI: 10.3390/catal11070792.

260. S. Rani, A. Garg, and N. Singh, "Efficient degradation of doxycycline and ofloxacin in an aqueous environment using Fe and Cu doped TiO_2-SiO_2 photocatalyst under sunlight," *Environmental Engineering Research*, vol. 27, no.4, pp. 2022.

261. V. Etacheri, C. Di Valentin, J. Schneider, D. Bahnemann, and S. C. Pillai, "Visible-light activation of TiO_2 photocatalysts: Advances in theory and experiments," *Journal of Photochemistry and Photobiology C: Photochemistry Reviews*, vol. 25, 1-29, 2015.

262. S. Prabhu, A. Nithya, S. C. Mohan, and K. Jothivenkatachalam, "Synthesis, Surface Acidity and Photocatalytic Activity of WO_3/TiO_2 Nanocomposites – An Overview," *Materials Science Forum*, vol. 781, 63-78, 2014.

263. D. He, Y. Yang, J. Tang, K. Zhou, W. Chen, Y. Chen, and Z. Dong, "Synergistic effect of TiO_2-$CuWO_4$ on the photocatalytic degradation of atrazine," *Environmental Science and Pollution Research*, vol. 26, no.12, pp. 12359-12367, 2019.

264. X. Hu, D. Gao, Y. Li, H. Dong, W. Zhou, L. Yang, and Y. Zhang, "Fabrication of novel $CuWO_4$ nanoparticles (NPs) for photocatalytic degradation of methylene blue in aqueous solution," *SN Applied Sciences*, vol. 1, no.1, pp. 119, 2018.

265. C. B. Anucha, I. Altin, E. Bacaksız, T. Kucukomeroglu, M. H. Belay, and V. N. Stathopoulos Enhanced Photocatalytic Activity of $CuWO_4$ Doped TiO_2 Photocatalyst Towards Carbamazepine Removal under UV Irradiation. Separations, 2021. 8, 25, DOI: 10.3390/separations8030025.

266. J. Han, Y. Li, L. Yang, T. Li, Y. Luo, L. Yang, and S. Luo, "Mesoporous TiO_2 with WO_3 functioning as dopant and light-sensitizer: A highly efficient photocatalyst for degradation of organic compound," *Journal of Hazardous Materials*, vol. 358, 44-52, 2018.